ÇUKUROVA UNIVERSITY
INSTITUTE OF NATURAL AND APPLIED SCIENCES

PhD. THESIS

Güvenç AKGÜL

STRUCTURAL CHARACTERIZATION OF Co DOPED ZnO NANOCRYSTALS BY X-RAY ABSORPTION SPECTROSCOPY

DEPARTMENT OF PHYSICS

ADANA, 2011

ÇUKUROVA UNIVERSITY
INSTITUTE OF NATURAL AND APPLIED SCIENCES

STRUCTURAL CHARACTERIZATION OF Co DOPED ZnO NANOCRYSTALS BY X-RAY ABSORPTION SPECTROSCOPY

Güvenç AKGÜL

PhD THESIS

DEPARTMENT OF PHYSICS

We certify that the thesis titled above was reviewed and approved for the award of degree of the Doctor of Philosophy by the board of jury on 04/03/2011

.....	.....	.....
Assist.Prof.Cebrail GÜMÜŞ	Prof.Dr.MetinÖZDEMİR	Assoc.Prof.Faruk KARADAĞ
Supervisor	Jury	Jury

.....	.....
Prof.Dr.Sadullah SAKALLIOĞLU	Assoc.Prof.Mustafa TOPAKSU
Jury	Jury

This PhD Thesis is written at the Physics Department of Institute of Natural And Applied Sciences of Çukurova University.
Registration Number:

Prof. Dr. İlhami YEĞİNGİL
Director
Institute of Natural and Applied Sciences

This study was financially supported by the Research Fund of Çukurova University.
Project Number FEF2007D12

Not: The usage of the presented specific declerations, tables, figures, and photographs either in this thesis or in any other reference without citation is subject to "The law of Arts and Intellectual Products" number of 5846 of Turkish Republic

ABSTRACT

PhD THESIS

STRUCTURAL CHARACTERIZATION OF Co DOPED ZnO NANOCRYSTALS BY X-RAY ABSORPTION SPECTROSCOPY

Güvenç AKGÜL

ÇUKUROVA UNIVERSITY
INSTITUTE OF NATURAL AND APPLIED SCIENCES
DEPARTMENT OF PHYSICS

Supervisor :Assist.Prof.Cebrail GÜMÜŞ
Year : 2011, Pages:159
Jury :Assist. Prof.Cebrail GÜMÜŞ
Prof.Dr.Metin ÖZDEMİR
Prof.Dr.Sadullah SAKALLIOĞLU
Assoc. Prof.Faruk KARADAĞ
Assoc. Prof.Mustafa TOPAKSU

Complex and multinary oxides provide a wide range of functional materials especially when nanostructured. Nanocrystalline $Zn_{1-x}Co_xO$ (x=0-0.50) particles are produced by chemical vapor synthesis (CVS) using laser flash evaporation as a novel precursor delivery method. The crystal and local structure of the samples is studied using X-ray diffraction and X-ray absorption spectroscopy. A single wurtzite phase is observed in samples with Cobalt contents as high as x = 0.25. X-ray absorption spectra show that the Co^{2+} ions are incorporated into the ZnO wurtzite lattice substituting Zn^{2+} ions for Cobalt contents between x=0.001 and x = 0.20. Only small lattice deformations are observed in these solid solutions. In order to investigate the local structure around Co and Zn and their distribution in the $Zn_{1-x}Co_xO$ nanoparticles Extended X-ray absorption fine structure (EXAFS) and X-ray absorption near-edge structure (XANES) spectra are analyzed in detail. These results are compared with XRD measurements to reveal the correlation between doping concentrations and non-isotropic strain in the nano particles. In addition, theorical calculation is done for Co doped ZnO nanomaterials by using FEFF8 code.

Key Words: Cobalt doped ZnO, XAS, XANES, EXAFS, Diluted Magnetic Semiconductors

ÖZ

DOKTORA TEZİ

Co KATKILI ZnO NANOKRİSTALLERİN YAPISAL KARAKTERİZASYONUNUN X-IŞINI SOĞURMA SPEKTROSKOPİSİ İLE İNCELENMESİ

Güvenç AKGÜL

ÇUKUROVA ÜNİVERSİTESİ
FEN BİLİMLERİ ENSTİTÜSÜ
FİZİK ANABİLİM DALI

Danışman :Yrd.Doç. Dr. Cebrail GÜMÜŞ
Yıl : 2011, Sayfa:159
Jüri :Yrd.Doç. Dr. Cebrail GÜMÜŞ
Prof.Dr.Metin ÖZDEMİR
Prof.Dr.Sadullah SAKALLIOĞLU
Doç. Dr. Faruk KARADAĞ
Doç. Dr. Mustafa TOPAKSU

Özellikle nano yapılandırılmış olan karmaşık ve çoklu oksitler, kullanışlı malzemelerin geniş bir aralığını oluşturmaktadır. Nano kristal $Zn_{1-x}Co_xO$ (x=0–0.50) parçacıklar yeni geliştirilen ön çıkışlı laser buharlaştırma kullanılarak kimyasal buharlaştırma sentezlemesi (CVS) yöntemiyle üretilmiştir. Numunelerin yerleşik ve kristal yapısı X-ışını soğurma spektroskopisi ve x-ışını kırınım yöntemi kullanılarak incelenmiştir. X=0.25 yüksek kobalt miktarına kadar numunelerde tekli faz olan Würtzite fazı gözlenmiştir.X=0.001 ve x=0.20 arasında kobalt miktarı için X-ışını sogurma spektroskopisi Wurtize ZnO yapısı içerisinde Co^{2+} iyonlarının Zn^{2+} iyonları yerlerine geçtigini göstermektedir. Sadece, bu katı çözeltiler içerisinde küçük örgü bozunumu gözlenmiştir. $Zn_{1-x}Co_xO$ parçacıklar içinde Co ve Zn cevresinde yerleşik yapıyı ve dağılımlarını incelemek için uzatılmış X-ışını soğurma ince uç yapısı (EXAFS) ve X-ışını soğurma yakın uç yapısı (XANES) spektrası detayda analiz edilmiştir. Bu sonuçlar, nano parçacıklar içinde izotropik olmayan gerilme ve katkı konsantrasyonları arasında ilişkiyi göstermek için XRD ölçümleriyle karşılaştırılmıştır. Ayrıca, FEFF8 kod kullanılarak Co katkılı ZnO nano materyaller için teorik hesap yapılmıştır.

Anahtar Kelimeler: Kobalt katkılı çinko oksit,XAS,XANES, EXAFS,Seyreltilmiş Manyetik Yarıiletkenler.

ACKNOWLEDGEMENTS

Foremost, I would like to express my sincere gratitude to my advisor Assist. Prof.Cebrail *GÜMÜŞ* and Prof.Dr.Yüksel UFUKTEPE for the continuous support of my Ph.D study and research, for their patience and motivation. I want to thank all the colleagues at Argonnne National Laboratory who contributed and helped me with this work. I want to express my sincere thanks to my supervisor Dr. Klaus Attenkofer his time effort and his active support and Dr. Randall E.Winans for giving me the opportunity to work at Argonne National Laboratory (ANL).

I also would like to thank Dr. Ercan Alp from Advanced Photon Source (APS) for the inspiring discussions and his helpful suggestions and support.

Special thanks to Prof. Dr. Markus Winterer, Dr. Ruzica Djenadic and Dr. Moazzam Ali from University of Duisburg-Essen,Germany for their help.

My sincere thanks also goes to Prof. Dr. Herman Winick from Stanford Synchrotron Radiation Laboratory (SSRL) for his financial support. This study is supported by the DOE Cooperative Research Program for Synchrotron-light for Experimental Science and Applications in the Middle East (SESAME) project and Argonne National Laboratory (ANL) by the Department of Energy (DOE).

I would like to thank Dr. Nadia Leyarovska from APS for help at the EXAFS beamline and Dr. Matt Newville from APS for his help with all the software proplems and his thoughtful suggestions to improve this work.

Besides, Mark Engbretson from APS for taking care of my computer needs and last but not least Cathleen Kmak from APS for her help with all the administrative issues.

Finally, I am eternally grateful to my fiancee, Assist.Prof. Funda AKSOY who always have been there in the bad and the good times, thanks for her help , support and constant love and strength throughout the years.

CONTENTS **PAGE**

ABSTRACT……..…….…..…..……..…....I
ÖZ……...…….……..…….....II
ACKNOWLEDGEMENTS..……..…….…..…..……..…....III
CONTENTS……...…….....IV
TABLE CAPTIONS ……..…….…….……..…...VI
FIGURE CAPTIONS …….…….…..……..……VIII
SYMBOLS AND ABBREVIATIONS……..…….…….…….....XIV
1. INTRODUCTION……..……..……...…...…….....1
1.1. Preface.……...……..…….....1
2. REVIEW OF LITERATURE ……..……..…….…….....7
2.1. Introduction ……...……..…….…….....…….7
2.2. Early History of X-rays…….…….…….9
2.3. Bragg`s Law and Nature of X-rays……..…….……....11
2.4. X-ray in Electromagnetic Spectrum.……...……..……....13
2.4.1. Polarization of Electromagnetic Radiation……....…….....17
2.5. Generally production of X-rays ……..…….……..19
2.6. The Synchrotron Light…….……....22
2.6.1. Bending Magnet Radiation...…….……..…….29
2.6.2. Undulator Magnet Radiation……..…….…….....38
2.6.3. Wiggler Magnet Radiation …….……..…....49
2.7. Monochromator and Slits……..…….….53
2.8. Wurtzite ZnO Structure……...…….55
3. MATERIAL AND METHOD……..…….……...…….…….…....59
3.1. Powder Synthesis……..…….….....59
3.2. Structural Characterization……..……...….…...61
3.2.1. X-Ray Diffraction (XRD)...…….…….……...61
3.2.2. Rietveld refinement……..…….…...…....66
3.2.3. Transmission electron microscopy(TEM)……..... 67
3.3. Method ……..…..68

3.4. Argonne National Laboratory (ANL)…….…….....69
3.5. Beamlines…….....70
3.6. Overview of the APS…….……..70
3.7. How APS works……..….....72
3.7.1. Linear Accelerator……...……..73
3.7.2. Booster Synchrotron……...……...74
3.7.3. The Electron Storage Ring……...……..75
3.7.4. Insertion Devices and Brilliance…….…..….....76
3.7.5. Experiment Hall …….....….....77
3.8. X-ray Absorption Spectroscopy…….….....78
3.8.1. X-rays absorption Coefficient……...…...….....84
3.8.2. The Regions of X-ray Absorption Spectroscopy (XAS)…….....87
3.8.3. EXAFS Region…….……..91
3.9. Data Analysis…….……...107
3.9.1. Introduction…….……...…….....107
3.9.1.1. ATHENA Software…….....……108
3.9.1.2. ARTEMIS Software……..…..…...111
4. EXPERIMENTAL RESULTS……...…….…….....….....115
4.1. Synthesis Products…….....115
4.2. Structural Characterization: Long Range Order…….……...…120
4.3. Structural Characterization: Local Structure…….……122
5. CONCLUSION AND DISCUSSION…….....141
6. FUTURE PROSPECTS……..…….....143
REFERENCES……..……..…….……...147
CURRICULUM VITAE……..…….……..…….157
APPENDIX……..……..…….....….….....158

TABLE CAPTIONS **PAGE**

Table 2.1. Differantial form of Maxwell`s Equations in free space…….……16
Table 2.2. The multiplicative correction factor *f(K)* that enables the low *K* analytic formulation of undulator central cone power……...47
Table 2.3. Typical parameters for Synchrotron Radiation…….52
Table 2.4. Properties of forms of Synchrotron Radiation……..53
Table 2.5. A few properties of wurtzite ZnO…….....56
Table 4.1. Results of EXAFS data analysis using ARTEMIS and RMC xas for Co-doped ZnO and Co oxides……..……136

FIGURE CAPTIONS **PAGE**

Figure 2.1. Schematic illustration of Bragg's law……....….12
Figure 2.2. Electromagnetic wave…….……....…14
Figure 2.3. Electromagnetic spectrum…….…….....15
Figure 2.4. The plane polarization of light…….....17
Figure 2.5. (a)The circularly and (b) elliptically polarization of light……..…...….18
Figure 2.6. Some Bremsstrahlung interaction of electrons with target…….…....20
Figure 2.7. Polarized X-rays orientations and directions……...….....24
Figure 2.8. The interaction of different wave length X-ray with atom……..…24
Figure 2.9. Typical Synchrotron facility……..…..……...….....25
Figure 2.10.Relativistic and non-relativistic electron moving……..….....26
Figure 2.11. Photon brilliance as a function of X-ray energy for conventional and synchrotron radiation sources….…….……..…..27
Figure 2.12. Three Forms of Synchrotron Radiation…….....29
Figure 2.13. Illustration of a bending magnet…….....30
Figure 2.14. A schematic of bending magnet radiation illustrating the "searchlight" effect…….....31
Figure 2.15. Bending magnet critical photon energy and Bessel function dependence……....….36
Figure 2.16. Systematic figure of Undulator magnet…….....39
Figure 2.17. Electron motion in a periodic magnetic field…….....39
Figure 2.18. (a) and (b) Power in the Central Radiation cone for soft x-ray undulators (c) Power in the Central Radiation cone for x-ray undulators……..48
Figure 2.19. The transition from undulator radiation (K≤1) to wiggler radiation…50
Figure 2.20. (a) Drawing of the first optical enclosure of a beamline.X-rays enter the optical enclosure from the left. All EXAFS beamlines have a monochromator and slits.Some EXAFS beamlines have one or more mirrors (b) Schematic of basic monochromator components……..54
Figure 2.21. The structure of wurtzite ZnO……...…55

Figure 2.22. Doping ZnO with transmission metals TM……..57
Figure 3.1. CVS reactor for the preparation of Co doped ZnO with laser flash evaporator, hot wall reactor and thermophoretic powder collector as modules…….....60
Figure 3.2. The change in the color of ZnO powders with addition of Co……...60
Figure 3.3. Examples of Miller indices notation for crystal planes …….....62
Figure 3.4. Diffraction of x-rays from parallel planes……...63
Figure 3.5. XRD Pattern of NaCl powder …….…….....64
Figure 3.6. Peak Width-Full Width at Half Maximum…….65
Figure 3.7. Effect of Lattice Strain on Diffraction Peak Position and Width……..66
Figure 3.8. Transmission electron microscope……...…….....68
Figure 3.9. Experimental setup at beamline 12.BM.B…….....69
Figure 3.10. Aerial photo of the Advanced Photon Source facility……...71
Figure 3.11. Beamlines map of APS…….…….....73
Figure 3.12. Linear accelerator at APS…….....74
Figure 3.13. Booster synchrotron at APS……....75
Figure 3.14. The electron storage ring at APS……..……...76
Figure 3.15. Undulator at APS ……..…..…..77
Figure 3.16. Experimental hall at APS…….…78
Figure 3.17. An electron ejected from the atom……..…….80
Figure 3.18. Scheme of the excitation of an electron by the absorption of a X-ray photon……..…..…..……..81
Figure 3.19. Fluorescent x-ray emission…….....82
Figure 3.20. Auger electron emission…….…...83
Figure 3.21. X- ray absorption measurements…….....85
Figure 3.22. (a) X-ray absorption process by a core electron (b) The absorption cross-section……....86
Figure 3.23. Sample x-ray absorption spectra for (a) Ti metal foil (b) Zn metal foil……...87
Figure 3.24. Ni K-edge x-ray absorption spectrum the molecule-based magnet CsNiCr(CN)6……88

Figure 3.25. Universal curve for the electron mean free path as a function of the kinetic energy of the photoelectron……..….89
Figure 3.26. Typical spectrum and metal K edge of XANES……..90
Figure 3.27. Ti K-edge XANES shows dramatic dependence on the local coordination chemistry…….91
Figure 3.28. Schematic of an EXAFS process……...…….…...92
Figure 3.29. X-ray absorption spectra of RbNO3 water solution and rubidium vapour in the energy range of Rb K-edge……..….93
Figure 3.30. (a)An illustration of the EXAFS (left) and XANES (right) processes.93
Figure 3.31. Illustration of the x-ray absorption process…….……..95
Figure 3.32. Energy to wave number conversion……..96
Figure 3.33. Isolated EXAFS χ(k) for FeO……...97
Figure 3.34. Illisturation of x-ray absorption through the photoelectric process…….…….....97
Figure 3.35. The modulates in the absorption coefficient μ(E), causing the EXAFS……..98
Figure 3.36. Functional forms for f(k) (left) and δ(k)(right) for O, Fe, and Pb showing the dependence of these terms on atomic number Z...…...102
Figure 3.37. Illustration of phase shift…….....102
Figure 3.38. Debye-Wallerfactor……..…..…….103
Figure 3.39. Inelastic losses…….104
Figure 3.40. The photo-electron mean-free-path for XAFS λ(k)……106
Figure 3.41. Plots showing the various steps in the data reduction steps in the analysis of EXAFS data…….…….107
Figure 3.42. The main window of the ATHENA program.…….109
Figure 3.43. The main window of the ARTEMIS program.……113
Figure 4.1. Correlation between actual, x_a, and nominal, x, Co content (a), precursor evaporation rate as a function of Co content (b)…….....115
Figure 4.2. comparison of FTIR spectra of the two precursor materials and the emission line of the CO_2 laser……...……116

Figure 4. 3. XRD patterns of as-synthesized $Zn_{1-x}Co_xO$ nanoparticles (vertical bars are three most pronounced Bragg reflections for wutrtzite ZnO, CoO and Co_3O_4)……..…..117

Figure 4.4. Rietveld refinements of the patterns for samples with Co content of $x = 0$ and $x = 0.25$……....118

Figure 4.5. Crystallite size fit (a) according to monodisperse coagulation and microstrain as a function of actual Co content (b) in $Zn_{1-x}Co_xO$ samples and as a function of the relative number of atoms on the particle surface (c)…….…….……119

Figure 4.6. Lattice parameters *a* and *c* and unit-cell volume of the $Zn_{1-x}Co_xO$ samples……..…….121

Figure 4.7. Structural parameters determined from Rietveld refinement as a function of Co content (a) and as a function of relative number of surface atoms (b)…….122

Figure 4.8. Co *K*-edge XANES spectra of $Zn_{1-x}Co_xO$, CoO, Co_3O_4, Co metal and theoretical calculation for Co-doped ZnO (a) and Zn *K*-edge XANES spectra for $Zn_{1-x}Co_xO$ and theoretical calculation for Co-doped ZnO. (b)…….…..124

Figure 4.9. EXAFS spectra (top) and radial structure functions (bottom) on Zn *K*-edge (a) and Co *K*-edge (b) for $Zn_{1-x}Co_x$…….…..126

Figure 4.10. ARTEMIS fit of the Zn- (top) and Co *K*-edge EXAFS spectra (bottom) of $Zn_{0.85}Co_{0.15}O$ (a) and corresponding radial structure functions (b) ……..……127

Figure 4.11. RMC analysis of EXAFS spectra of $Zn_{0.80}Co_{0.20}O$…….…..128

Figure 4.12. Partial pair distribution functions for $Zn_{0.80}Co_{0.20}O$ derived from RMC analysis of EXAFS data……129

Figure 4.13. ARTEMIS fit of the Co *K*-edge (a) and Zn *K*-edge (b) radial structure functions of $Zn_{0.999}Co_{0.001}O$ and insets show EXAFS spectra …….……..130

Figure 4.14. ARTEMIS fit of the Co *K*-edge (a) and Zn *K*-edge (b) radial structure functions of $Zn_{0.995}Co_{0.005}O$ and insets show EXAFS spectra ……131
Figure 4.15. ARTEMIS fit of the Co *K*-edge (a) and Zn *K*-edge (b) radial structure functions of $Zn_{0.99}Co_{0.01}O$ and insets show EXAFS spectra …….....132
Figure 4.16. ARTEMIS fit of the Co *K*-edge (a) and Zn *K*-edge (b) radial structure functions of $Zn_{0.95}Co_{0.05}O$ and insets show EXAFS spectra ……..……..…....133
Figure 4.17. ARTEMIS fit of the Co *K*-edge (a) and Zn *K*-edge (b) radial structure functions of $Zn_{0.90}Co_{0.10}O$ and insets show EXAFS spectra…….....134
Figure 4.18. ARTEMIS fit of the Co *K*-edge (a) and Zn *K*-edge (b) radial structure functions of $Zn_{0.80}Co_{0.20}O$ and insets show EXAFS spectra ……...……...135
Figure 4.19. Partial pair distribution functions for $Zn_{0.90}Co_{0.10}O$ derived from RMC analysis of EXAFS data……...137
Figure 4.20. Cation-Oxygen pair distribution for Co doped ZnO……....137
Figure 4.21. TEM images for Co doped ZnO (a) Only ZnO (b)1%Co and (c) 10% Co…….……138
Figure 4.22. Wurtzite structure (a) the Co doping crystal structure in ZnO nanostructure (b)…….……...…139
Figure 4.23. Displayed are the nearest and next nearest interatomic distances according to RMC data analysis as a function of cobalt content as determined from moment analysis of the corresponding partial pair distribution functions…….……140
Figure 6.1. Simulation of the electric field distribution of a TiO_2 sample structure with a pyramid-like surface morphology and 1V potential difference from the surrounding environment…….……145
Figure 6.2. Schematic view of the sample electron total yield detector……146

SYMBOLS AND ABBREVIATIONS

Symbols

a, b, c	: Lattice parameters
h, k, l	: Miller indices
B	: Magnetic field
d	: Distance
H	: Hamiltonian
E	: Energy,electric field
f	: Frequency
h	: Planck constant
I	: Intensity
k	: Wavevector
N_{el}	: Number of electrons
R	: Distance
t	: Thickness
T_C	: Curie temperature
V	: Volume (unit cell) ,voltage
Z	: Atomic number
θ	: Angle
υ	: Frequency
χ	: Extended X-ray absorption fine structure oscillation
μ	: Absorption coefficient
χ^2	: Chi Square
ω	: Frequency
T	: Transmission
λ	: Wavelength (lambda)
E	: Electric field
Ø	: Phase

c	: Speed of light
∇	: Gradient operator
μ_o	: Permittivity of free spece
ε	: Unit vector
λ_{SWL}	: Short wavelength limit
E_k	: Kinetic energy
m	: Mass of electron
v	: Electron velocity
E_e	: The storage ring energy
t	: Time
p	: Momentum
F	: Force
F_B	: Photon flux
λ_c	: Critical wavelength
N	: Full cycles
γ^*	: Lorentz factor
K	: Magnetic tuning
ε_{crit}	: Critical photon energy
n	: An integer
x_a	: Actual cobalt content
D	: Crystalline size
Q	: Momentum transfer
ρ	: Sample density
A	: Atomic mass
$f(k)$	: Scattering amplitude
$\delta(k)$	: Phase-shift
σ^2	: Debye Waller Factor

N : Number of neighboring atoms

$\dot{A}$: Quantum field theory

a , $a^{\dagger}$: Operators

u : Relative position of the anion

Abbreviations

bcc : Body centered cubic

hcp : Hexagonal close packed

fcc : Face centered cubic

ccp : Cubic closest packed

CN : Coordination number

CVS : Chemical vapor synthesis

LDOS : Local density of states

Exp : Experimental

FTIR : Fourier transform infrared spectroscopy

IR : Ionic radius

RT : Room temperature

TM : Transition element

UV : Ultraviolet

EXAFS : Extended X-ray Absorption Fine Structure

XAFS : X-ray Absorption Fine Spectroscopy

XANES : X-ray Absorption Near Edge Spectroscopy

XAS : X-ray Absorption Spectroscopy

XPS : X-ray Photoelectron Spectroscopy

XRD : X-ray Diffraction

TEM : Transmission Electron Microscopy

FWHM : Full Width at Half Maximum

CVD : Chemical Vapor Deposition

DMS : Diluted magnetic semiconductors

SMSC : Semimagnetic semiconductors

RMC : Reverse Monte Carlo method

MeV	:	Million electron volts
GeV	:	Giga electron volts
ANL	:	Argonne National Laboratory
APS	:	Advanced Photon Source
VUV	:	Visible ultra violet
ZnO	:	Zinc oxide
AAS	:	Atomic absorption spectroscopy
rf	:	Radio frequency
mm	:	Mili meter
CB	:	Conduction band
VB	:	Valence band
RDF	:	Radial distribution function
CIF	:	Crystallographic information file
FTIR	:	Fourier transform infrared spectroscopy

1. INTRODUCTION

1.1. Preface

With the availability of the synchrotron radiation sources, x-ray absorption spectroscopy techniques (XAS) developed into widely used tools for the structural research of materials by identifying the local structure around atoms of a selected type in the sample. In EXAFS (Extended X-ray Absorption Fine Structure) number and species of neighbour atoms, their distance from the selected atom and the thermal or structural disorder of their positions can be determined from the oscillatory part of the absorption coefficient above a major absorption edge. The analysis can be applied to crystalline, nanostructural or amorphous materials, liquids and molecular gases. EXAFS is often the only practical way to study the arrangement of atoms in materials without long range order. (EXAFS) spectroscopy is a powerful experimental tool to get structural information of the investigated material. Our aim is to develope new highly efficient electron emitters for experimental tools. This highly efficient electron emitter will use as a photocathode for streak camera dedector. For this photocathode development we use doped semiconductor doping nanomaterials for example Co doped ZnO. The structural characterization of Co doped ZnO using EXAFS method is only part of developing semiconductor photocathodes. To get structural information such as neighboring atom, distances of atoms, coordination number of the atoms we have used EXAFS method.

Nanoparticles are commonly defined as particles less than 100 nm in diameter (Ichinose et al. ,1992, El-Shall and Edelstein, 1996). They have many properties which differ from the corresponding bulk material thereby making them attractive for many new electronic, optical or magnetic applications. They can be used for these functional applications in the form of granular films, nanocomposites or nanophase materials. If particles are small enough, they become electronically comparable to atoms and molecules, following quantum mechanical rules instead of the laws of classical physics. The scientific and technological issues of nanosized particles and

nanostructured materials are blossoming over the past years and are providing the seeds for new applications in, for instance, catalysis, technical ceramics, membrane technology, optoelectronics, and solid state ionics. The reason for this is that nanosized particles and nanostructured materials, and the physicaland chemical combinations of substances at the nanometer or sub-nanometer scale, can lead to innovative materials with improved or even new, unexpected properties.

Also due to this small size, nanoparticles have a large fraction of surface atoms, i.e. a high surface-to volume ratio. This increases the surface energy compared with that of bulk material. The high surface-to-volume ratio together with size effects (quantum effects) give nanoparticles distinctively different properties (chemical, electronic, optical, magnetic and mechanical) from those of bulk material. For instance, nanoparticle-based semiconductor sensors exhibit higher sensitivities to air pollutants and have lower detection thresholds and lower operating temperatures (Baraton and Merhari, 2004). In various applications e.g. electronic, magnetic and optical (Kruis et al. ,1998), in bioanalysis and in environmental remediation (Kamat and Meisel ,2003, Zhang ,2003), nanoparticles are used.

Nanoparticles such as metals, semiconductors and metal oxides are of great interest for a wide variety of applications in the field of information, energy, environmental and medical technologies due to their unique or improved properties determined primarily by size, composition and structure along with their self-organized film structures.

In addition, more speculative applications in nanotechnology are envisaged, i.e. artificial neural networks, molecular computer components, novel vaccines, quantum computing, targeted cell destruction, implanted biosensors, and targeted drug delivery. Nanoparticle synthesis can be achieved through a wide variety of routes. Basically there are four generic routes to make nanoparticles: i.e.Wet chemical route, Mechanical route, Form-in-place, Gas-phase synthesis

Wet chemical processes include chemistry, hydrothermal methods, sol-gels, and other precipitation processes. Essentially, solutions of different ions are mixed in well-defined quantities and under controlled conditions of heat, temperature and pressure to promote the formation of insoluble compounds, which precipitate out of

solution. These precipitates are then collected through filtering and/or spray drying to produce a dry powder.

Mechanical processes include grinding, milling, and mechanical alloying techniques. Provided that there is a coarse powder, this coarse powder mechanically is transformed into finer and finer powder. The most common processes are either planetary or rotating ball mills. The advantages of these techniques are that they are very simple, require low cost equipment and, provided that a coarse feedstock powder and be made, the powder can be processed. However, there are difficulties such as agglomeration of particles, broad particle size distribution, contamination from the process equipment, and often difficulty in getting to the very fine particle sizes with viable yield. It is commonly used for metals and inorganics.

Form-in-place processes are vacuum deposition processes such as physical vapor deposition (PVD) and chemical vapor deposition (CVD), and spray coating. These processes are focused to the production of nanostructured layers and coatings with enhanced properties for different applications.

Gas phase synthesis includes flame pyrolysis, electro-explosion, laser ablation, and plasma synthesis techniques. The production of fullerenes and carbon nanotubes is a specific subset of gas-phase synthesis techniques. These processes are quite inefficient for the fabrication of powders. Powders can be manufactured by scraping the deposits from the collector.

In last decade diluted magnetic semiconductors (DMSs) or semimagnetic semiconductors (SMSCs) have attracted increasing attention as potential candidates for spintronic devices initiated by theoretical predictions (Dietl ,2000, Sato ,2001). The key requirement for practical applications is the generation of intrinsic ferromagnetism with Curie temperatures above room temperature. Many studies on ZnO doped with cobalt (Kim ,2007, Bouloudenine ,2005, Chambers ,2006) or another transition metal elements (Jin, 2007, Kolesnik ,2004, Cong ,2006) have been reported. However, a major challenge for the preparation of DMS is precipitation of second phases or clusters which may mask ferromagnetism due to intrinsic carrier mediated spin polarization. The source for these problems is the limited solubility of the dopants in ZnO which are in a thermodynamically metastable state. Therefore,

nonequilibrium techniques are preferable to achieve higher doping concentrations (Liu ,2008).

Since stable divalent Cobalt and Zinc oxides exist and the ionic radii of the cations are very similar and tetrahedral coordination is also common for Co^{2+}, it seems a good candidate for substitutional doping in ZnO which is one requirement for intrinsic carrier mediated spin polarization. Additionally, the nonequilibrium technique chemical vapor synthesis (CVS) is used to generate the $Zn_{1-x}Co_xO$ nanoparticles employing laser flash evaporation as a novel precursor delivery method which allows the generation of complex oxides from precursors of low volatility (Winterer, 2007).

Ferromagnetism at room temperature has been experimentally observed for several doped oxidic semiconductors (Co:ZnO, Ti:ZnO , Mn:ZnO, Co:TiO2, Mn:TiO2, etc.), but its origin is still under discussion. The present work is an effort to understand the structral characterization of Co doped the $Zn_{1-x}Co_xO$ nanoparticles. In order to investigate local structure of the Co in Co-doped ZnO nanoparticles X-ray absorption spectra are measured at the Co *K*-edge and Zn *K*-edge using EXAFS method. Because EXAFS spectroscopy is a powerful experimental tool to get structural information of the investigated material. The EXAFS data are also analyzed using ARTEMIS and FEFF8 programme and compared the Reverse Monte Carlo Method (RMC). The program xafsX (Winterer ,1997) is used for XAFS data reduction. The EXAFS data are analysed by the Reverse Monte Carlo Method (RMC) using the rmcxas program (Winterer, 2000). Both, unfiltered and filtered (by Fourier back transformation from R-space between 0.5 Å and 3.5 Å) data are investigated . The structural results– pair distribution functions and their moment analysis are almost identical, however the RMC analysis of filtered data is converging better since most multiple scattering signals are eliminated which would only be possible to fit using higher order correlation functions. Therefore, we describe only the results for the filtered data. Initial atom configurations are generated from results of the Rietveld refinements of X-ray-diffraction data of the corresponding samples and contain an appropriate number of Co atoms. Zn and Co EXAFS spectra are analysed simultaneously using a single atomic configuration

where an appropriate number of Zn atoms are substitutionally replaced in a wurtzite lattice by Co atoms. Theoretical amplitude and phase functions for RMC analysis are obtained by FEFF8 simulations (Ankudinov ,1998).

ARTEMIS is a program for analyzing EXAFS data and uses chi(k) as it‘s input. FEFF8 is used as external program to calculate basic spectra for XANES fitting. FEFF8 is self-consistent real space multiple-scattering code for simultaneous calculations of x-ray absorption spectra and electronic structure. Output includes extended x-ray-absorption fine structure (EXAFS), full multiple scattering calculations of various x-ray absorption spectra (XAS) and projected local densities of states (LDOS).

2. REVIEW OF LITERATURE

2.1. Introduction

Materials for optoelectronic devices and spintronics are receiving increasing attention in the last few years. A variety of materials, specially diluted magnetic semiconductors, have been investigated in this connection(Chambers *et al.*, 2003 and Ziese *et al.*, 2001) Diluted magnetic semiconductors (DMSs) has attracted increasing attention as potential candidates for spintronic devices initiated by theoretical predictions. Due to these features worldwide experimental and theorical efforts have been directed towards understanding the underlying physics of the unusual phenomena associated with these special semiconductors. The importance of the materials was reported firstly by Kamarov et al in 1977 which was about magnetic–optical effects in CdMnTe (Kamarov *et al.*, 1977). ZnO based DMS is particular interesting since the room temperature ferromagnetism was reported for various dopants (Yoon *et al.* 2003, Venkatesan *et al.*2004, Sluiter *et al.*2005, Sati *et al.*, 2006). Especially, TM doped ZnO-based DMS have attracted much attention as ferromagnetic semiconductors with a high Curie temperature above 300K and large magnetization (Dietl *et al.* , 2000). Other important paper about Co doped ZnO was written by Wu *et al.*,2004. They have obtained a dilute magnetic semiconductor in $Zn_{1-x}Co_xO$ nanorods with a Curie temperature higher than 350 K using a simple thermal chemical vapor deposition method (Wu *et al.*,2004).

Doping nanomaterials provides a flexible way to tune to the properties of the materials while maintaining their high surface areas. The electronic, optical, photochemical, photo electrochemical, photocatalytic and photoexcited relaxation properties can be tuned towards the desired direction by doping different elements. The materials can be engineered towards specific applications through careful selection of the dopants.(Chen X, 2005). A unique subset of semiconductor nanomaterials is doped semiconductor nanoparticles. One of the II-VI semiconductors, ZnO doped with transition metal $Zn_{1-x}TM_xO$: TM=Co, Mn, Fe, and Ni, has attracted renewed attention as a promising ferromagnetic semiconducting

material having a *Tc* above room temperature according to theoretical predictions.(Dietl *et al.*, 2000 and Sato *et al.* , 2001) $Zn_{1-x}TM_xO$ is close to being realized as a room temperature ferromagnetic semiconductor due to recent experimental studies.(Ueda *et al.*, 2001, Lee *et al.*,2002, Radovanovic *et al.*2003,Sharma *et al.*2004, Yin *et al.*2004,Yan *et al.*2004). But there is a big controversy about the origin of ferromagnetism in $Zn_{1-x}TM_xO$.(Jin *et al.*,2001, Venkatesan *et al.*,2004 and Cheng *et al.*,2003) Some authors(Kim *et al.*, 2002, Park *et al.*2004.) believed that the secondary phases of TM clusters and their oxides might be responsible for the observed ferromagnetism in $Zn_{1-x}TM_xO$. Secondary phase formation along with single phase $Zn_{1-x}TM_xO$ depends on the growth conditions, i.e., doping concentration *x* and sample preparation temperature *Tg*. However, the past studies are still inadequate to predict suitable *x* of any TM in ZnO to grow $Zn_{1-x}TM_xO$ in single phase at any *Tg*.

A report of ferromagnetism in Co doped TiO_2 (Matsumoto *et al.*,2007) gave the hope that Co- and Mn-doped oxides may indeed be useful for spintronics. Theoretical calculations of Sato *et al.*,2000 showed that ZnO doped with several 3d transition metal ions such as V, Cr, Fe, Co and Ni may exhibit ferromagnetic ordering. A number of workers have, therefore, investigated ZnO doped with transition metal ions in the last few years, in particular, thin films of Co doped ZnO. Results of these studies have been reviewed by Chambers *et al.*,2006 and Farrow *et al.*,2003 and Prellier et al. 2003.The latter authors conclude that the Co-doped ZnO films generally exhibit ferromagnetism above room temperature. The earlier work on Co-doped ZnO films showed them to be ferromagnetic with a $T_C > 280$ K,(Ueda *et al*, 2001) recent results are not altogether conclusive. $Zn_{1-x}Co_xO$ films obtained by the sol-gel method were found to be ferromagnetic with a T_C>300 K by Lee et al. 2002 although the presence of a secondary phase was noted in the samples $x \geq 0.25$. Films of Co-doped ZnO prepared by pulsed laser deposition are reported to be ferromagnetic at room temperature(Rode *et al.*, 2003, Ramachandran *et al.*,2004) but Norton *et al.* 2003,suggest that Co nanocrystallites present in the sample could be responsible for the ferromagnetism. Room-temperature ferromagnetism and negative magneto resistance were reported recently by Yan *et al.*,2003 on thin films

synthesized on the sub nanometer scale by sputtering. Polycrystalline monophasic samples do not appear to exhibit ferromagnetism. Risbud *et al*. 2003 show that well characterized stoichiometric bulk samples of $Zn_{1-x}Co_xO$ are not ferromagnetic and indicate dominant nearest-neighbour antiferromagnetic interaction. These samples were prepared by heating a solid solution of zinc and cobalt oxalates at a temperature of 1173 K for 15 min. Deka *et al.*,2004 have reported ferromagnetism upto 750 K in polycrystalline $Zn_{1-x}Co_xO$ prepared by combustion synthesis. The reaction temperature in such a combustion synthesis will be rather high. Colloidal Co^{2+} doped ZnO nanocrystals prepared by the isocrystalline core-shell method are reported to be ferromagnetic.(Schwartz *et al.*,2003) Other paper about Co doped ZnO was written by Zhi Sun *et al.*,2008 *and* Tonghei *et al.*,2007 .In these work x-ray absorption fine structure (XAFS) at Co *K* edge and X-ray diffraction is used to investigate the Co occupation sites and distributions in $Zn_{1-x}Co_xO$ thin films with Co concentrations. Co *K*-edge XAFS analysis indicates unambiguously that the doped Co ions are substantially incorporated into the ZnO host lattice.

2.2. Early History of X-rays

Discovered in 1895 by Wilhelm Rontgen, a professor of physics at Wurtzburg University while studying the discharge of electricity through rarefied gases. In a darkened room he made the accidental discovery that a paper washed in Barium – Platino-Cyanide hights up and fluorescence equally well whether the coated side or the other side is turned towards the discharge tube. Realizing immediately the importance of his discovery . He begins to study these new rays which he calls x-rays. In this first paper on these new rays Rontgen describes most of the basic properties of x-rays. Within three months after his discovery x-rays were being put to use in a hospital in Vienna. In 1901 Rontgen was awarded the first Nobel Prize in Physics for his discovery “The news spread like wildfire. Public and scientific press alike hailed the discovery as epoch making and correctly.For here was the matc that lit the torch that is modern science”. Lecture by Arthur Compton.

By the time synchrotron radiation was observed almost a half-century later the scientific use of x-rays was established. Many discoveries in physics, chemistry and medicine have been made using X-rays. The most important ones awarded with the Nobel Prize are the following ;

1901: W.C.Rontgen,in physics, for the discovery of x-rays

1914: M.Von Laue,in physics,for the discovery of x-ray diffraction by crystals

1915: W.H.Bragg and W.L.Bragg, in physics for determination of crystal structures using x-rays

1917: C.G.Barkla ,in physics for the discovery of the characteristic x-ray radiation of the elements

1924: M.Siegbahn,in physics for discoveries emission satellites in the field of x-ray spectroscopy

1927: A.H.Compton,in physics for revealing the particle nature of x –rays in scattering experiments on electrons

1936: P.Debye ,in chemistry ,for determining molecular structures by x-ray diffraction in gases

1962: M.F.Perutz and J.C.Kendrew ,in chemistry ,for determining the structure of hemoglobin snd myoglobin

1962: F.Crick ,J.Watson snd M.Wilkins ,in medicine ,for their discoveries concerning the molecular structure of nucleic acids and its significance for information transfer in living material.

1964: D.Crowfoot Hodgking,in chemistry ,for the determination of the structure of penicillin and other important biochemical substances

1976: W.N. Lipscomb ,in chemistry ,for the determination of boranes

1979: A.M. Cormack and G.N. Hounsfield ,in medicine ,for the development of computerized tomography

1981: M.Siegbahn ,in physics ,for developing high resolution electron spectroscopy

1985: H.A.Hauptman and J.Karle ,in chemistry ,for the development of direct methods for x-ray crystallographic structure determination

1988: J.Deisenhofer ,R.Huber and H.Michel,in chemistry ,for the determination of protein structures crucial to photosynthesis.

2.3. Bragg`s Law and Nature of X-rays

The very short wavelengths of x-rays, hinted at in early diffraction studies in which the rays were passed through narrow slits, was firmly established in 1912 by the pioneering work of the German physicist Max von Laue and his students Walter Friedrich and Paul Knipping. Laue suggested that the ordered arrangements of atoms in crystals could serve as natural three-dimensional diffraction gratings. Typical atomic spacings in crystals are approximately 1 angstrom (1×10^{-10} meter), ideal for producing diffraction effects in electromagnetic radiation of comparable wavelength. Friedrich and Knipping verified Laue's predictions by photographing diffraction patterns produced by the passage of X-rays through a crystal of zinc sulfide. These experiments demonstrated that X-rays have wavelengths of about 1 angstrom and confirmed that the atoms in crystals are arranged in regular structures.

In the following year, the British physicist William Lawrence Bragg devised a particularly simple model of the scattering of x-rays from the parallel layers of atoms in a crystal. The Bragg law shows how the angles at which x-rays are most efficiently diffracted from a crystal are related to the x-ray wavelength and the distance between the layers of atoms. Bragg's physicist father, William Henry Bragg, based his design of the first x-ray spectrometer on his son's analysis. The pair used their x-ray spectrometer in making seminal studies of both the distribution of wavelengths in x-ray beams and the crystal structures of many common solids an achievement The Braggs and his father were awarded the Nobel Prize in physics in 1915 for their work in determining crystal structures beginning with NaCl, ZnS and diamond. (Encyclopedia Brittannica)

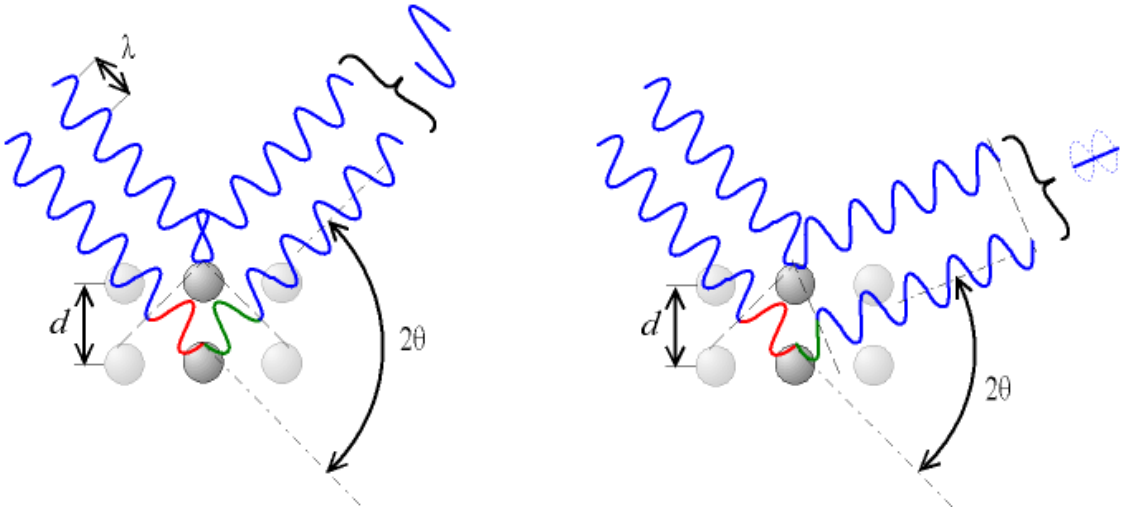

Figure 2.1. Schematic illustration of Bragg's law(http://en.wikipedia.org/wiki/Braggs %27s_law)

$$n\,l = 2d.sin\theta \qquad (2.1.)$$

Equation (2.1) is called Bragg`s law where variable *d* is the distance between atomic layers in a crystal, and the variable (λ) lambda is the wavelength of the incident x-ray beam, n is an integer.

This observation is an example of x-ray wave interference, commonly known as x-ray diffraction (XRD), and was direct evidence for the periodic atomic structure of crystals postulated for several centuries. Although Bragg's law was used to explain the interference pattern of x-rays scattered by crystals, diffraction has been developed to study the structure of all states of matter with any beam, e.g., ions, electrons, neutrons, and protons, with a wavelength similar to the distance between the atomic or molecular structures of interest.

In the early 1920s, experimental studies of the scattering of x-rays from solids played a key role in establishing the particle nature of electromagnetic radiation. In 1905 German physicist Albert Einstein had proposed that electromagnetic radiation is granular, consisting of quanta (later called photons) each with an energy $h\upsilon$, where *h* is Planck's constant (about 6.62×10^{-34} joule.second) and υ is the frequency of the radiation. Einstein's hypothesis was strongly supported in subsequent studies of the

photoelectric effect and by the successes of Danish physicist Niels Bohr's model of the hydrogen atom and its characteristic emission and absorption spectra. Further verification came in 1922 when American physicist Arthur Compton successfully treated the scattering of x-rays from the atoms in a solid as a set of collisions between x-ray photons and the loosely bound outer electrons of the atoms.

Adapting the relation between momentum and energy for a classical electromagnetic wave to an individual photon, Compton used conservation of energy and conservation of momentum arguments to derive an expression for the wavelength shift of scattered x-rays as a function of their scattering angle. In the so-called Compton effect, a colliding photon transfers some of its energy and momentum to an electron, which recoils. The scattered photon must thus have less energy and momentum than the incoming photon, resulting in scattered x-rays of slightly lower frequency and longer wavelength. Compton's careful measurements of this small effect, coupled with his successful theoretical treatment (independently derived by the Dutch scientist Peter Debye), provided convincing evidence for the existence of photons. The approximate wavelength range of the x-ray portion of the electromagnetic spectrum, 10^{-8} to 10^{-12} metre, corresponds to a range of photon energies from about 100 eV (electron volts) to 1 MeV .

2.4. X-Ray in Electromagnetic Spectrum

X-rays are a form of electromagnetic radiation. Electromagnetic (EM) radiation is a self-propagating wave in space or through matter. EM radiation has an electric and magnetic field component which oscillate in phase perpendicular to each other and to the direction of energy propagation. An illustrated electromagnetic wave is given in figure 2.2. Electromagnetic radiation is classified into types according to the frequency of the wave, these types include (in order of increasing frequency): radio waves, microwaves, terahertz radiation, infrared radiation, visible light, ultraviolet radiation, x-rays and gamma rays. Of these, radio waves have the longest wavelengths and Gamma rays have the shortest. A small window of frequencies, called visible spectrum or light, is sensed by the eye of various

organisms, with variations of the limits of this narrow spectrum. EM radiation carries energy and momentum, which may be imparted when it interacts with matter.

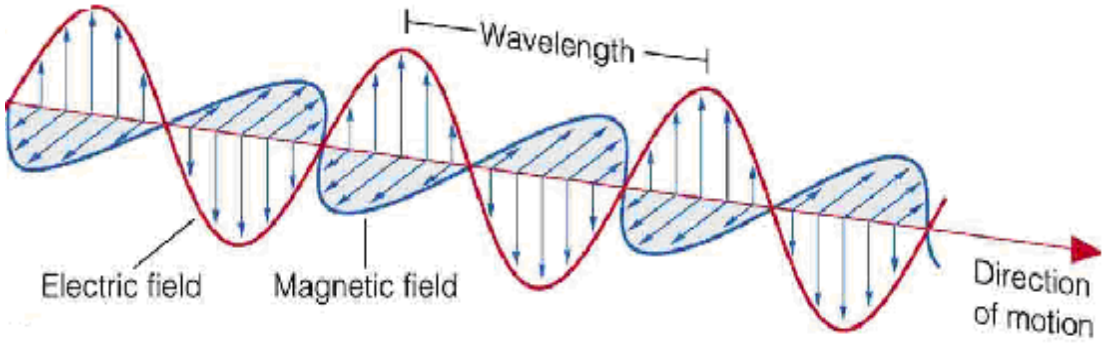

Figure 2.2. An x-ray is a tranverse electromagnetic wave,where tha electric and magnetic field ***E*** and ***B***, are perpendicular to each other and to the direction of propagation **k (**spot.pcc.edu/.../electromag-wavelength.jpg**)**

Their basic physical properties are identical to those of the more familiar components of the electromagnetic spectrum visible light, infrared radiation, and ultraviolet radiation. As with other forms of electromagnetic radiation, x-rays can be described as coupled waves of electric and magnetic fields traveling at the speed of light (about 300,000 km, or 186,000 miles, per second).Electromagnetic spectrum is given in figure 2.3. Their characteristic wavelengths and frequencies can be demonstrated and measured through the interference effects that result from the overlap of two or more waves in space.

X- rays are electromagnetic radiation ranging in wavelength from about 100 Å to 0.01 Å. The shorter the wavelength of the x ray, the greater is its energy and its penetrating power. Longer wavelengths, near the ultraviolet-ray band of the electromagnetic spectrum, are known as soft x -rays. The shorter wavelengths, closer to and overlapping the gamma-ray range, are called hard x- rays.

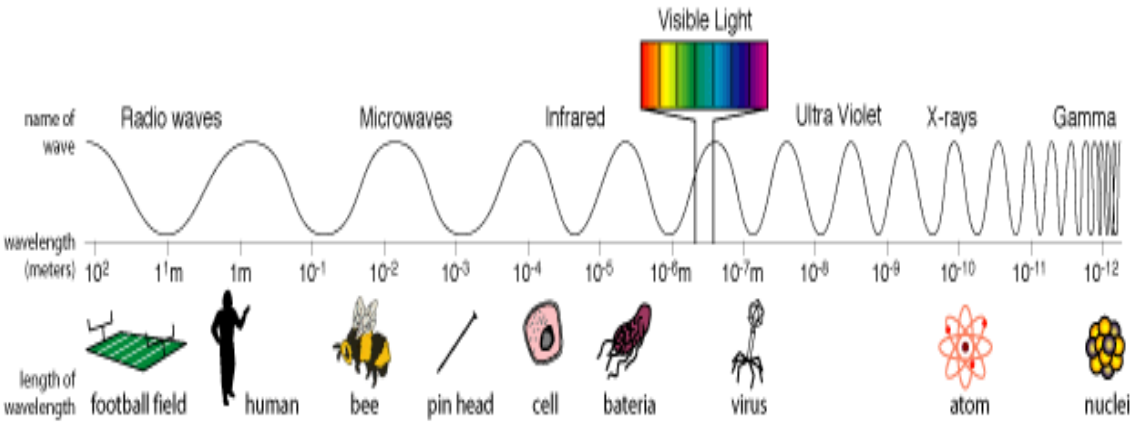

Figure 2.3. Electromagnetic spectrum

Electromagnetic radiation can be considered as wave motion in accordance with classical theory.

$$E = A.exp(i\omega t-Ø) \qquad (2.2.)$$

where A ;amplitude of the wave, ω;frequency (ω= 2πν) and Ø ;phase (Ø = νt)

According to the quantum theory electromagnetic radiation can also be considered as a particles called photons. Each photon has associated with it an amount of energy.

$$E=h\upsilon \qquad (2.3.)$$

where h is called planck`s constant and it has $6.63x10^{-34}$ j.s. Relationship between wavelength and frequency is

$$\lambda=c/\upsilon \qquad (2.4.)$$

where c is velocity of light and it has $3x10^{8}$ meter/sec.

Though it was immediately suspected, following Röntgen's discovery, that x-rays were a form of electromagnetic radiation, this proved very difficult to establish.

x-rays are distinguished by their very short wavelengths, typically 1,000 times shorter than the wavelengths of visible light. Because of this, and because of the practical difficulties of producing and detecting the new form of radiation, the nature of x-rays was only gradually unraveled in the early decades of the 20th century.

Electromagnetic waves were first postulated by James Clerk Maxwell and subsequently confirmed by Heinrich Hertz. Maxwell derived a wave form of the electric and magnetic equations, revealing the wave-like nature of electric and magnetic fields, and their symmetry. Because the speed of EM waves predicted by the wave equation coincided with the measured speed of light, Maxwell concluded that light itself is an EM wave.

According to Maxwell's equations, a time-varying electric field generates a magnetic field and vice versa. Therefore, as an oscillating electric field generates an oscillating magnetic field, the magnetic field in turn generates an oscillating electric field, and so on. These oscillating fields together form an electromagnetic wave.

Table 2.1. Differantial form of Maxwell`s Equations in free space

Gauss' law	$\tilde{N}.\mathbf{E} = \frac{r}{e_0}$
Gauss' law for magnetism	$\tilde{N}.\mathbf{B} = 0$
Maxwell-Faraday equation	$\tilde{N}\mathbf{x}\vec{E} = -\frac{\partial \vec{B}}{\partial t}$
Ampere and Maxwell 's law	$\tilde{N}\mathbf{x}\vec{B} = \mu_o \vec{J} + \mu_o \varepsilon_o \frac{\partial \vec{E}}{\partial t}$
Velocity of light	$\mathbf{c} = \frac{1}{\sqrt{m_o e_o}} \approx 3x10^8 \frac{m}{s}$

In classical electromagnetism, Maxwell's equations are a set of four partial differential equations that describe the properties of the electric and magnetic fields and relate them to their sources, charge density and current density. These equations

are used to show that light is an electromagnetic wave. These equations are shown in table 2.1.

X-rays also exhibit particle-like properties; they can be described as a flow of photons carrying discrete amounts of energy and momentum. This dual nature is a property of all forms of radiation and matter and is comprehensively described by the theory of quantum mechanics.

2.4.1. Polarization of Electromagnetic Radiation

In 1906 the British physicist Charles Glover Barkla first demonstrated the wave nature of X-rays by showing that they can be “polarized” by scattering from a solid. Polarization refers to the orientation of the oscillations in a transverse wave; all electromagnetic waves are transverse oscillations of electric and magnetic fields. Polarization is a property of waves that describes the orientation of their oscillations.

Polarization is used in areas of science and technology dealing with wave propagation, such as optics, seismology, and telecommunications. For electromagnetic waves such as light, the polarization is described by specifying the direction of the wave's electric field.

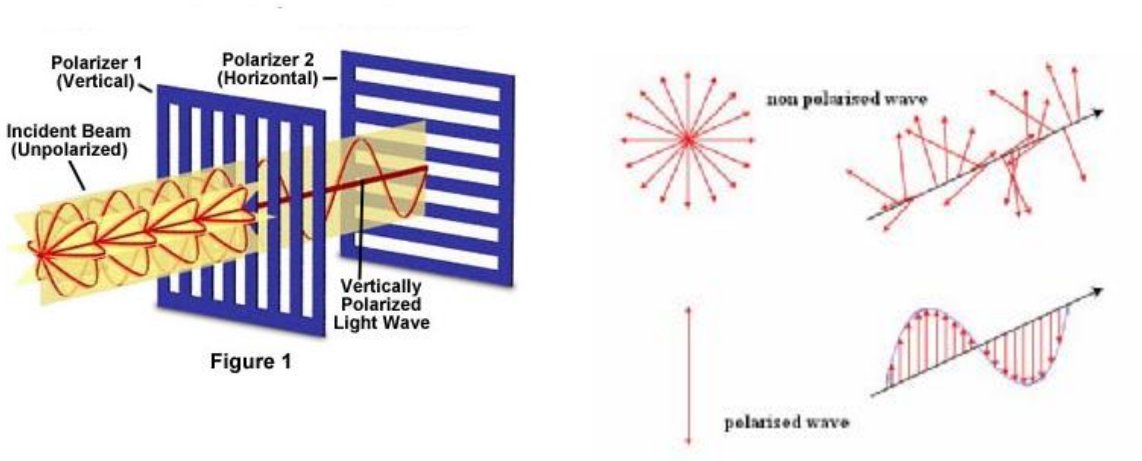

Figure 2.4. The plane polarization of light (http://webphysics.davidson.edu/faculty)

Light consists of oscillating electrical fields, denoted by E, and magnetic fields, denoted by B. We will concentrate on the electric field component and ignore

the magnetic field; however, we could just as well describe light and its effects in terms of the magnetic field component. We don't do it because the interaction of magnetic fields with charged particles is more complex than electric fields, but we could.

Light whose electric field oscillates in a particular way is said to be polarized. If the oscillation is in a plane, the light is said to be *plane polarized* . Plane polarized light is shown in fig.2.4. Plane polarized light can be polarized in different directions. Light can also be *circularly polarized*, with its electric field direction spiraling in a screw pattern. Circularly polarized light can be right- or left-handed. Light can consist of a combination of plane and circular polarization as well; its electric field spirals in a screw fashion with an elliptical cross-section. Such light is called *elliptically polarized*. circularly polarized and elliptically polarized are shown in fig. 2.5.

Although we often speak of "unpolarized" light, every photon of light is polarized in some manner. "Unpolarized" light is a random mixture of light of all polarizations. When light has an easily observed dominant polarization, we refer to it as polarized.

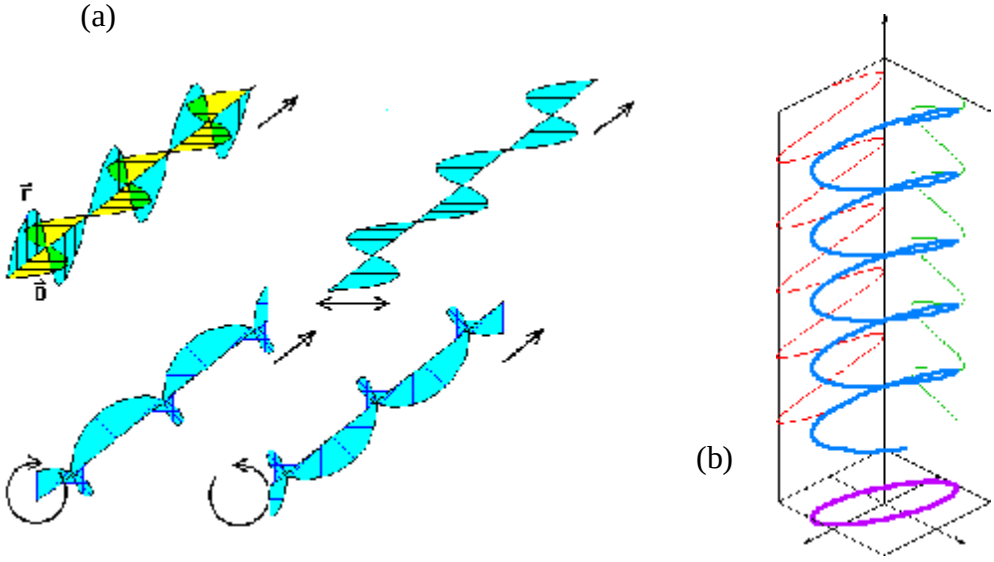

Figure2.5. (a)The circularly and (b) elliptically polarization of light (http://wikipedi.org)

According to the Maxwell equations, the direction of the magnetic field is uniquely determined for a specific electric field distribution and polarization. Already we know that synchrotron radiation is a polarized radiation.

The spatial and temporal variation of a plane wave propagation along the z-axis can be encompassed in one simple expression, $E_o e^{i(kz-\omega t)}$. More generally the three dimensions the polarization of the electric field is written as a unit vector **ε**, and the wavevector along the direction of propagation as **k,** so that

$$\boldsymbol{E(r.t)} = \varepsilon E_o e^{i(\boldsymbol{kr}-\omega t)} \qquad (2.5.)$$

Since electromagnetic waves are transverse we have $\boldsymbol{\varepsilon.k} = 0$, $\boldsymbol{k.E} = \boldsymbol{k.B} = 0$ as shown in Fig.2.2. This is the classical description of a linearly polarized, electromagnetic plane wave. (Nielsen, *et al.* 2001)

2.5. Generally Production of X-rays

There are three common mechanisms for the production of x-rays: the acceleration of a charged particle (electrons or positrons) in a store ring, atomic transitions between discrete energy levels, and the radioactive decay of some atomic nuclei. Each mechanism leads to a characteristic spectrum of x-ray radiation.

In the theory of classical electromagnetism, accelerating electric charges emit electromagnetic waves. In the most common terrestrial source of x-rays, the x-ray tube, a beam of high-energy electrons impinges on a solid target. As the fast-moving electrons in the beam interact with the electrons and nuclei of the target atoms, they are repeatedly deflected and slowed. During this abrupt deceleration, the beam electrons emit bremsstrahlung (German: “braking radiation”) a continuous spectrum of electromagnetic radiation with a peak intensity in the x-ray region. This braking radiation is illustrated in fig.2.6. Most of the energy radiated in an x-ray tube is contained in this continuous spectrum. Far more powerful (and far larger) sources of a continuum of x-rays are synchrotron particle accelerators and storage rings. In a synchrotron, charged particles (usually electrons or positrons) are accelerated to very

high energies (typically billions of electron volts and they have very high speed which is close light speed v ≈0.999c) and then confined to a closed orbit by strong magnets. When the charged particles are deflected by the magnetic fields (and hence accelerated via the change in their direction of motion), they emit so-called synchrotron radiation a continuum whose intensity and frequency distribution are determined by the strength of the magnetic fields and the energy of the circulating particles. Specially designed synchrotron light sources are used worldwide for x-ray studies of materials.

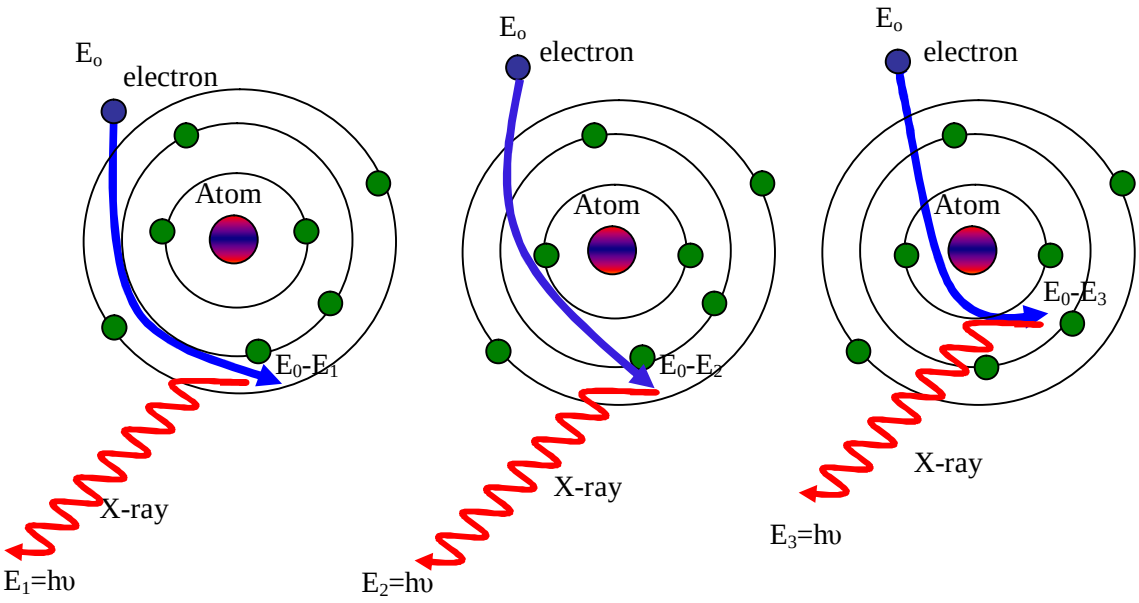

Figure 2.6. Some Bremsstrahlung interaction of electrons with target

X-ray emission is sometimes a by-product of a nuclear transformation. In the process of electron capture, an inner-shell atomic electron is captured by the atomic nucleus, initiating the transformation of a nuclear proton into a neutron and lowering the atomic number by one unit. The vacant inner-shell orbit is then quickly filled by an outer-shell electron, producing a characteristic x-ray photon. The relaxation of an excited nucleus to a lower-energy state also sometimes results in the emission of an x-ray photon. However, the photons emitted in most nuclear transitions of this type are of even higher energy than x-rays they fall into the gamma-ray region of the electromagnetic spectrum. (Encyclopedia Brittannica).

In an x-ray tube, in addition to the continuous spectrum of radiation emitted by the decelerating electrons, there is also a spectrum of discrete x-ray emission lines that is characteristic of the target material. This “characteristic radiation” results from the excitation of the target atoms by collisions with the fast-moving electrons. Most commonly, a collision first causes a tightly bound inner-shell electron to be ejected from the atom; a loosely bound outer-shell electron then falls into the inner shell to fill the vacancy. In the process, a single photon is emitted by the atom with an energy equal to the difference between the inner-shell and outer-shell vacancy states. This energy difference usually corresponds to photon wavelengths in the x-ray region of the spectrum. Characteristic x-ray radiation can also be produced from a target material when it is exposed to a primary x-ray beam. In this case, the primary x-ray photons initiate the sequence of electron transitions that result in the emission of secondary x-ray photons.

In 1913 the English physicist Henry Moseley discovered a simple relationship between the wavelengths of the x-ray emission lines from a target and the atomic number of the target element the wavelengths are inversely proportional to the square of the atomic number. Known as Moseley’s law, this relationship proved to be a definitive tool in the determination of atomic numbers in the early days of atomic physics. X-ray fluoresence techniques, in which the wavelengths of characteristic x-rays are recorded following the excitation of a target, are now commonly used to identify the elemental constituents of materials.

X-rays are produced when accelerated electrons collide with the target. The loss of energy of the electrons due to impact is manifested as x-rays. X-ray radiation is produced in an x-ray tube. Most of the kinetic energy of the electrons striking the target is converted into heat, less than 1% being transformed into x-rays. The electrons transfer all their energy into photon energy. The intensity is zero up to a certain wavelength short wavelength limit (λ_{SWL}). The electrons transfer all their energy into photon energy:

$$E_k = \frac{1}{2}mv^2 = eV = h\upsilon_{max} \qquad (2.6.)$$

$$\lambda_{SWL}(Å) = \frac{c}{u} = \frac{hc}{eV} \quad (2.7.)$$

$$\lambda_{SWL}(Å) = \frac{12.4x10^{3}}{V} \quad (2.8.)$$

where is electron charge (1.6×10^{-19}C), E_k; kinetic energy, V; applied voltage, m; mass of the electron (9.11×10^{-31}kg) and v; electron velocity (m/sec). Equation (2.8) shows the numerical relation between wavelength λ in Å and voltage in Volt.

2.6. The Synchrotron Light

Synchrotron light is the electromagnetic radiation emitted when electrons, moving at velocities close to the speed of light, are forced to change direction under the action of a magnetic field. Charged particles do not radiate while in uniform motion, but during acceleration a rearrangement of its electric fields is required and this field perturbation, travelling away from the charge at the velocity of light, is what we observe as electromagnetic radiation. The electromagnetic radiation is emitted in a narrow cone in the forward direction, at a tangent to the electron's orbit. In synchrotron radiation sources (storage rings) highly relativistic electrons are stored to travel along a circular path for many hours. Radiation is caused by transverse acceleration due to magnetic forces in bending magnets (forming the circular path) or periodic acceleration in special insertion device magnets like undulators, wiggler magnets and wave length shifters. Radiation is linearly polarized in the plane of acceleration (in most cases the horizontal plane). Elliptical polarization occurs for bending magnet radiation observed from above or below the midplane. Polarized x-rays orientations and directions is illustrated in fig.2.7.The radiation is emitted in pulses of 10-20 picosec separated by some 2 nanosec or longer separation if desired. Synchrotron light is unique in its intensity and brilliance and it can be generated across the range of the electromagnetic spectrum: from infrared to x-rays.

This phenomenon has been observed for many decades, and was initially an undesired feature in large high-energy particle accelerators. However, the unique properties of the light produced by synchrotrons were noticed, and specialized accelerators built to optimize those desired properties.

The radiation was named after its discovery in a General Electric synchrotron accelerator built in 1946 and announced in May 1947 by Frank Elder, Anatole Gurewitsch, Robert Langmuir, and Herb Pollock in a letter entitled “Radiation from Electrons in a synchrotron”.

Synchrotron light has a number of unique properties. These include:

- High brightness: synchrotron light is extremely intense (hundreds of thousands of times more intense than that from conventional x-ray tubes) and highly collimated.
- Wide energy spectrum: synchrotron light is emitted with energies ranging from infrared light to hard x-rays.

  Tunable: it is possible to obtain an intense beam of any selected wavelength.
- Highly polarized: the synchrotron emits highly polarized radiation, which can be linear, circular or elliptical.
- Emitted in very short pulses: pulses emitted are typically less than a nano-second (a billionth of a second), enabling time-resolved studies.

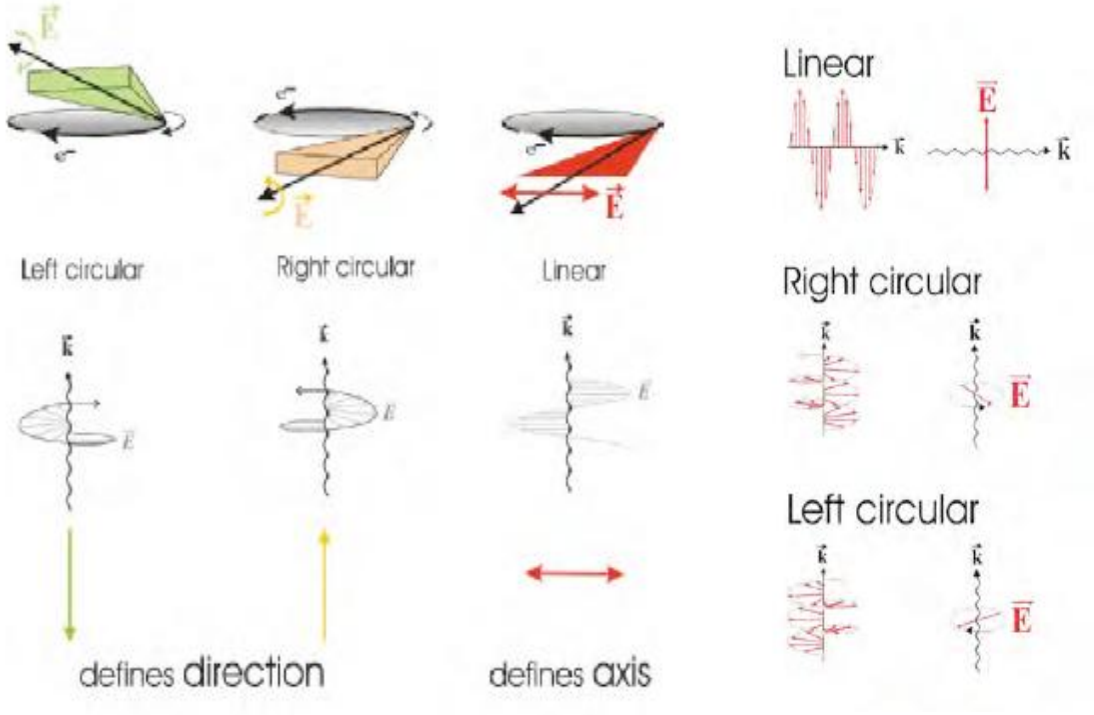

Figure 2.7. Polarized X-rays orientations and directions (Nilsson, 2001)

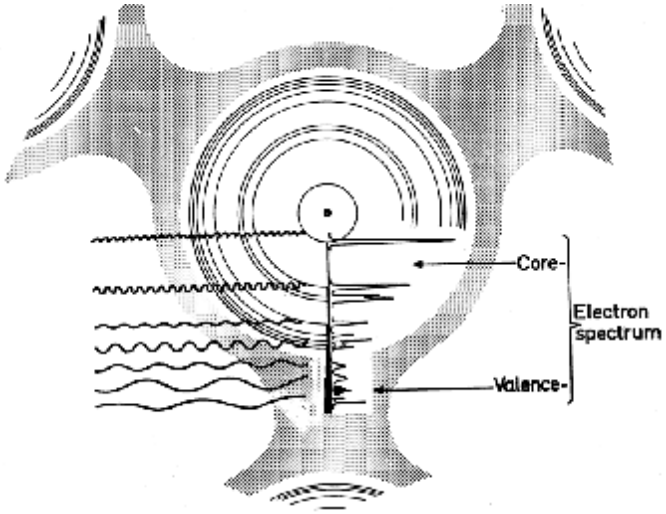

Figure 2.8. The interaction of different wave length X-ray with atom(Nilsson, 2001)

The interaction of different wave length x-ray with atom is illustrated in figure 2.8. Electrons are generated in the centre (electron gun) and accelerated to 99.9997% of the speed of light by the linear accelerator (linac). The electrons are

then transferred to the booster ring, where they are increased in energy. They are then transferred to the outer storage ring .The electrons are circulated around the storage ring by a series of magnets separated by straight sections. As the electrons are deflected through the magnetic field created by the magnets, they give off electromagnetic radiation, so that at each bending magnet a beam of synchrotron light is produced. These operations are illustrated in fig.2.9

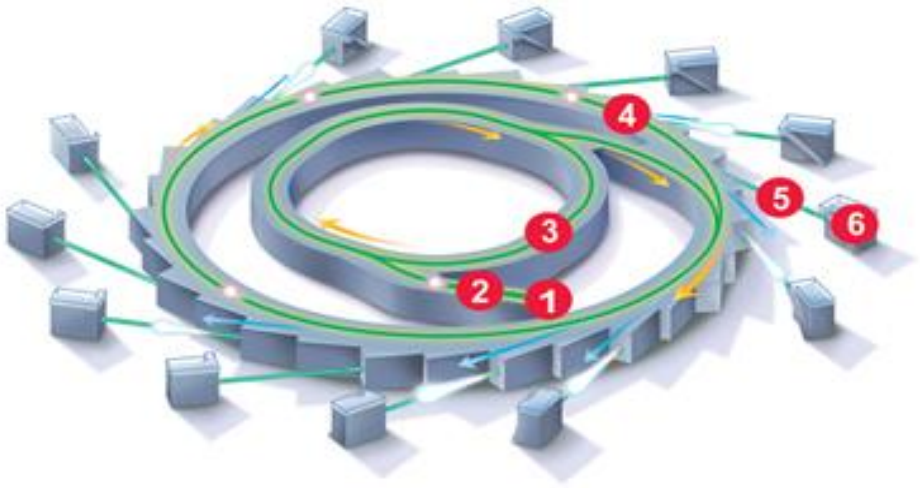

Figure 2.9. Typical Synchrotron facility. 1.electron gun, 2. linac, 3. booster ring, 4. storage ring, 5. beamline, 6. end station.
(http://www.schoolofthinking.org)

For non-relativistic energies, the radiation emitted from the electron is in the classical dipole pattern, illustrated schematically in Figure 2.10 (a). The radiation emitted is distributed over a wide range of angles. Since the electron is in a circular orbit, the acceleration is perpendicular to the direction of motion, and as a result, the dipole pattern has a maximum in the direction of motion (Heald, 1988).

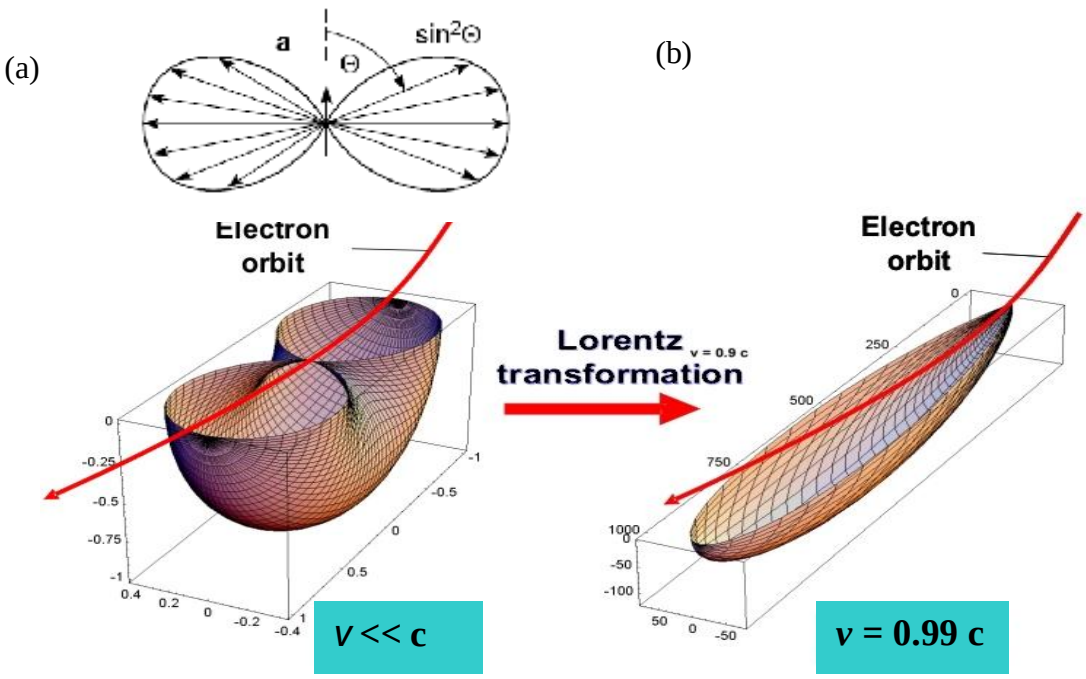

Figure 2.10.(a) non-relativistic electron moving in a magnetic field emits in the classical manner into two lobes with power proportional to $\sin^2\theta$,, where θ, is the angle between the emission direction and the acceleration vector. In panel (b), the beaming effect on the radiation is illustrated for a relativistic photon (www.physik.uni-kiel.de/kfs/infos/Quellen/sync)

However, as the electron speed reaches the speed of light, relativistic effects must be considered. The relativistic effect compresses the dipole pattern along the direction of motion resulting in a concentrated dipole tangential to the electron orbit (Margaritondo, 1988). This is illustrated in Figure 2.10 (b).

The spectral distribution of bending magnet radiation is a function of the storage ring energy and the radius of curvature. The curvature can also be expressed as the bending magnet strength. The source characteristics are defined by the critical photon energy, given by

$$E_c(keV) = 0.6650\, E_e^2(GeV)B(T) \qquad (2.9.)$$

where B is the magnet strength in teslas and E_e is the storage ring energy in GeV and E_c is the critical photon energy in keV. This is the value at which half of the irradiated power is emitted at photon energies above the critical energy and half below the critical value (Margaritondo, 1988). For the APS (Advenced Photon Source) bending magnets, the critical energy is 19.5 keV giving a peak flux of approximately 9.6 x 10^{13} photons/s/mrad^2/0.1% bw at 16.3 keV (Bizek, 1996). A diagram of the energy spectrum (in terms of brilliance) for the APS bending magnet and other synchrotron sources is given in Figure 2.11.

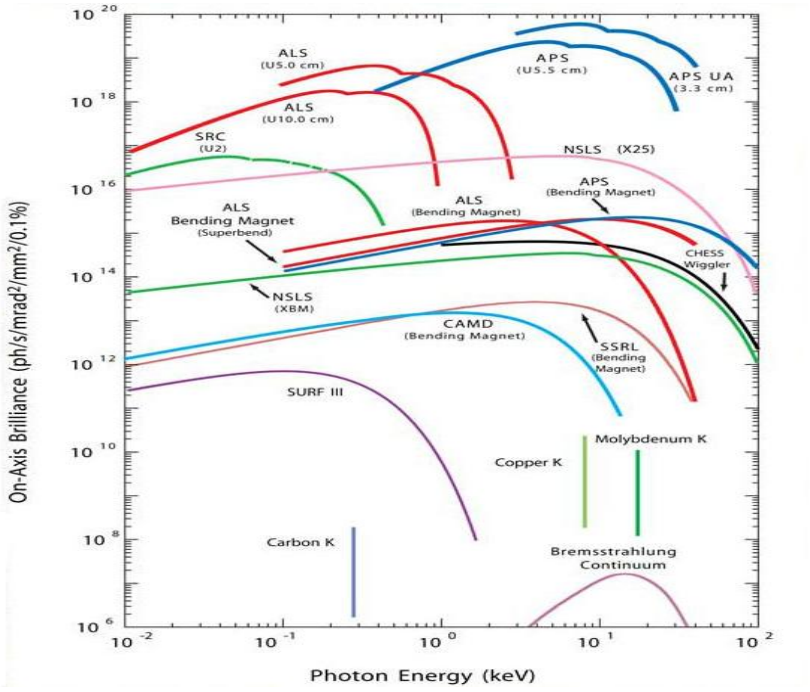

Figure 2.11. Photon brilliance as a function of X-ray energy for conventional and Synchrotron radiation sources.
(www.aps.anl.gov/.../Images/billcurvesREV.jpg)

Except that bending magnet photon flux can also be harnessed from insertion devices placed into the electron orbit of the storage ring. These are series of opposing polarity magnets placed into straight sections of the storage ring where there are no bending magnets. The series of alternating magnetic fields causes the electron beam to “wiggle” or “undulate” in the device around its normal trajectory. These insertion devices are called Undulator and Wiggler magnet respectively. A wiggler contains

high magnetic fields and forces the electrons through extremely tortuous paths. Each oscillation creates synchrotron radiation, concentrated along the major axis of the insertion device. Wiggler radiation does not produce interference effects between the individual poles, so the spectrum produced is essentially the equivalent superposing a number of bending magnets that is roughly two times the number of periods in the wiggler array. The spectral distribution characteristics are also similar to that of the bending magnet source. The undulator insertion device has a larger number of periods in the array and weaker magnetic fields. As a result, interference effects create radiation that is highly concentrated (*i.e.*, very small bandwidth) around specific energies and its harmonics. This can be tuned by the user to the desired energy by altering the magnetic field strength in the undulator. In practice, this is done by changing the gap distances between the poles of the magnets in the array (Margaritondo, 1988). The bandwdith of the undulator can be increased by tapering the gap of the array. This causes the electron to go through a series of oscillations with varying periods, creating a more continuous spectrum (Lai *et. al.*, 1993).Three forms of synchrotron radiation is illustrated in figure 2.12.

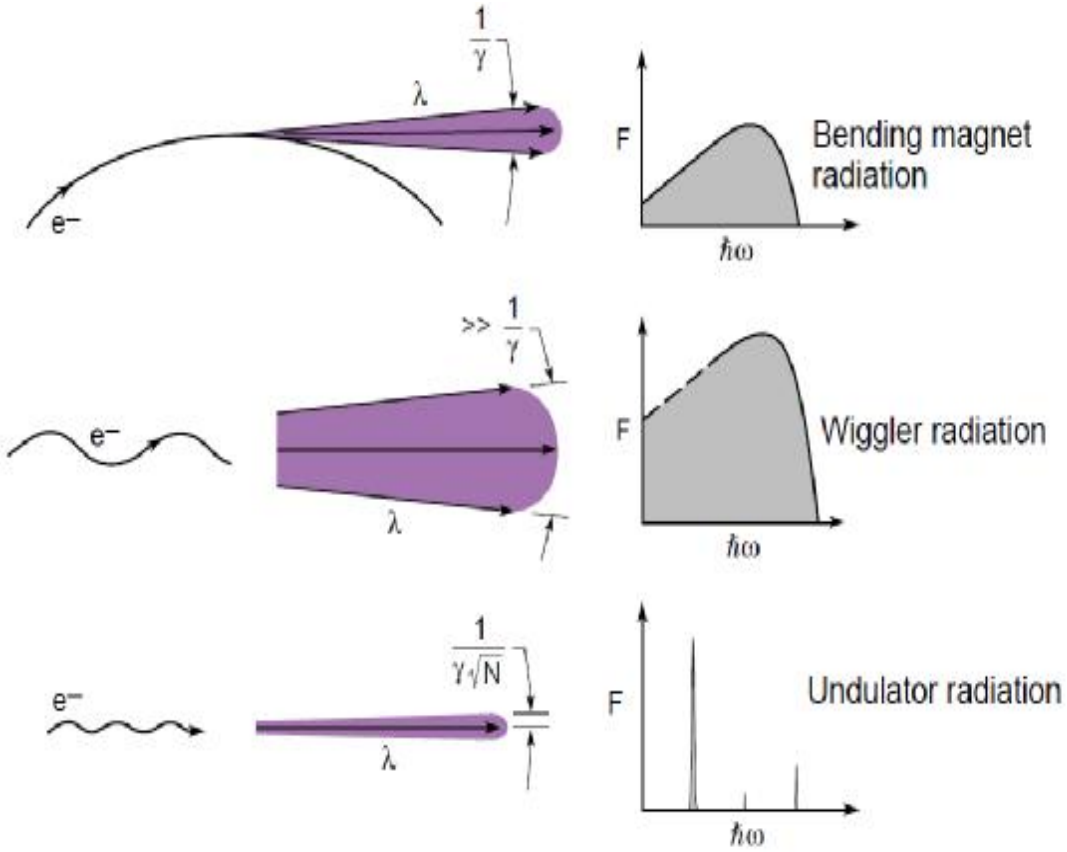

Figure 2.12. Three Forms of Synchrotron Radiation (Atwood,1999).

Now, we must do determinate the radiation of these insertion devices briefly.

2.6.1. Bending Magnet Radiation

Bending magnet radiation is sometimes described as a sweeping ”searchlight” analogous to the headlight of a toy train on a circular track. Bending magnet is illustrated in fig.2.13.

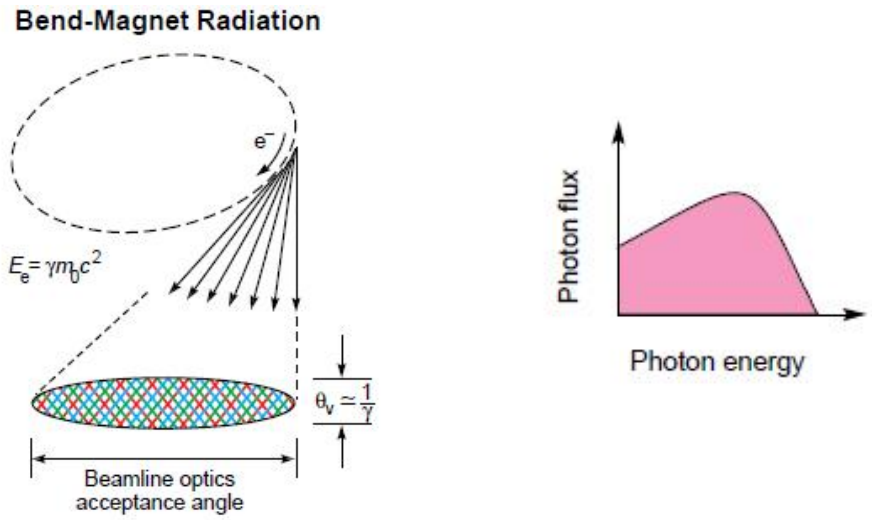

Figure 2.13.Illustration of a bending magnet. At each deflection of the electron path a beam of light is produced. The effect is similar to the sweeping of a search light. (Atwood,1999)

This searchlight effect is a general manifestation associated with radiation from relativistic particles undergoing acceleration. An electron experiencing radial acceleration as it travels around a circle emits radiation through a broad angular pattern as seen in its frame of reference. However , angular patterns are very much compressed upon Lorentz transformation from one frame of reference (that moving the electron) to another (the laboratory frame of the observer) when the relative motion is highly relativistic. In appendix 1 it is shown that angles measured from the direction of motion are related by

$$\tan q = \frac{\sin q^*}{g(\cos q^* + b)} \qquad (2.10.)$$

where q^* is observed in the frame of reference moving with the electron ,q is in the laboratory frame , $b \equiv$ v/c (where v is the relative velocity between frames and c is the velocity of light), and $\gamma \equiv 1/(1-v^2/c^2)^{1/2} \equiv 1/(1-b^2)^{1/2}$.For highly relativistic electrons b approaches unit , and $\gamma >> 1$. Thus for arbitrarily large emission angles q` , in the lectron frame , the radiation is folded into a narrow forward radiation cone of half angle

$$q@\frac{1}{2g} \qquad (2.11.)$$

leading to the description of synchrotron radiation as being concentrated in a narrow "search light beam".As an electron traverses a curved path , radiation is emitted tangentially, as seen in Fig 2.14. in a narrow radiation cone of half width *q @ 1/2g*.(Atwood,1999)

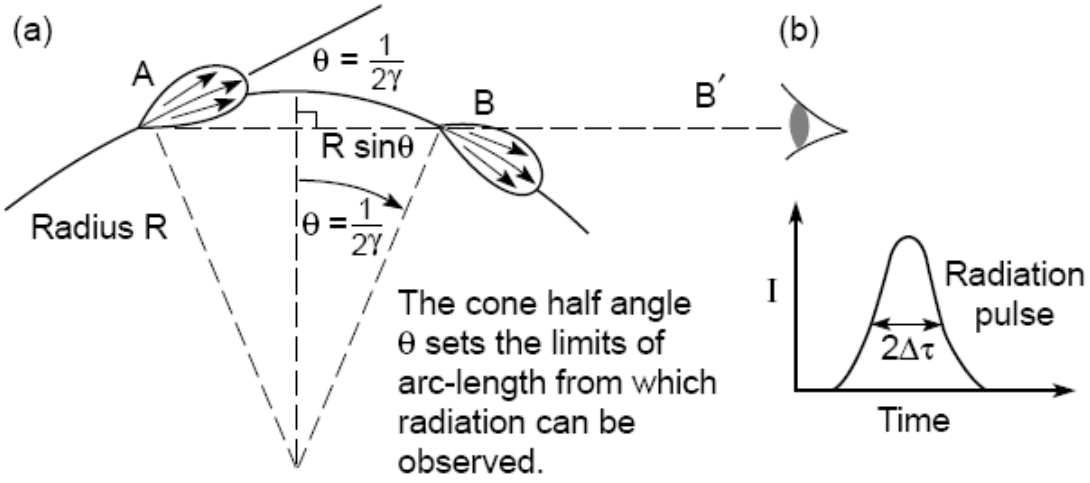

Figure 2.14.(a) A schematic of bending magnet radiation illustrating the "searchlight" effect (b) The time width of the observed radiation pulse is determined by transit time differences between radiation and electrons between A and B (Atwood,1999)

For electrons circulating in a ring , we can Heisenberg`s uncertainty principle , *DE.Dt ³ ħ/2* , where *Dt* is the time duration during which one detects radiation , and *DE* is the uncertainty in observed photon energies. We begin by estimating the detected pulse duration 2*Dt* , of radiation emitted by a short bunch of electrons following a circular trajectory of radius R. We estimate the time extent of the observed signal by considering a detector at point B or equivalently further to the right at B′. As the electron comes within an angle *q @ 1/2g* of the horizon at point A , the dedector will be in the path of emitted photons. These photons will be detected after a transit time of the light , τ_r. The signal will continue until the electron reaches point B, beyond which the radiation cone has turned too far to permit

reception by our dedector. The electron will reach point B after a transit time around the bend, τ_e .the puls width ,$\Delta\tau$ shown in fig.2.14 (b) is the difference between these two transit times , i.e. the dedector decets radiation after a time τ_r , and stops dedecting radiation at τ_e

Following this outline , we see that

$$2Dt = t_e - t_r \tag{2.12.}$$

$$2Dt = \frac{arclength}{v} - \frac{radiationpath}{c} \tag{2.13.}$$

$$2Dt \; @ \; \frac{R.2q}{v} - \frac{2R\sin q}{c} \tag{2.14.}$$

Noting that $q \; @ \; 1/2g$, making a small angle approximation for $\sin q \; @ \; q$, and substituting $v = bc$, one obtain

$$2Dt @ \frac{R.}{gv} - \frac{R}{gc} = \frac{R}{l}\left(\frac{1}{v} - \frac{1}{c}\right) \tag{2.15.}$$

Writing $v = bc$

$$2Dt \; @ \; \frac{R.}{gbv} - - = \frac{R}{l}(1 - b) \tag{2.16.}$$

Noting that

$$g \cong \frac{1}{\sqrt{1 - b^2}} \tag{2.17.}$$

$$\gamma^2 = \frac{1}{1-b^2} = \frac{1}{(1-b)(1+b)} \qquad (2.18.)$$

And thus for b = v/c approaching unity

$$1- b @ \frac{1}{2g^2} \qquad (2.19.)$$

The expression for the duration of the radiation pulse becomes

$$2Dt @ \frac{R.}{2cg^3} \qquad (2.20.)$$

This can be expressed as an anticipated photon energy spread through the use oh Heisenberg`s uncertainty principle and an expression for the radius of curvature R. From the uncertainty principe,

$$DE.Dt \; ³ \; \hbar/2 \qquad (2.21.)$$

Combining this with the expression in eq.(1) for the pulse duration , we see that the photons will have an energy spread of order

$$DE ³ \frac{2\mathbf{h}cg^3}{R} \qquad (2.22.)$$

To better appreciate the photon energies implied by eq.(2.22) it is useful to replace the electron radius of curvature R with an expression involving γ and the magnetic field. For electrons crossing a perpendicular magnetic field , as a bending magnet , the relativistically correct form of the equation of motion can be written as

$$\boldsymbol{F} = \frac{d\vec{P}}{dt} = -e\,\vec{\mathbf{r}}\,\vec{v}x\vec{B} \qquad (2.23.)$$

Where **p** = γm**v** is the momentum, m is the electron mass, γ is the Lorentz factor , **v** is the velocity , and **B** is the magntic flux density. For electron motion in a uniform magnetic field , the electron energy and thus γ is a constant , so that only the direction of **v** changes , not its magnitude .To see this we write the rate of change of electron energy as

$$\frac{dE}{dt} = \vec{v}.\vec{F} = -e\vec{v}.(\vec{v}x\vec{B}) = 0 \qquad (2.24.)$$

which is zero by vector identity (see appendix 2). Thus the electron energy , which can be written , is a constant

$$\frac{dE_e}{dt} = \frac{d}{dt}(gmc^2) = 0 \qquad (2.25.)$$

thus g , and therefore the scalar magnitude v of the velocity , are both constant . y he equation of motion can be rewritten as

$$gm\frac{d\vec{v}}{dt} = -e\vec{v}x\vec{B} \qquad (2.26.)$$

Since the magnitude of **v** is constant , the magnitude of the acceleration is also , equal to evB/γm , in a plane perpendicular to **B** . this corresponds to motion along a circle , with centripetal acceleration v^2/R , so that the scalar form of the equation of motion becomes

$$gm(-\frac{v^2}{R}) = -evB \qquad (2.27.)$$

Solving for the radius of curvature , we have

$$R = \frac{gmv}{eB} \tag{2.28.}$$

Or for highly relativistic electrons (v≅c)

$$R \approx \frac{gmc}{eB} \tag{2.29.}$$

Using this in eq.(2.22) the rms spread of photon energies for bending magnet radiation becom

$$\Delta E \propto \frac{2e\hbar Bg^2}{m} \tag{2.30.}$$

Which we note depends on the electron charge to mass ratio *e/m*,and the product Bg^2 .If we substitute values for *e*,ħ and *m* eq. (2.30) indicates photon energies in the keV range (nanometer wavelengths) for typicial values of *g* and *B* found in modern storage rings ,e.g. *g* of several thousand and *B* of 1T or more . For higly relativistic electrons it is convenient to express the electron energy in terms of *g* and the electron rest energy, mc^2, as

$$g = \frac{E_e}{mc^2} = 1957\ E_e\ (\text{GeV}) \tag{2.31.}$$

Where on right side we used the fact that the electron rest energy is 0.5110 MeV, and expressed the electron enery E_e in GeV. (Atwood,1999)

The description of expected photon energy spread obtained ,eq.(2.30), is based on elatively simple arguments involving Heisenberg`s uncertainty principle .It is valuable in that it provides a measure of the expected photon energies radiated by accelerated charges moving at relativistic speeds , and givens a functional dependence in terms of Bg^2 . the numerical factor obtained by this argument is,

however ,is somewhat arbitrary in that it depends on the angular distrubition of radiation embodied in our assumption that *q @ 1/2g*. A more precise description of the photon energy distribution , obtained by a rigorous solution of Maxwell`s equations for a relativistic electron in a uniform magnetic field introduces instead a factor of 3/2 and a more useful definition of *DE* . The results somewhat complex , involving modified Bessel functions of the second kind (Jackson, 1978).

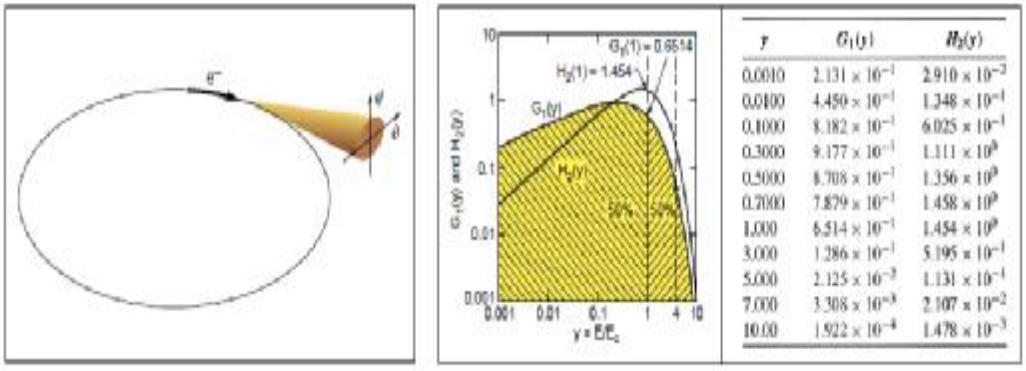

y	$G_1(y)$	$H_2(y)$
0.0010	2.131×10^{-1}	2.910×10^{-2}
0.0100	4.450×10^{-1}	1.348×10^{-1}
0.1000	8.182×10^{-1}	6.025×10^{-1}
0.3000	9.177×10^{-1}	1.111×10^{0}
0.5000	8.708×10^{-1}	1.356×10^{0}
0.7000	7.879×10^{-1}	1.458×10^{0}
1.000	6.514×10^{-1}	1.454×10^{0}
3.000	1.286×10^{-1}	5.195×10^{-1}
5.000	2.125×10^{-2}	1.131×10^{-1}
7.000	3.308×10^{-3}	2.107×10^{-2}
10.00	1.922×10^{-4}	1.478×10^{-3}

Figure 2.15. Bending magnet critical photon energy and Bessel function dependence (Atwood,1999)

Defining *q* as the in –plane observation angle for radiation from relativistic electrons traveling in a circular path , and *y* as the out of plane (vertical) angle , Kimshows that the photon flux F_B for bending magnet radiation is given on axis by

$$\frac{d^3 F_B}{dq\,dy\,dw/w}\Big|_{Y=0} = 1.33x10^{13}\, E^2_e(GeV)\, I\,(A)\, H_2\,(E/E_c)\, \frac{\frac{photon}{s}}{mrad^2.(0.1\%BW)} \qquad (2.32.)$$

where the electron enery E_e is in GeV , the average current *I* is in amperes, where the units of relative spectral bandwith *dw/w* are expressed non- dimensionally as a factor of 10^{-3} , or 0.1% BW, and the function

$$H_2(y) = y^2\, K^2_{2/3}(y/2) \qquad (2.33.)$$

is a modified Bessel function dependence , tabulated and shown graphically in figure 2.15. the ratio E/E_c is the photon energy normalized with respect to critical photon energy

$$E_c = \frac{3e\mathbf{h}Bg^2}{2m} \tag{2.34.}$$

Equation (2.34) can be written in practical units as

$$E_c\,(keV) = 0.665\ E_e^2\,(GeV)\ B(T) \tag{2.35.}$$

where the critical photon energy is in keV , the electron beam energy is given in GeV , and the magnetic field in teslas. The corresponding *critical wavelength* is

$$l_c = \frac{4pmc}{3eBg^2} \tag{2.36.}$$

Which can be written in practical units of nanometers, GeV, and teslas as

$$l_c(nm) = \frac{1.864}{E_e^2(GeV)B(T)} \tag{2.37.}$$

Note that the critical photon energy given in eq.(2.34) is well within tha range of photon energies estimated by eq.(2.30) on the basis of relativistic angular transformations and Heisenberg uncertainty arguments.

The critical energy is in fact a very useful parameter for characterizing synchrotron radiation from relativistic electrons as traverse the fields a bending magnet. For example, Advanced Photon Source (APS) at Argonne National Laboratory in Illinois , with a beam energy of 7.0 GeV and a bending magnet field strength of 0.60 T , has a critical photon energy of 19.5 keV and a critical wavelength of 0.064 nm (0.64Å).

Bending magnet has advantage which are covers broad spectral range, least expensive, most accessable and disadvantages which are limited coverage of hard x-rays, not as bright as undulator (Atwood,1999).

2.6.2.Undulator Magnet Radiation

The electron beam is periodically deflected by weak magnetic fields. Similar to antenna radiation the particle emits radiation at the wavelength of its periodic motion in the undulator. To the particle this wavelength is the undulator period length (λ) divided by γ due to relativistic Lorentz contraction. In the laboratory system this wavelength appears to the observer further reduced by another factor γ due to the Doppler effect. The undulator period length of the order of cm`s is thus reduced by a factor γ^2 (10^6 - 10^8) to yield short wavelength radiation in the VUV and x-ray regime. The spectral resolution of the radiation is proportional to the number of undulator periods and its wavelength can be shifted by varying the magnetic field. Most radiation is emitted within the small angle of $1/\gamma\sqrt{N}$ (Helmut Wiedemann, 1998). Undulator radiation is quasi monochromatic and highly directional, approximating many of the desired properties of an x-ray laser.

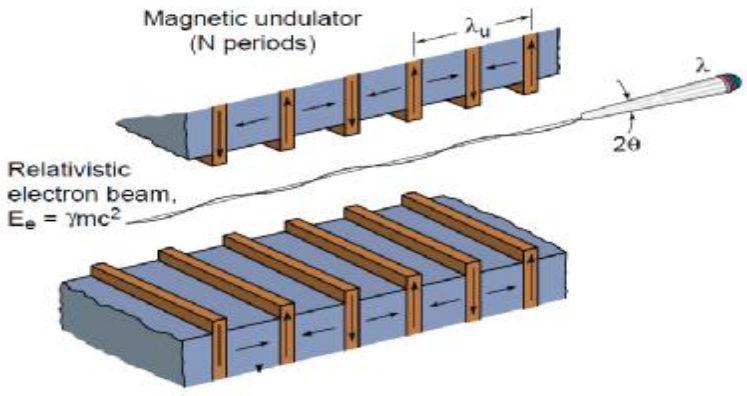

Figure 2.16. Systematic figure of Undulator magnet. (Atwood,1999)

Magnetic fields in the periodic undulator cause the electrons to oscillate and thus radiate. These magnetic fields also slow the electrons axial (z) velocity somewhat, reducing both the Lorentz contraction and the Doppler shift, so that the observed radiation wavelength is not quite so short. The force equation for an electron is

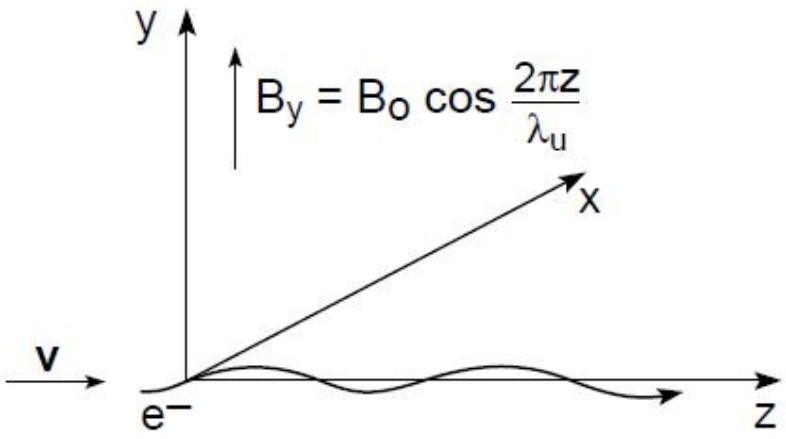

Figure 2.17. Electron motion in a periodic magnetic field (Atwood,1999)

$$\frac{d\mathbf{p}}{dt} = -e(\mathbf{E} + \mathbf{v}x\mathbf{B}) \qquad 2.38.)$$

where $\mathbf{p} = \gamma m\mathbf{v}$ is the momentum. The radiated fields are relatively weak so that

$$\frac{d\mathbf{p}}{dt} = -e(\mathbf{v}x\mathbf{B}) \qquad 2.39.)$$

Taking to first order $v \cong v_z$, motion in the x-direction is

$$mg\frac{dv_x}{dt} = +ev_z B_y \qquad (2.40.)$$

$$mg\frac{dv_v}{dt} = +e\frac{dz}{dt}B_o \cos(\frac{2pz}{l_u})(0 \le z \le N l_u) \qquad (2.41.)$$

$$mgdv_x = = edzB_o \cos(\frac{2pz}{l_u}) \tag{2.42.}$$

Integrating both sides,

$$mgv_x = = eB_o \frac{l_u}{2p} \int \cos(\frac{2pz}{l_u}).d(\frac{2pz}{l_u}) \tag{2.43.}$$

$$mgv_x = = eB_o \frac{l_u}{2p} \sin(\frac{2pz}{l_u})$$

(2.44)

$$v_x = = \frac{Kc}{g} \sin(\frac{2pz}{l_u}) \tag{2.45.}$$

$$K \equiv \frac{eB_0 l_u}{2pmc} = 0.9337 B_0(T) l_u(cm) \tag{2.46.}$$

is the non-dimensional "magnetic deflection parameter." The "deflection angle", θ, is

$$\theta = \frac{v_x}{v_z} \cong \frac{v_x}{c} = \frac{K}{g} \sin k_u z \tag{2.47.}$$

In a magnetic field γ is a constant; to first order the electron neither gains nor looses energy.

$$\gamma \equiv \frac{1}{\sqrt{1-\frac{v^2}{c}}} = \frac{1}{\sqrt{1-\frac{v_x^2+v_z^2}{c^2}}} \tag{2.48.}$$

Thus,

$$\frac{v_z^2}{c^2} = 1 - \frac{1}{g^2} - \frac{v_x^2}{c^2} \tag{2.49.}$$

$$\frac{v_z^2}{c^2} = 1 - \frac{1}{g^2} - \frac{K^2}{g^2}\sin^2\left(\frac{2pz}{l_u}\right) \tag{2.50.}$$

Taking the square root, to first order in the small parameter K/γ

$$\frac{v_z}{c} = 1 - \frac{1}{2g^2} - \frac{K^2}{2g^2}\sin^2\left(\frac{2pz}{l_u}\right) \tag{2.51.}$$

Using the double angle formula $\sin 2k_u z = (1 - \cos 2k_u z)/2$, where $k_u = 2\pi/\lambda_u$,

$$\frac{v_z}{c} = 1 - \frac{1 + K^2/2}{2g^2} + \frac{K^2}{4g^2}\cos\left(2.\frac{2pz}{l_u}\right) \tag{2.52.}$$

The first two terms show the reduced axial velocity due to the finite magnetic field (*K*). The last term indicates the presence of harmonic motion, and thus harmonic frequencies of radiation.The electron “sees” a Lorentz contracted period

$$l` = \frac{l_u}{g} \tag{2.53.}$$

and emits radiation in its frame of reference at frequency

$$f` = \frac{c}{l`} = \frac{cg}{l_u} \tag{2.54.}$$

Observed in the laboratory frame of reference, this radiation is Doppler shifted to a frequency

$$f` = \frac{f`}{g(1-b\cos q)} = \frac{c}{l_u(1-b\cos q)} \tag{2.55.}$$

On-axis (θ = 0) the observed frequency is

$$f = \frac{c}{l_u(1-b)} \tag{2.56.}$$

By definition,

$$g = \frac{1}{\sqrt{1-b^2}}; g^2 = \frac{1}{(1-b)(1+b)} \approx \frac{1}{2(1-b)} \tag{2.57.}$$

Thus,

$$f = \frac{2g^2 c}{l_u} \tag{2.58.}$$

and the observed wavelength is

$$l = \frac{c}{f} = \frac{l_u}{2g^2} \tag{2.59.}$$

For $\theta \neq 0$, take

$$cosq = 1 - \frac{q^2}{2} + ... \tag{2.60.}$$

then ,

$$f = \frac{c}{l_u(1 - b\cos q)} \tag{2.61.}$$

$$f = \frac{c/l_u}{1 - b(1 - q^2/2 + ...)} = \frac{c/l_u}{1 - b + bq^2/2 - .....} = \frac{c/(1-b)l_u}{1 - bq^2/2(1-b).....} \tag{2.62.}$$

$$f = \frac{2g^2 c/l_u}{1 + g^2 q^2} = \frac{2g^2 c}{l_u(1 + g^2 q^2)} \tag{2.63.}$$

The observed wavelength is then

$$l = \frac{l_u}{2g^2}(1 + g^2 q^2) \tag{2.64.}$$

exhibiting a reduced Doppler shift off-axis, i.e., longer wavelengths.This is a simplified version of the " Undulator Equation ".

Averaging the z-component of velocity over a full cycle (or N full cycles) gives

$$\frac{v_z}{c} = 1 - \frac{1 + K^2/2}{2g^2} \tag{2.65.}$$

We can use this to define an effective Lorentz factor γ* in the axial direction

$$g^* = \frac{g}{\sqrt{1 + K^2/2}} \tag{2.66.}$$

As a consequence, the observed wavelength in the laboratory frame of reference is modified from Eq. (5), taking the form

$$l = \frac{l_u}{2g^{*2}}(1+g^{*2}q^2) \tag{2.67.}$$

that is, the Lorentz contraction and relativistic Doppler shift now involve γ* rather than γ

$$l = \frac{l_u}{2g^2}(1+\frac{K^2}{2})(1+\frac{g^2}{1+K^2/2}q^2) \tag{2.68.}$$

$$l = \frac{l_u}{2g^2}(1+\frac{K^2}{2}+g^2q^2) \tag{2.69.}$$

where K ≅ e Bo $\lambda_u/2\pi$mc. This is the ***undulator equation***, which describes the generation of short(x-ray) wavelength radiation by relativistic electrons traversing a periodic magnet structure, accounting for magnetic tuning (K) and off-axis (γ_θ) radiation. In practical units

$$l(nm) = \frac{1.306\, l_u(cm)(1+\frac{K^2}{2}+g^2q^2)}{E_e^2(GeV)} \tag{2.70.}$$

With electrons executing N oscillations as they traverse the periodic magnet structure, and thus radiating a wavetrain of N cycles, it is of interest to know what angular cone contains radiation of relative spectral bandwidth

$$\frac{\Delta l}{l} = \frac{1}{N} \tag{2.71.}$$

Write the undulator equation twice, once for on-axis radiation (θ = 0) and once for wavelengthshifted radiation off-axis at angle θ:

$$l_0 + \Delta l = \frac{l_u}{2g^2}(1 + g^2 q^2) \tag{2.72.}$$

$$l_0 = \frac{l_u}{2g^2} \tag{2.73.}$$

$$\frac{\Delta l}{l} = g^2 q^2 \tag{2.74.}$$

Combining the two equations (2.71and 2.73)
defines θ_{cen} :

$$g^2 q^2_{cen} = \frac{1}{N}, \text{ which gives } q_{cen} \approx \frac{1}{l\sqrt{N}} \tag{2.75.}$$

This is the half-angle of the "central radiation cone", defined as containing radiation of $\Delta\lambda/\lambda = 1/N$. (Atwood,1999).
Also the average power radiated into the central cone , for a single electron is given by

$$\overline{P}_{cen} \cong \frac{pe^2 cg^2}{e_o l_u^2 N} \frac{K^2}{(1 + K^2/2)^2} \tag{2.76.}$$

With an associated of $\Delta\lambda/\lambda = 1/N$ and a redition cone half angle of $1/\gamma^* \sqrt{N}$. This result is generally valid $K \leq 1$. For N_e electrons radiating independently within the undulator

$$Ne = IL/ec, \text{ where } L = N\lambda u \tag{2.77.}$$

The power radiated into the central cone is then

$$\overline{P}_{cen} \cong \frac{pe\ g^2 I}{e_o l_u} \frac{K^2}{(1+K^2/2)^2} \qquad (K \le 1) \tag{2.78.}$$

Our formula for calculated power in the central radiation cone ($\theta_{cen} = 1/\gamma^* N$, $\Delta\lambda/\lambda = 1/N$) is strictly valid for $K << 1$. This restriction is due to our neglect of K^2 terms in the axial velocity v_z. The P_{cen} formula, however, indicates a peak power at $K=\sqrt{2}$, suggesting that we explore extension of this very useful analytic result to somewhat higher K values. Kim* has studied undulator radiation for arbitrary K and finds an additional multiplicative factor, $f(K)$, which accounts for energy transfer to higher harmonics(Atwood,1999):

$$\overline{P}_{cen} \cong \frac{pe\ g^2 I}{e_o l_u} \frac{K^2}{(1+K^2/2)^2} f(K) \tag{2.79.}$$

Where

$$f(K) = [J_0(x) - J_1(x)]^2 \tag{2.80.}$$

$$x = K^2/4(1+ K^2/2) \tag{2.81.}$$

$$f(K)=1-x-x^2/4+3x^3/8 \tag{2.82.}$$

Table 2.2. The multiplicative correction factor *f(K)* that enables the low *K* analytic formulation of undulator central cone power (Eq.2.79) to be extended to higher *K*-values (Atwood,1999)

K	x	f(K)
0	0	1.00
0.5	0.0556	0.944
1.0	0.1667	0.828
$\sqrt{2}$	0.2500	0.740
1.5	0.2647	0.725
2	0.3333	0.653
2.5	0.3788	0.606

From the undulator equation

$$l = \frac{l_u}{2g^2}\left(1+\frac{K^2}{2}+g^2q^2\right) \tag{2.83.}$$

On axis, θ = 0, and with $f\lambda = c$

$$f = 2g^2c / l_u\left(1+\frac{K^2}{2}\right) \tag{2.84.}$$

In terms of photon energy (on-axis)

$$\mathbf{h}w = 4p\mathbf{h}g^2c / l_u\left(1+\frac{K^2}{2}\right) \tag{2.85.}$$

We can now replace $K^2/(1 + K^2/2)^2$ in P_{cen} by an expression involving $\hbar\omega$.

Introducing the limiting photon energy $\hbar\omega_o$, corresponding to $K = 0$,

$$\mathbf{h}w_o = 4p\mathbf{h}g^2 c l_u \tag{2.86.}$$

then,

$$\overline{P}_{cen} \cong \frac{pe\ g^2 I}{e_o l_u} \frac{\mathbf{h}w}{\mathbf{h}w_o}(1-\frac{\mathbf{h}w}{\mathbf{h}_o}) f(\mathbf{h}w/\mathbf{h}w_o) \tag{2.87.}$$

Where

$$f(\mathbf{h}w/\mathbf{h}w_o) \cong \frac{7}{16} + \frac{5}{8}\frac{\mathbf{h}w}{\mathbf{h}w_o} - \frac{1}{16}(\frac{\mathbf{h}w}{\mathbf{h}w_o})^2 + ... \tag{2.88.}$$

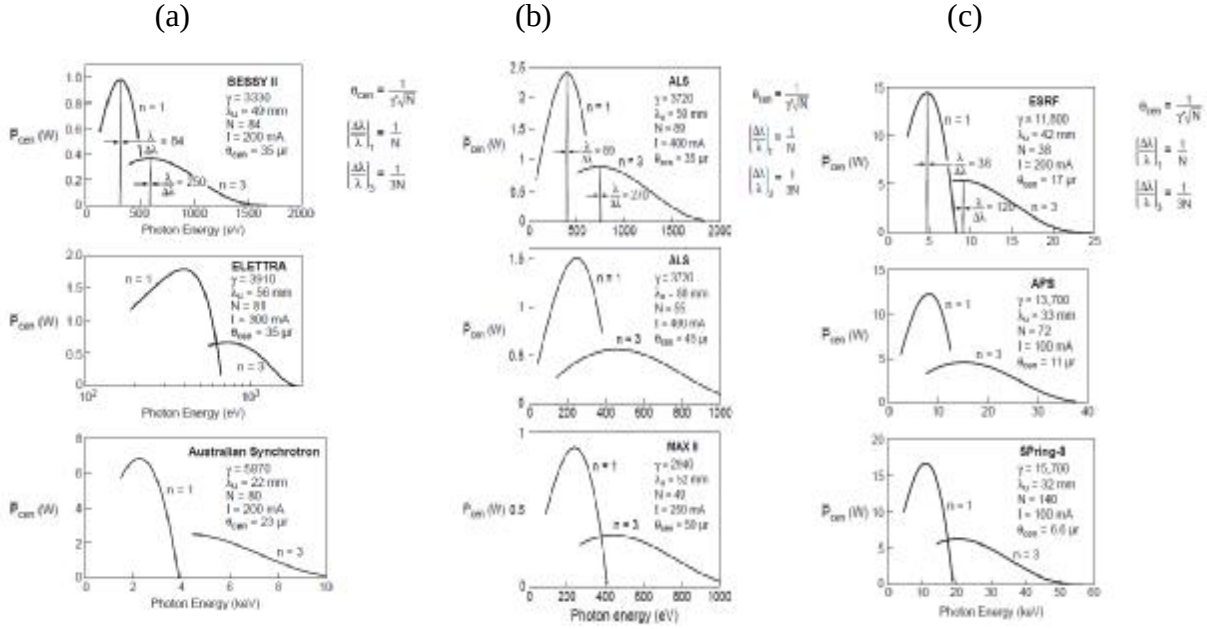

Figure 2.18. (a) and (b) Power in the Central Radiation cone for soft x-ray undulators
(c) Power in the Central Radiation cone for x-ray undulators
(Atwood,1999)

Undulator radiation ($K \leq 1$) has narrow spectral lines, high spectral brightness, partial coherence.

2.6.3. Wiggler Magnet Radiation

Increasing the magnetic field strength causes the pure sinusoidal transverse motion of electrons in an undulator to become distorted due to relativistic effects generating higher harmonics of the single wavelength undulator radiation. The monochromatic undulator spectrum therefore changes into a line spectrum. For very strong fields many harmonics are generated which eventually merge into a continuous spectrum from IR to hard x-rays. The spectral intensity varies little over a broad wavelength range and drops off exponentially at photon energies higher than the critical photon energy, $\varepsilon_{crit} \sim Bg^2$. Compared to bending magnet radiation, wiggler radiation is enhanced by the number of magnet poles and is well collimated within an angle of K/g, or a few mrad.

We have seen in the preceding sections that as K increases toward unity the radiated power in higher harmonics grows rapidly. Indeed , for K >> 1 analysis shows the emergence of a large number of ever stronger harmonics. Extending to ever higher photon energies. Figure 2.20 shows the development of this harmonic structure for increasing values of the magnetic deflection parameter K (Atwood,1999).

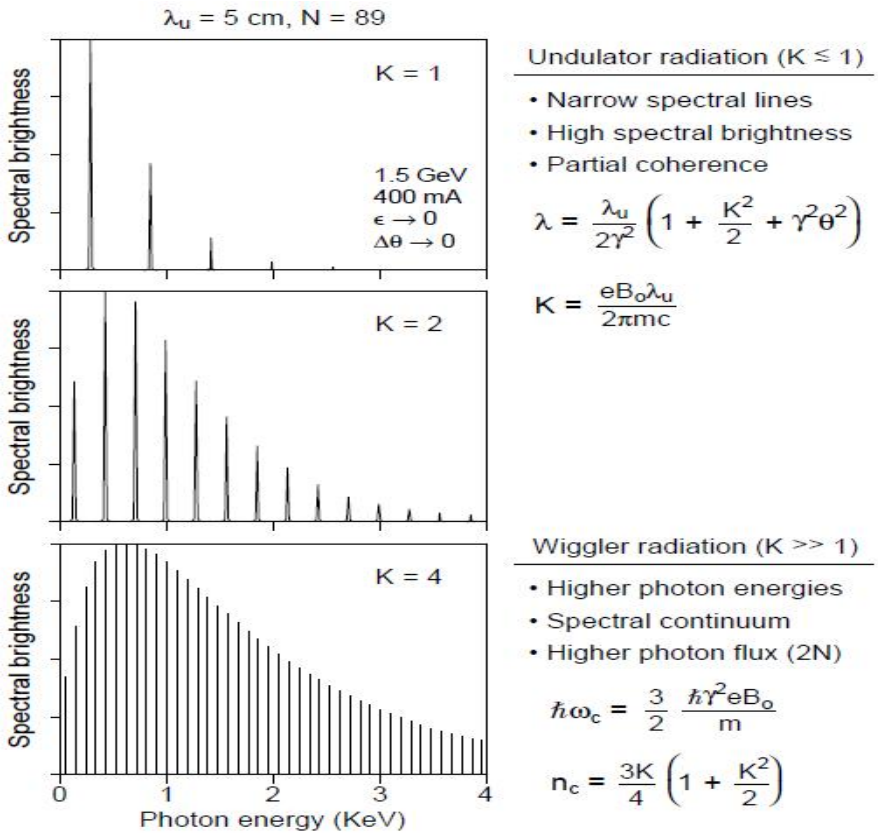

Figure 2.19. The transition from undulator radiation ($K \leq 1$) to wiggler radiation ($K >> 1$) is illusturated (Atwood,1999).

We have approached the subject of radiation from relativistic electrons traversing periodic magnet structures from a small K theory of undulator radiation . While this has clear advantages , the approximations made are not valid for large K wiggler radiation. For wiggler radiation with $K >> 1$ the motion becomes significantly more complex . At very high $K >> 1$, the radiated energy appears in very high harmonics, and at rather large horizontal angles $\theta \cong \pm K/\gamma$. Because the emission angles are large, one tends to use larger collection angles, which tends to spectrally merge nearby harmonics. The result is a continuum at very high photon energies, similar to that of bending magnet radiation, but increased by 2N (the number of magnet pole pieces).

$$E_c = \hbar w_c = \frac{3e\hbar B\gamma^2}{2m}; n_c = \frac{3K}{4}(1+\frac{K^2}{2}) \quad (2.89.)$$

$$\frac{d^3 F}{dq dy \, dw/w} = 2.65x10^{13} \, N \, E^2_e(GeV) \, I \, (A) \, H_2 \, (E/E_c) \, \frac{\frac{photon}{s}}{mrad^2.(0.1\%BW)} \quad (2.90.)$$

$$\frac{d^3 F}{dq dy \, dw/w} = 4.92x10^{13} \, N \, E^2_e(GeV) \, I \, (A) \, G_1 \, (E/E_c) \, \frac{\frac{photon}{s}}{mrad^2.(0.1\%BW)} \quad (2.91.)$$

Also it can see typical parameters for synchrotron radiation for some synchrotron facilities in table 2.3.

Table 2.3. Typical parameters for Synchrotron Radiation (Atwood,1999).

Facility	ALS	ELETTRA	Australian Synchrotron	APS
Electron energy	1.90 GeV	2.0 GeV	3.0 GeV	7.00 GeV
γ	3720	3910	5871	13,700
Current (mA)	400	300	200	100
Circumference (m)	197	259	216	1100
RF frequency (MHz)	500	500	500	352
Pulse duration (FWHM) (ps)	35-70	37	~100	100
Bending Magnet Radiation:				
Bending magnet field (T)	1.27	1.2	1.31	0.599
Critical photon energy (keV)	3.05	3.2	7.84	19.5
Critical photon wavelength	0.407 nm	0.39 nm	1.58 Å	0.636 Å
Bending magnet sources	24	12	28	35
Undulator Radiation:				
Number of straight sections	12	12	14	40
Undulator period (typical) (cm)	5.00	5.6	22.0	3.30
Number of periods	89	81	80	72
Photon energy ($K = 1$, $n = 1$)	457 eV	452 eV	2.59 keV	9.40 keV
Photon wavelength ($K = 1$, $n = 1$)	2.71 nm	2.74 nm	0.478 nm	1.32 Å
Tuning range ($n = 1$)	230-620 eV	2.0-6.7 nm	0.319-0.835 nm	3.5-12 keV
Tuning range ($n = 3$)	690-1800 eV	0.68-2.2 nm	0.106-0.278 nm	10-38 keV
Central cone half-angle ($K = 1$)	35 μrad	35 μrad	23 μrad	11 μrad
Power in central cone ($K = 1$, $n = 1$) (W)	2.3	1.7	6.6	12
Flux in central cone (photons/s)	3.1×10^{16}	2.3×10^{16}	1.6×10^{16}	7.9×10^{15}
σ_x, σ_y (μm)	260, 16	255, 23	320, 16	320, 50
σ'_x, σ'_y (μrad)	23, 3.9	31, 9	34, 6	23, 7
Brightness ($K = 1$, $n = 1$)[a]				
[(photons/s)/mm^2 · mrad^2 · (0.1%BW)]	2.3×10^{19}	9.9×10^{18}	1.3×10^{19}	5.9×10^{18}
Total power ($K = 1$, all n, all θ) (W)	83	126	476	350
Other undulator periods (cm)	3.65, 8.00, 10.0	8.0, 12.5	6.8, 18.3	2.70, 5.50, 12.8
Wiggler Radiation:				
Wiggler period (typical) (cm)	16.0	14.0	6.1	8.5
Number of periods	19	30	30	28
Magnetic field (maximum) (T)	2.1	1.5	1.9	1.0
K (maximum)	32	19.6	12	7.9
Critical photon energy (keV)	5.1	4.0	11.4 keV	33
Critical photon wavelength	0.24 nm	0.31 nm	0.11 nm	0.38 Å
Total power (max. K) (kW)	13	7.2	9.3	7.4

Table 2.4. Properties of forms of Synchrotron Radiation (Atwood,1999).

Bending magnet radiation	Wiggler magnet radiation	Undulator magnet radiation
-Broad photon flux	-Higher photon energy	-Brighter radiation
-Good photon flux	-More photon flux	-Smaller spot size
-No heat load	-Expensive cooled optics	-Partial coherence
-Less expensive	-Expensive magnet structure	-Expensive magnet structure
-Easier access	-Less access	-Less access

2.7. Monochromator and Slits

The monochromator is used to select the X-ray energy incident on the sample. Typically the monochromator is stepped through the XAS scan range or it can be run continuously. The latter scanning mode is called quick-scanning of the monochromator. An X-ray monochromator usually consists of two parallel crystals (double-crystal monochromator) or a single crystal with a slot cut nearly through it (channel-cut monochromator). Typical monochromator crystals are made of silicon or germanium and are cut and polished such that a particular atomic plane of the crystal, described by the (*hkl*) indices, is parallel to the surface of the crystal. Common monochromator crystals are Si (111), Si(311), and Ge(111). The energy of X-rays diffracted by the crystal is controlled by rotating the crystals in the white beam. A simplified schematic of a monochromator is shown in Fig.2.21. Only the X-rays with energies that satisfy Bragg's Law are diffracted by the crystal. Bragg's Law is:

$$n\lambda = 2d\sin(\theta) \tag{2.92.}$$

where d is the spacing of the atomic planes of the crystal parallel to its surface, θ is the angle of the crystal with respect to the impinging white beam, λ is the wavelength

of the diffracted X-ray, and n is an integer. The fundamental X-ray energy corresponds to n = 1,and X-rays of higher harmonic energies correspond to n > 1.

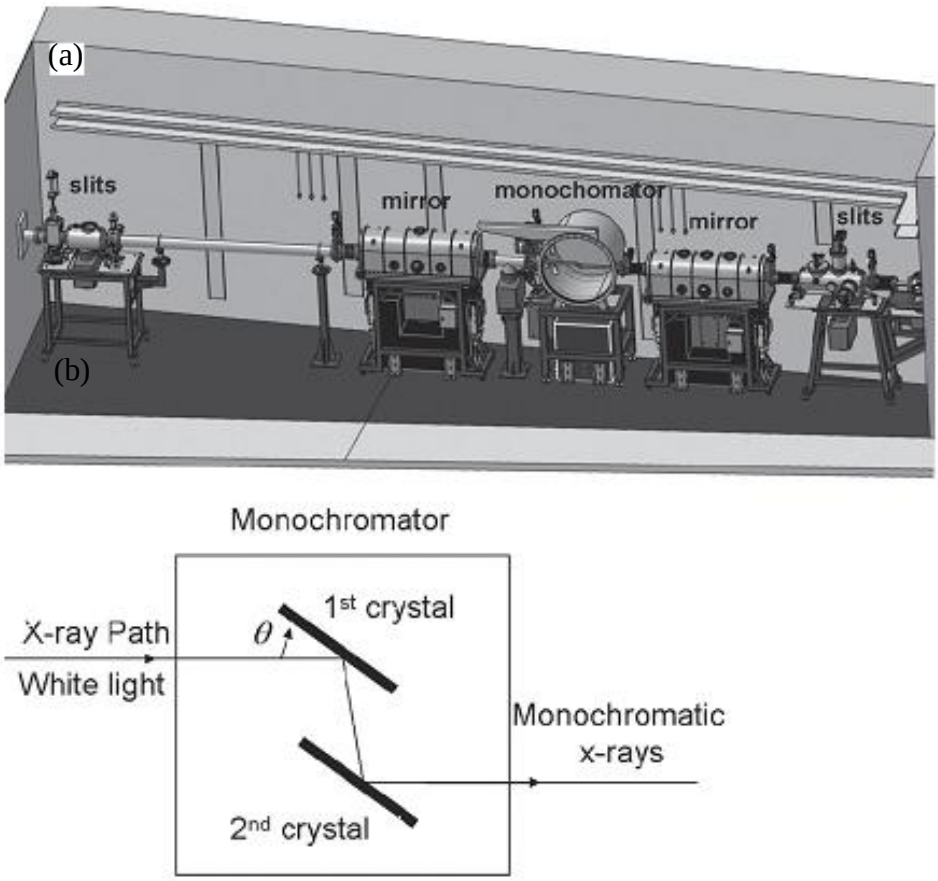

Figure. 2.20. (a) Drawing of the first optical enclosure of a beamline.X-rays enter the optical enclosure from the left. All EXAFS beamlines have a monochromator and slits.Some EXAFS beamlines have one or more mirrors.(b) Schematic of basic monochromator components (Kelly,2008).

Slits are used to define the X-ray beam profile and to block unwanted X-rays. Two common types are fixed and adjustable slits. Fixed slits have a pre-cut opening of fixed heights between 0.2 and 1.0 mm and a width of several centimeters. These slits can be moved into or out of the X-ray beam. Adjustable slits use metal plates that move independently to define each edge of the X-ray beam. Many beamlines have slits located upstream and downstream of the monochromator Fig. 2.20 (a) and before the I_0 detector. The monochromator slits may need to be adjusted at the start of an experiment or after a large (several kiloelectronvolts) change in X-

ray energy. Optimization is done by maximizing the X-ray intensity while changing the position of the slit opening. Vertical slits placed downstream or upstream of the monochromator can be used to increase the energy resolution of the X-ray incident on the sample at the expense of some loss in X-ray intensity (Kelly,2008).

2.8. Wurtzite ZnO Structure

The crystal structure of deposited ZnO thin films is generally hexagonal (wurtzite), and the film is usually polycrystalline. The structure of wurtzite ZnO is presented in Figure 2.21. The Zn atoms are tetrahedrally coordinated to four O atoms, where the Zn *d* electrons hybridize with O *p* electrons.

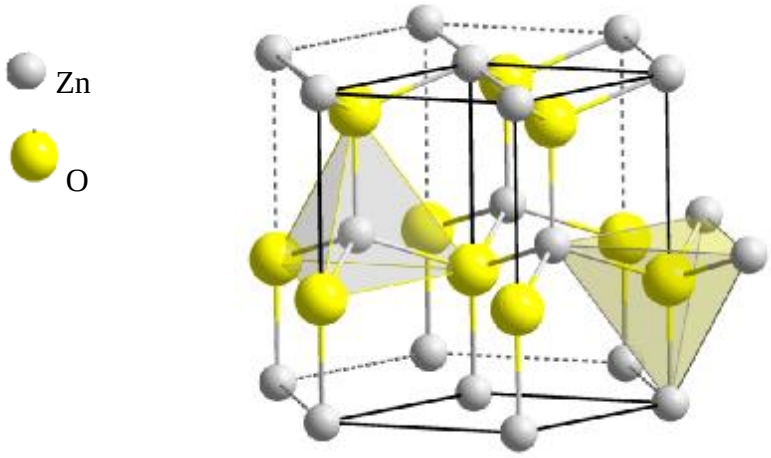

Figure 2.21. The structure of wurtzite ZnO

The lattice constants of wurtzite ZnO at room temperature is a = 3.250 Å and c = 5.206 Å. Also, it can be seen properties of wurtzite ZnO in table 2.5. Zinc Oxide (ZnO) is a promising wide bandgap semiconductor for applications in UV light emitting devices and sensors. For several years ZnO research has focused intensely on optimization of bulk and epitaxial growth, p-type doping, and production of high quality metal contacts.

Table 2.5. A few properties of wurtzite ZnO

Lattice Parameters at 300K	**Value**
a_0	0.32495 nm
c_0	0.52069 nm
a_0/ c_0	1.602
u	0.345
Density	5.606 g/cm^3
Stable phase	Wurtzite
Melting point	1975 C^o
Static dielectric constant	8.656
Energy gap	3.4 eV (direct)
Exciton binding energy	60 meV
Electron effective mass	0.24

More recently these efforts have expanded to include synthesis, properties, and deviceintegration of ZnO nanostructures. A variety of such low-dimensional structures (e.g., nanocrystals, nanowires,nanohelixes, nanotubes) have been demonstrated exhibiting greater purity and better crystal quality than bulk crystals and epilayers, as low defect concentrations are statistically favored in these nanoscale systems. These nanostructures present potential for important applications particularly inbiosensing devices and other nanoscale transducers. A challenging problem facing this area however involves the controlled assembly and integration of these nanoscale objects into anisotropicand highly functional systems of complex architecture. Zinc Oxide (ZnO) has caused agreat deal of interest in finding the capabilities this material have. ZnO is aunique material that demonstrates semiconducting, piezoelectric, and doped pyroelectric material. With Zinc Oxide becoming a favorable semiconductor with its wide direct bandgap of 3.3ev there has been much interest in optoelectronics applications to use this material as a UV laser.

Zinc Oxide is a strong candidate for short-wavelength optical devices such as laser emitting diodes or laser diodes. Zinc Oxide in the usage of thin films has shown very strong spontaneousand stimulating emissions by excitons at room temperature. This versatile material is also being used or considered for antireflections coatings, transparent electrodes in the solar cells, gas sensors,varistors, surface acoustic wave devices, electro and photoluminescent devices and is considering promising for phosphor for low-voltage luminescence in flat panel displays. Howevert here is no clear understanding of defectrelated luminescence phenomena in ZnO. Zinc Oxide nanoparticles are strong UV absorbers and can be used as a protective pigment in paints and coating applications. They also show strong photocatalytic and biocidal activity. Zinc oxide (ZnO) has been shown to exhibit the large direct band gap (3.37 eV) and exciton binding energy (60 meV) as well as the excellent chemical and thermal stability, properties that may lead to the important applications of this material in the ultraviolet devices, catalysis, piezoelectrics, and gas sensors. Recently, the prediction by Dietl and Sato of room temperature ferromagnetism in doped ZnO, the diluted magnetic semiconductors (DMS), has generated considerable research activity in both theory and experiment .So far, ZnO based DMS still attracts intensive researches because of its applications in spin valves and spin-based light-emittingdiodes, including Mn doped ZnO, Fe doped ZnO, Cu ZnO and Co doped ZnO. TM doped ZnO is illustrated in figure 2.22.

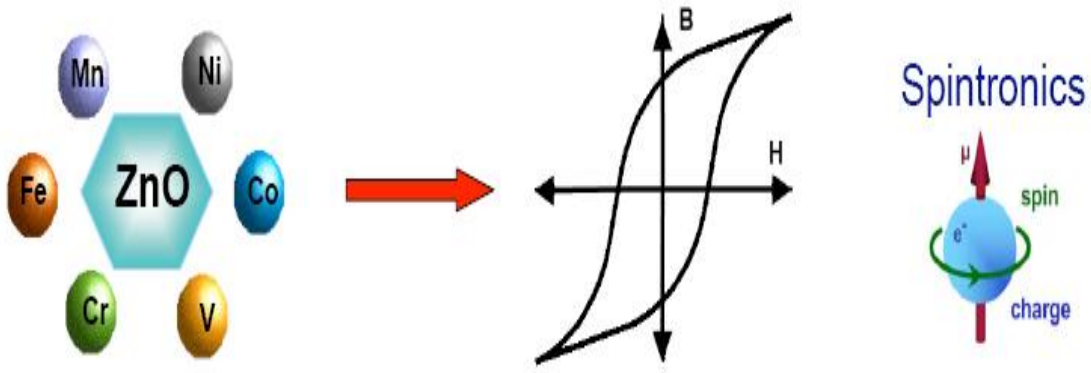

Figure 2.22. Doping ZnO with some transmission metals TM

3. MATERIAL AND METHOD

3.1. Powder Synthesis

Nanocrystalline zinc oxide particles doped with Cobalt ($Zn_{1-x}Co_xO$) contents between with x=0 and x=0.50 were produced by CVS method. The experimental setup is illustrated in Fig. 3.1. Appropriate amounts of anhydrous solid zinc acetate, $Zn(OAc)_2$ (Sigma Aldrich, 99.9 % purity) and cobalt acetate, $Co(OAc)_2$ (Sigma Aldrich, 99.9 % purity) powders of nominal Co content x are mixed thoroughly in a mortar inside a glove box and then transfered under inert conditions to the laser flash evaporator. The radiation (50 W) of a CO_2 laser (Coherent GEM 100 W) is used to evaporate the precursor mixture (Winterer 2007). It used $Zn(CH_3CO_2)_2$ as a Zinc precursor and $Co(CH_3CO_2)_2$ as a Cobalt precursor. The precursors vapors are transported into the hot wall reactor using helium (1020 sccm) as carrier gas. The reactor consists of two sequential furnaces, where the precursors react with oxygen (1000 sccm) and form oxide particles. The hot wall temperature was 1100°C and the total pressure 20 mbar. The particles are separated from the gas flow by thermophoresis in a particle collector. Atomic absorption spectroscopy (AAS) has been used to determine the actual cobalt content (x_a) in the as-synthesized particles. The measurement was carried out using Thermo Scientific Atomic Absorption Spectrometer M Series.

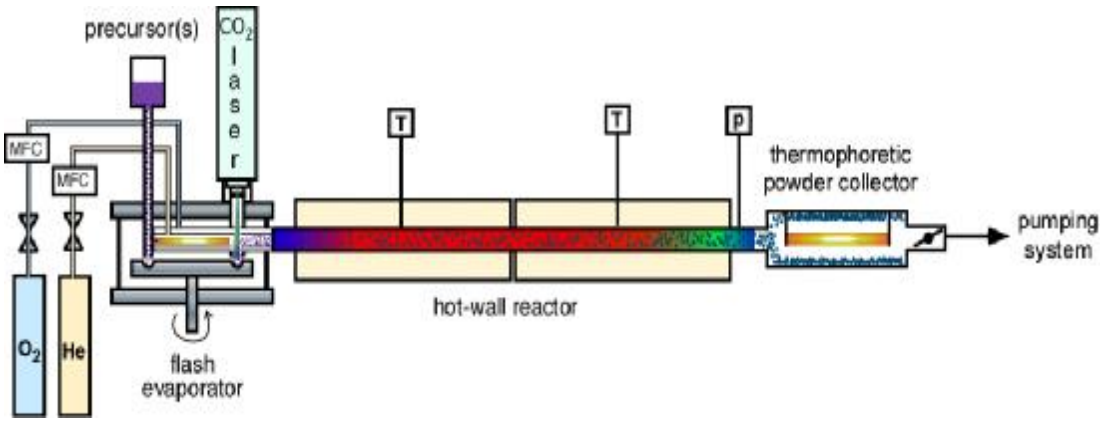

Figure 3.1. CVS reactor for the preparation of Co doped ZnO with laser flash evaporator, hot wall reactor and thermophoretic powder collector as modules.

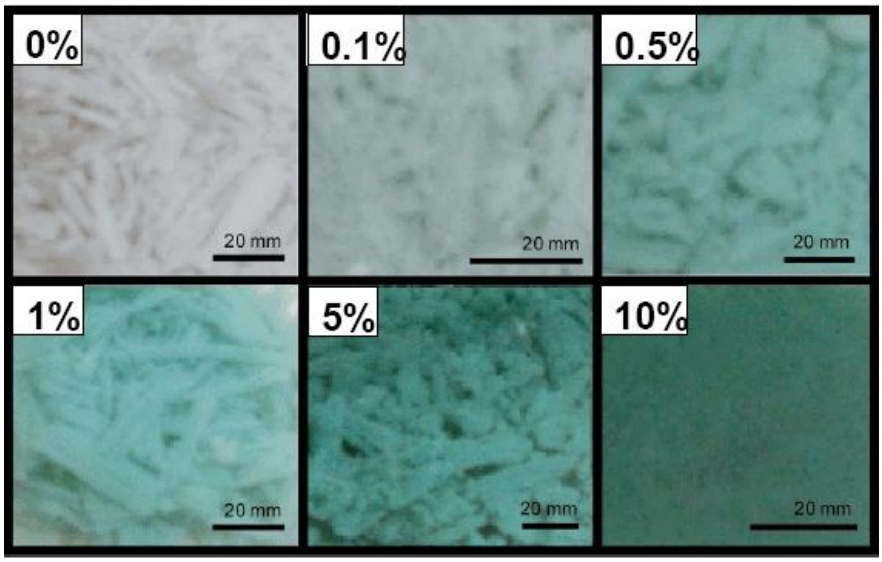

Figure 3.2. The change in the color of ZnO powders with addition of Co

Also, Figure 3.2 shows the change in the color of ZnO powders with addition of Co concentration x=0.10 as a synthesized powders.

3.2. Structural Characterization

3.2.1. X-Ray Diffraction (XRD)

In the present work, crystal structure and phase composition of the as-synthesized samples are determined by X-ray diffraction (XRD) using a PANalytical X-ray diffractometer (X'Pert PRO) with Ni-filtered Cu-K_α (1.5406 Å) radiation produced at 40 kV and 40 mA. The data, recorded over the $2q$ range from 20 to 120° with a step size of 0.03° and a sampling time of 200 s/step are collected using a X'Celerator detector. Detailed structural analyses are performed by Rietveld refinement of the x-ray data using the MAUD program (Lutterrotti,1990). Results reported by Kihara et al. for ZnO (Kihara 1985), and data reported by Liu et al. and Wyckoff, respectively for CoO and Co_3O_4 (Liu 1990 and Wyckoff 1963) are used as initial structural parameters for the refinements.

X-ray diffraction (XRD) is a versatile, non-destructive technique that reveals detailed information about the chemical composition and crystallographic structure of natural and manufactured materials and finding the crystal structure of an unknown material.

About 95% of all solid materials can be described as crystalline. The x-ray diffraction pattern of a pure substance is, therefore, like a fingerprint of the substance. The powder diffraction method is thus ideally suited for characterization and identification of polycrystalline phases. In order to better convey an understanding of the fundamental principles and buzz words of x-ray diffraction instruments, let us quickly look at the theory behind these systems. Solid matter can be described as :

Amorphous : The atoms are arranged in a random way similar to the disorder we find in a liquid. Glasses are amorphous materials.

Crystalline : The atoms are arranged in a regular pattern, and there is a smallest volume element that by repetition in three dimensions describes the crystal. E.g. we can describe a brick wall by the shape and orientation of a single brick. This smallest volume element is called a unit cell. The dimensions of the unit cell is

described by three axes : a, b, c and the angles between them alpha, beta, gamma. (About 95% of all solids can be described as crystalline.)

An electron in an alternating electromagnetic field will oscillate with the same frequency as the field. When an x-ray beam hits an atom, the electrons around the atom start to oscillate with the same frequency as the incoming beam. In almost all directions we will have destructive interference, that is, the combining waves are out of phase and there is no resultant energy leaving the solid sample. However the atoms in a crystal are arranged in a regular pattern, and in a very few directions we will have constructive interference. The waves will be in phase and there will be well defined x-ray beams leaving the sample at various directions. Hence, a diffracted beam may be described as a beam composed of a large number of scattered rays mutually reinforcing one another. This model is complex to handle mathematically, and in day to day work we talk about x-ray reflections from a series of parallel planes inside the crystal. The orientation and interplanar spacings of these planes are defined by the three integers *h,k,l* called indices. A given set of planes with indices *h,k,l* cut the a-axis of the unit cell in h sections, the b axis in k sections and the c axis in l sections. A zero indicates that the planes are parallel to the corresponding axis. E.g. the 2, 2, 0 planes cut the a and the b– axes in half, but are parallel to the c– axis. A few planes are illustrated in Figure 3.3.

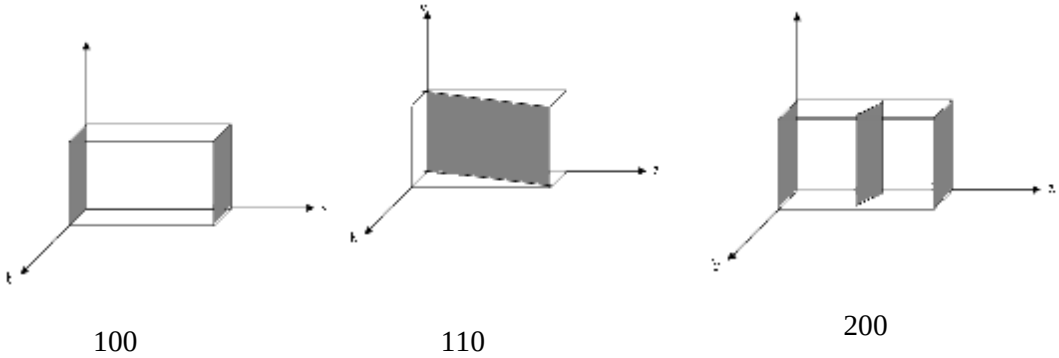

Figure 3.3. Examples of Miller indices notation for crystal planes (http://epswww.unm.edu/xrd/xrdbasics.pdf)

If we use the three dimensional diffraction grating as a mathematical model, the three indices *h, k, l* become the order of diffraction along the unit cell axes a, b and c respectively.

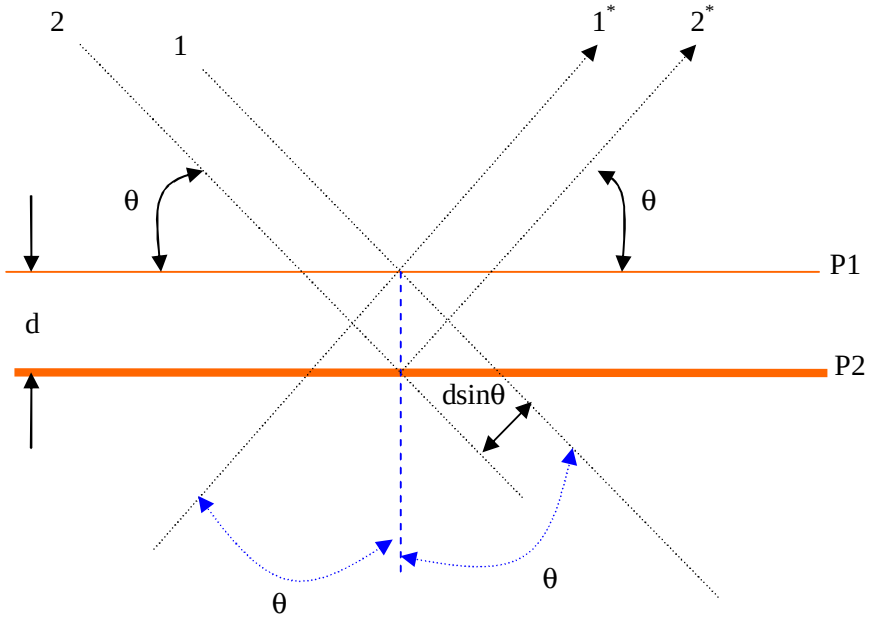

Figure 3.4. Diffraction of x-rays from parallel planes (http://epswww.unm.edu/xrd/)

Let us consider an x-ray beam incident on a pair of parallel planes P1 and P2, separated by an interplanar spacing d which is illustrated in Figure 3.4.

The two parallel incident rays 1 and 2 make an angle (θ) with these planes. A reflected beam of maximum intensity will result if the waves represented by 1' and 2' are in phase. The difference in path length between 1 to 1' and 2 to 2' must then be an integral number of wavelengths, (λ). We can express this relationship mathematically in Bragg's law.

$$n\,l = 2d\sin\theta \qquad (3.1.)$$

where *n* is taken as unity, The process of reflection is described here in terms of incident and reflected (or diffracted) rays, each making an angle θ with a fixed crystal plane. Reflections occurs from planes set at angle θ with respect to the incident beam and generates a reflected beam at an angle 2θ from the incident beam.

The possible *d*-spacing defined by the indices *h, k, l* are determined by the shape of the unit cell. Rewriting Bragg's law we get :

$$\sin\theta = \frac{l}{2d} \tag{3.2.}$$

The parameter d_{hkl} depends on the crystalline structure and can be calculated using:

$$d_{hkl} = \frac{a_o}{\sqrt{h^2 + k^2 + l^2}} \tag{3.3.}$$

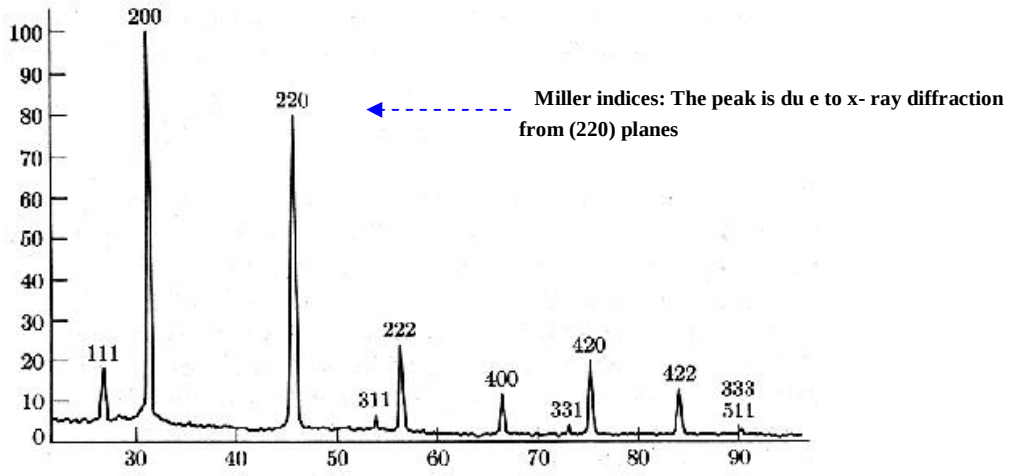

Figure 3.5. XRD Pattern of NaCl powder (www.physics.pdx.edu/~pmoeck/phy381/Topic5a-XRD.pdf)

Therefore the possible 2θ values where we can have reflections are determined by the unit cell dimensions. However, the intensities of the reflections are determined by the distribution of the electrons in the unit cell. The highest electron density are found around atoms. Therefore, the intensities depend on what kind of atoms we have and where in the unit cell they are located. Planes going through areas

with high electron density will reflect strongly, planes with low electron density will give weak intensities.(http://epswww.unm.edu/xrd/xrdbasics.pdf)

Also, the crystalline size *D* can be evaluated from the full-width-half-maximum (FWHM) value of the reflections of the films, using the Scherer equation:

$$D = \frac{0.9\,l}{w\cos q} \qquad (3.4.)$$

where ω is the broadening of the diffraction line measured at half its maximum intensity in radians and λ is wavelength of the X-rays (often the Cu K_α line at 0.15406 nm).

Significance of peak shape in XRD is peak position, width and intensity important for particle or grain size and residual strain used to get information about structure. Full Width at Half Maximum (FWHM) is illustrated in figure3.6 and effect of Lattice Strain on Diffraction Peak Position and Width and can also be fit with Gaussian,Lorentzian , Gaussian-Lorentzian etc.

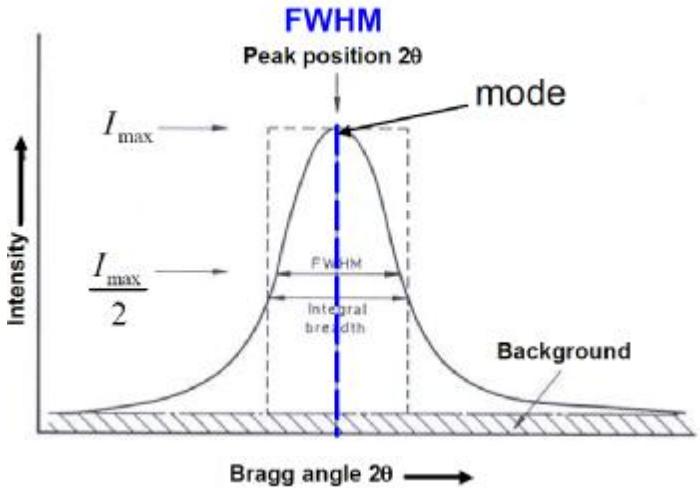

Figure 3.6. Peak Width-Full Width at Half Maximum (www.physics.pdx.edu/~pmoeck/phy381/Topic5a-XRD.pdf)

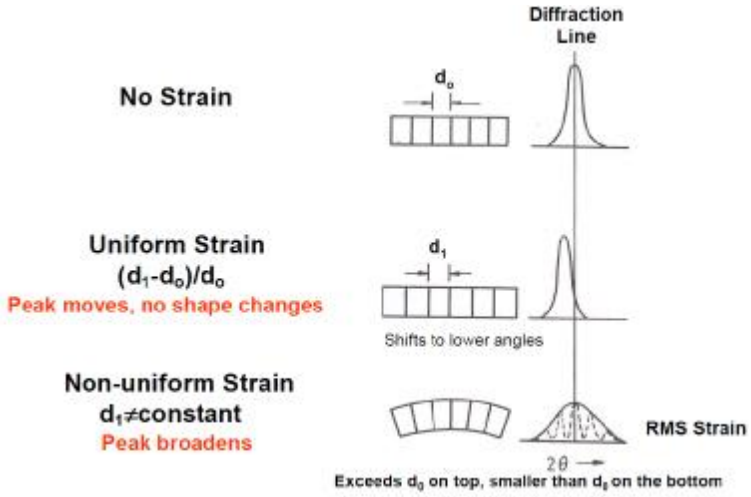

Figure 3.7. Effect of Lattice Strain on Diffraction Peak Position and Width (www.physics.pdx.edu/~pmoeck/phy381/Topic5a-XRD.pdf)

The crystal parameters from XRD data are extracted by Rietveld refinement using the Maud program. Rietveld refinement is a standard procedure to get these parameters.

3.2.2. Rietveld Refinement

Rietveld refinement is a technique devised by Hugo Rietveld for use in the characterisation of crystalline materials. The neutron and x-ray diffraction of powder samples results in a pattern characterised by reflexes (peaks) in intensity at certain positions. The height, width and position of these reflections can be used to determine many aspects of the materials structure.The method was first reported for the diffraction of monochromatic neutrons where the reflection-position is reported in terms of the Bragg angle 2θ. This terminology will be used here although the technique is equally applicable to alternative scales such as x-ray energy or neutron time-of-flight. The only wavelength and technique independent scale is in reciprocal space units or momentum transfer *Q*, which is historically rarely used in powder diffraction but very common in all other diffraction and optics techniques.

The momentum transfer plays an important role in the evaluation of neutron, x-ray and electron diffraction for the investigation of condensed matter. Bragg diffraction occurs on the atomic crystal lattice, conserves the wave energy and thus is called elastic scattering, where the wave numbers final and incident particles, k_f and k_i, respectively, are equal and just the direction changes by a reciprocal lattice vector $G = Q = k_f - k_i$ with the relation to the lattice spacing $G = 2\pi / d$. As momentum is conserved, the transfer of momentum occurs to crystal momentum.

The presentation in Q space is generic and does not depend on the type of radiation and wavelength used but only on the sample system, which allows to compare results obtained from the many different methods. Some established communities such as powder diffraction employ the diffraction angle 2θ as the independent variable, which worked fine in the early years when only a few characteristic wavelengths such as Cu-Kα were available. The relationship to Q space is(Wikipedia):

$$Q = \frac{4p \sin q}{l} \tag{3.5.}$$

3.2.3. Transmission Electron Microscopy (TEM)

Transmission electron microscopy (TEM) is a microscopy technique whereby a beam of electrons is transmitted through an ultra thin specimen, interacting with the specimen as it passes through. An image is formed from the interaction of the electrons transmitted through the specimen; the image is magnified and focused onto an imaging device, such as a fluorescent screen, on a layer of photographic film, or to be detected by a sensor such as a CCD camera. You can see objects to the order of a few angstrom (10^{-10} m). For example, you can study small details in the cell or different materials down to near atomic levels. The possibility for high magnifications has made the TEM a valuable tool in both medical, biological and materials research.

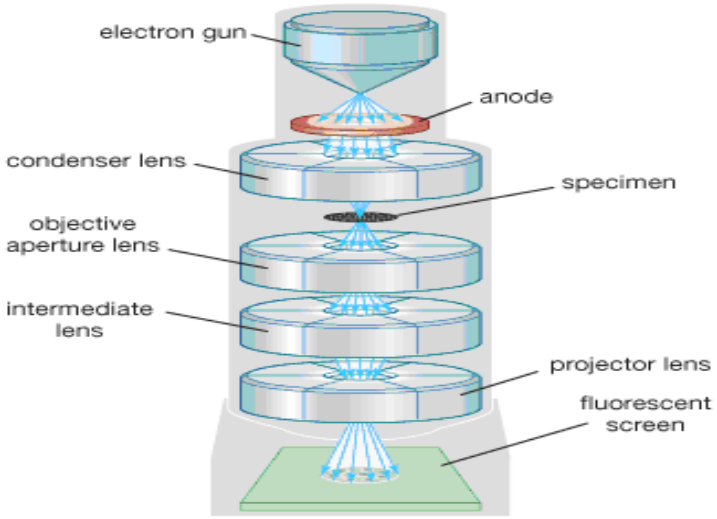

Figure 3.8. Transmission electron microscope.(Encyclopaedia Britannica)

3.3. Method

In order to investigate local structure of the Co in Co doped ZnO nanoparticles X-ray absorption spectra are measured at the Co *K*- edge and Zn *K*-edge using beam line 12.BM.B at the Advanced Photon Source (APS) at Argonne National Laboratory in Chicago-USA. The beam line 12.BM.B is a bending magnet beamline dedicated to spectroscopy scattering experiments and has energy range 7.5-28 keV. The absorption of the samples is optimized by diluting appropriate amounts of sample homogeneously in starch powder and pressing a pellet uniaxially. Transmission and fluorescence spectra are collected at ambient temperature. It can be seen experimental setup at beamline 12.BM.B in figure 3.9. The spectra of commercial CoO and Co_3O_4 powders (Sigma Aldrich) are also recorded. The EXAFS data are also analyzed using ARTEMIS, RMC and FEFF8 programme. ARTEMIS is a program for analyzing EXAFS data and uses chi(k) as it‘s input. FEFF8 is used as external program to calculate basic spectra for XANES fitting.

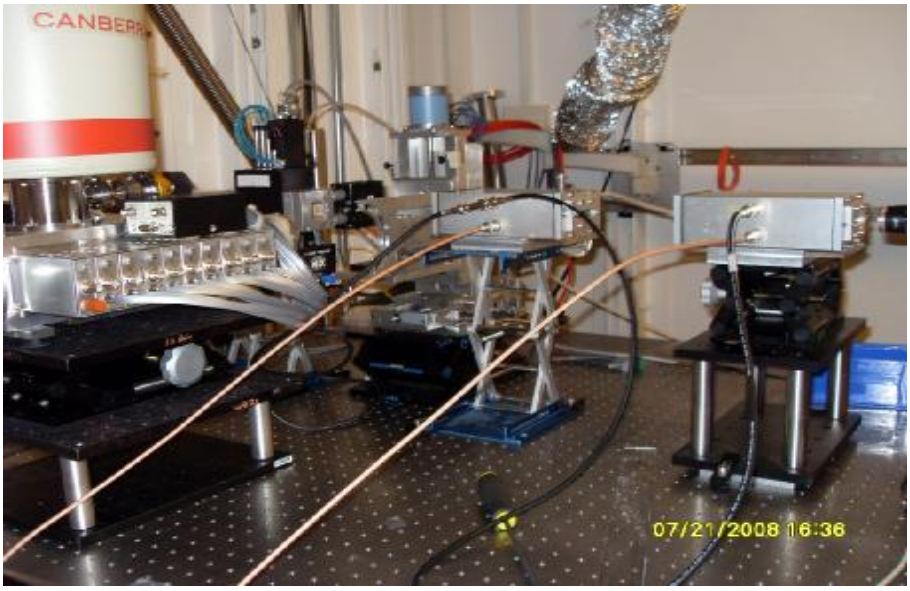

Figure 3.9. Experimental setup beamline 12.BM.B at the Advanced Photon Source

3.4. Argonne National Laboratory (ANL)

Argonne National Laboratory is one of the U.S. Department of Energy's largest research centers. It is also the America's first national laboratory, chartered in 1946.

Recognized for its excellence in connecting basic research to innovative technology, Argonne is a direct descendant of the University of Chicago's Metallurgical Laboratory, part of the World War Two Manhattan Project. It was at the Met Lab where, on Dec. 2, 1942, Enrico Fermi and his band of about 50 colleagues created the world's first controlled nuclear chain reaction in a racquets court at the University of Chicago. Fermi believed that a collaborative approach to science would deepen understanding and result in greater value. Over the years, Argonne has embraced Fermi's beliefs, creating one of the world's broadest scientific institutes, bringing together many areas of science, engineering and technology.

Today, the laboratory has about 2,800 employees, including about 1,000 scientists and engineers, of whom about 750 hold doctorate degrees. Argonne's annual operating budget of about $530 million supports upwards of 200 research

projects, ranging from studies of the atomic nucleus to global climate change research. Since 1990, Argonne has worked with more than 600 companies and numerous federal agencies and other organizations.

Argonne occupies 1,500 wooded acres in DuPage County, Ill. The site is surrounded by forest preserve about 25 miles southwest of Chicago's Loop. The site also houses the U.S. Department of Energy's Chicago Operations Office

3.5. Beamlines

At a synchrotron facility, electrons are usually accelerated by a synchrotron, and then injected into a storage ring, in which they circulate, producing synchrotron radiation, but without gaining further energy. The radiation is projected at a tangent to the electron storage ring and captured by beamlines. These beamlines may originate at bending magnets, which mark the corners of the storage ring; or insertion devices, which are located in the straight sections of the storage ring. The spectrum and energy of X-rays differ between the two types. The beamline includes x-ray optical devices which control the bandwidth, photon flux, beam dimensions, focus, and collimation of the rays. The optical devices include slits, attenuators, crystal monochromators, and mirrors. The mirrors may be bent into curves or toroidal shapes to focus the beam. A high photon flux in a small area is the most common requirement of a beamline. The design of the beamline will vary with the application. At the end of the beamline is the experimental end station, where samples are placed in the line of the radiation, and detectors are positioned to measure the resulting diffraction, scattering or secondary radiation.

3.6. Overview of the APS

The Advanced Photon Source (APS) at the U.S. Department of Energy’s Argonne National Laboratory provides this nation’s (in fact, this hemisphere’s) most brilliant x-ray beams for research in almost all scientific disciplines.

These x-rays allow scientists to pursue new knowledge about the structure and function of materials in the center of the Earth and in outer space, and all points in between. The knowledge gained from this research can impact the evolution of combustion engines and microcircuits, aid in the development of new pharmaceuticals, and pioneer nanotechnologies whose scale is measured in billionths of a meter, to name just a few examples. These studies promise to have far-reaching impact on our technology, economy, health, and our fundamental knowledge of the materials that make up our world. The APS electron accelerator and storage system are the first critical steps in producing the high-energy x-rays that are used for frontier research.



Figure 3.10. Aerial photo of the Advanced Photon Source facility (APS) (www.anl.gov)

3.7. How APS works

Electrons are produced by a cathode that is heated to about 1,100°C (2,000°F). The electrons are accelerated to 99.999% of the speed of light in a linear accelerator. From the linear accelerator, the electrons are injected into the booster synchrotron. Here, the electrons are sent around an oval racetrack of electromagnets, providing further acceleration. Within one-half second, the electrons reach 99.999999% of the speed of light. Upon reaching this speed, the electrons are injected into the storage ring, a 1,104 meter (3622 ft) circumference ring of more than 1,000 electromagnets.

Once in the storage ring, the electrons produce x-ray beams that are available for use in experimentation. Around the ring are 40 straight sections. One of these sections is used to inject electrons into the ring, and four are dedicated to replenishing the electron energy lost though x-ray emission by using 16 radio-frequency accelerating cavities. The remaining 35 straight sections can be equipped with insertion devices. Insertion devices, arrays of north-south permanent magnets usually called "undulators," cause the electrons to oscillate and emit light in the invisible part of the electromagnetic spectrum. Due to the relativistic velocities of the electrons, that light is Lorentz contracted into the x-ray band of the electromagnetic spectrum.

The Experiment Hall surrounds the storage ring and is divided into 35 sectors, each of which has access to x-ray beamlines, one at an insertion device, and the other at a bending magnet. Each sector also corresponds to a lab/office module offering immediate access to the beamline.

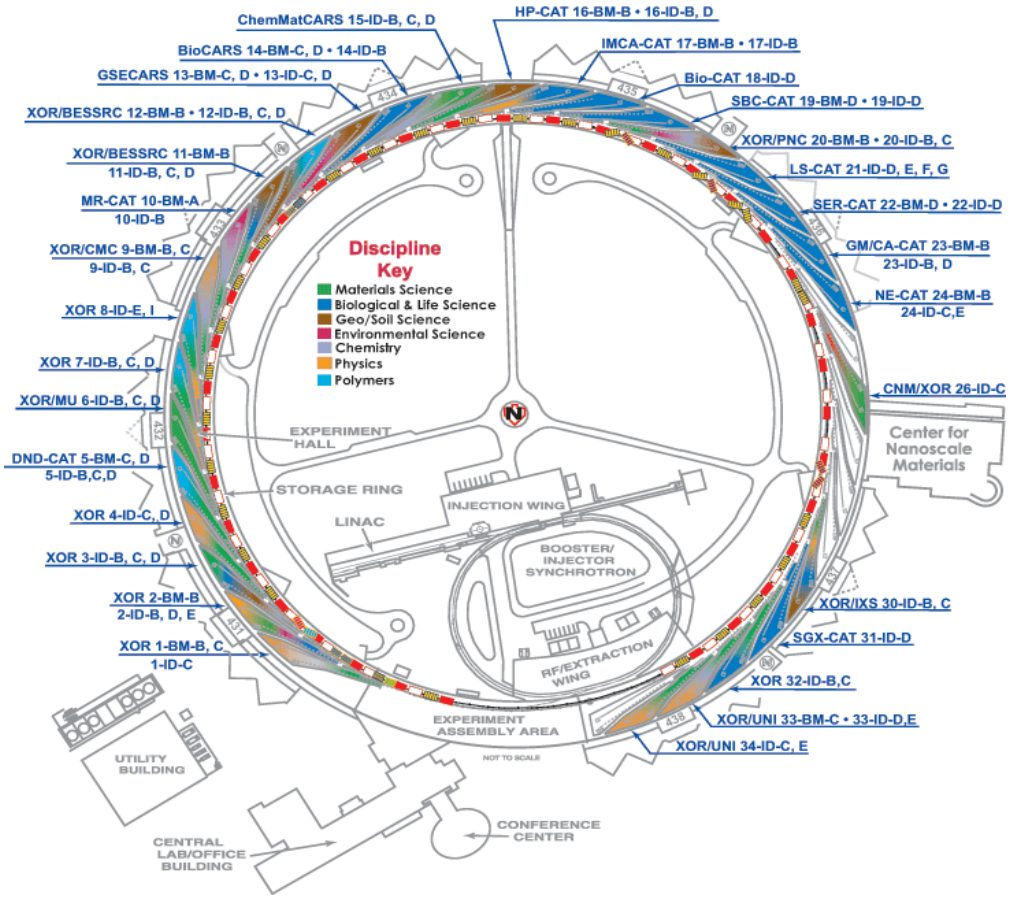

Figure 3.11. Beamlines map of APS (www.anl.gov)

There are 5 main components that make up the APS technical facility: the linear accelerator, the booster synchrotron, the electron storage ring, insertion devices, and the experiment hall.

3.7. 1. Linear Accelerator

Producing brilliant x-ray beams at the APS begins with electrons emitted from a cathode heated to ~1100° C. The electrons are accelerated by high-voltage alternating electric fields in a linear accelerator (linac; photo below). Selective phasing of the electric field accelerates the electrons to 450 million volts (MeV). At

450 MeV, the electrons are relativistic: they are traveling at >99.999% of the speed of light, which is 299,792,458 meters/ second (186,000 miles/second).



Figure 3.12. Linear accelerator at APS (http://www.aps.anl.gov/)

3.7.2. Booster Synchrotron

Electrons are injected into the booster synchrotron (photo below), a racetrack-shaped ring of electromagnets, and accelerated from 450 MeV to 7 billion electron volts (7 GeV) in one-half second. (By comparison, the electron beam that lights a TV screen is only 25,000 electron volts.) The electrons are now traveling at >99.999999% of the speed of light. The accelerating force is supplied by electrical fields in four radio frequency (rf) cavities. In order to maintain the orbital path of the electrons, bending and focusing magnets increase the electron field strength in synchronization with the rf field.

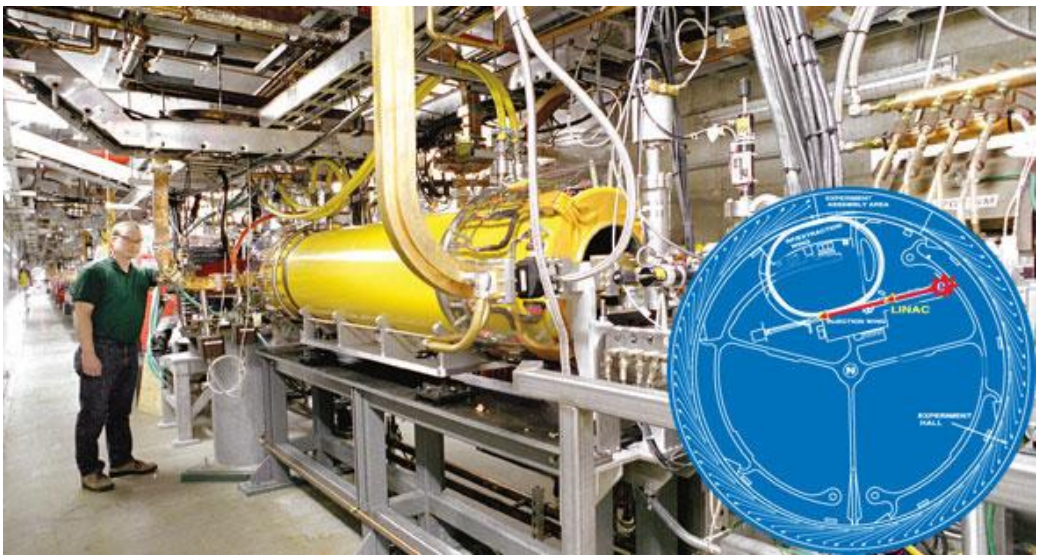

Figure 3.13. Booster synchrotron at APS (http://www.aps.anl.gov/)

3.7.3. The Electron Storage Ring

The 7-GeV electrons are injected into the 1104-m-circumference storage ring, a circle of more than 1,000 electromagnets and associated equipment, located in a concrete enclosure inside the experiment hall, which is large enough to encircle Chicago's U.S. Cellular Field. A powerful electromagnetic field focuses the electrons into a narrow beam that is bent on a circular path as it orbits within aluminum-alloy vacuum chambers running through the centers of the electromagnets.The sequencing, or lattice, of magnets in the APS storage ring (photo below) produces a beam of very small size and low angular divergence, qualities prized by users of synchrotron light sources. The lattice also results in 40 straight sections, or sectors, in the storage ring. Five sectors are used for beam injection and rf equipment. The remaining 35 are equipped with insertion devices (diagram at right), which are the sources of the brightest x radiation in the Western Hemisphere.

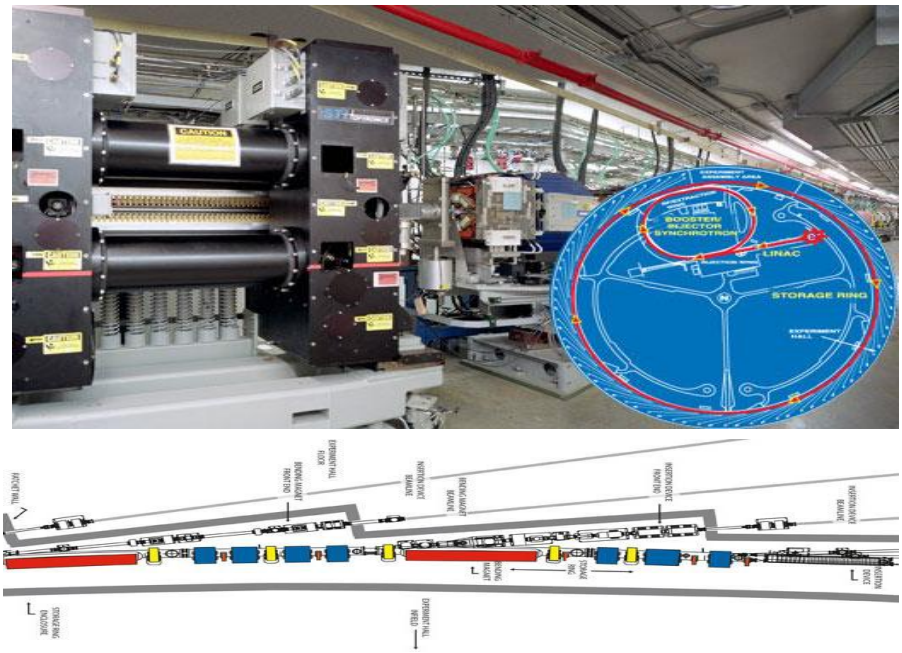

Figure 3.14. The electron storage ring at APS (http://www.aps.anl.gov/)

3.7.4. Insertion Devices and Brilliance

Synchrotron storage rings optimized for insertion devices (photo below) are called "third-generation" light sources. Some, like the Advanced Light Source in California and the SuperACO in France, provide radiation in the ultraviolet/soft x-ray part of the spectrum. The 7-GeV APS and its sister facilities, the 6-GeV European Synchrotron Radiation Facility in France, and the Super Photon Ring 8-GeV (SPring-8) in Japan, can produce a range of x-rays up to those of the hard (highly penetrating) variety because of higher machine energies.

Third-generation storage rings maximize those x-ray beam qualities, flux and brilliance, that are needed for frontier experimentation. Flux and brilliance are benchmarks of x-ray beam quality. Both are based on a measure of the number of photons per second in a narrow energy bandwidth and in a unit of solid angle in the horizontal and vertical directions. Flux is the number of photons per second passing through a defined area, and is the appropriate measure for experiments that use the entire, unfocused x-ray beam. Brilliance is a measure of the intensity and directionality of an x-ray beam. It determines the smallest spot onto which an x-ray

beam can be focused. View a chart comparing APS spectral brilliance to a variety of x-ray sources.



Figure 3.15. Undulator at APS (http://www.aps.anl.gov/)

3.7.5. Experiment Hall

The ratchet-shaped radiation-shielding wall between the APS storage ring and the experiment hall serves as a line of demarcation. Thirty-five "sectors" are marked on the experiment hall floor. Each of these sectors comprises at least two x-ray beamlines, one originating at a bending magnet in the storage ring lattice, the other at an insertion device. With all APS sectors equipped and operating, the APS, in effect, has 35 discrete laboratories under one roof.

The circular APS experiment hall is where scientists assemble their experimental apparatus and carry out research. The hall has been designed as an enclosed, 1104-m-circumference optical bench. The hall floor is made of 1-ft-thick poured concrete. Usual practice in poured concrete construction is the use of evenly spaced cuts in the slab to create isolated sections, which are free to move

independently, alleviating cracks. There are no cuts in the APS experiment hall floor, creating a solid and uniform slab, as shown in the photo below, which was taken before installation of experimental equipment.

A stable experiment hall floor is of great benefit to users of the APS, who must align their experimental equipment to submicron tolerances. Regular surveys of the floor show that it has moved at most by 6 mm in certain areas (less in others) and is now moving on the scale of 0.2 mm per year. That figure includes shrinkage, settlement, and all of the transitory effects experienced by concrete over time.



Figure 3.16**.** Experimental hall at APS

3.8. X-ray Absorption Spectroscopy

X-ray spectroscopy is one of the effective methods of the nondestructive analysis of the electronic structure, atomic concentration and chemical phase composition of materials. X-ray Absorption Spectroscopy (XAS) is a synchrotron-

based experimental technique which allows to obtain the details of structural environment around selected atoms in a sample. One of the most popular modifications of XAS is x-ray Absorption Fine-Structure method, or XAFS. In this experiment, the x-ray photons of tunable energies (wavelengths) get absorbed by the sample they irradiate if the energy of the photons is equal to or exceeds the ionization energy of selected atoms or ions. In the x-ray photon absorption, in accordance with Einstein's photoelectric effect, the photons knock the core-shell electrons out of the atoms and the resulting photo-electrons travel away from the absorbing atoms.

Near edge spectral dependencies of the x-ray absorption coefficient and spectral distributions of the intensity in the characteristic x-ray emission bands reflect the energy distribution of the density of empty electronic states of the conduction band (CB) and occupied electronic states of the valence band (VB), respectively. X-ray absorption and emission processes have a local character (associated with hole localization in the core shell) and selection rules for the transitions between the initial and the final state have been worked out. The selection rules for the dipole transitions are: $\Delta l = \pm 1, \Delta m = 0, \pm 1$, $\Delta j = 0, \pm 1$, $\Delta L = 0, \pm 1$, $\Delta J = 0, \pm 1$, $\Delta S = 0, \pm 1$ .All these rules are the so-called dipole selection rules. Thus the possibility to obtain the information about local and partial (allowed for certain angular momentum symmetry) density electronic states of the conduction and the valence band is appeared. Such unique information does not posses a single method.

X-rays interact with matter in several ways. These interactions all include some type of excitation of or scattering with, the matter involved. If an incident x-ray photon is of sufficient energy, the atom may absorb it. The absorption of the x-ray causes a photoelectron to be ejected from the atom in a process called photoionization, which is illustrated in Figure 3.17. This creates an excited state within the atom.

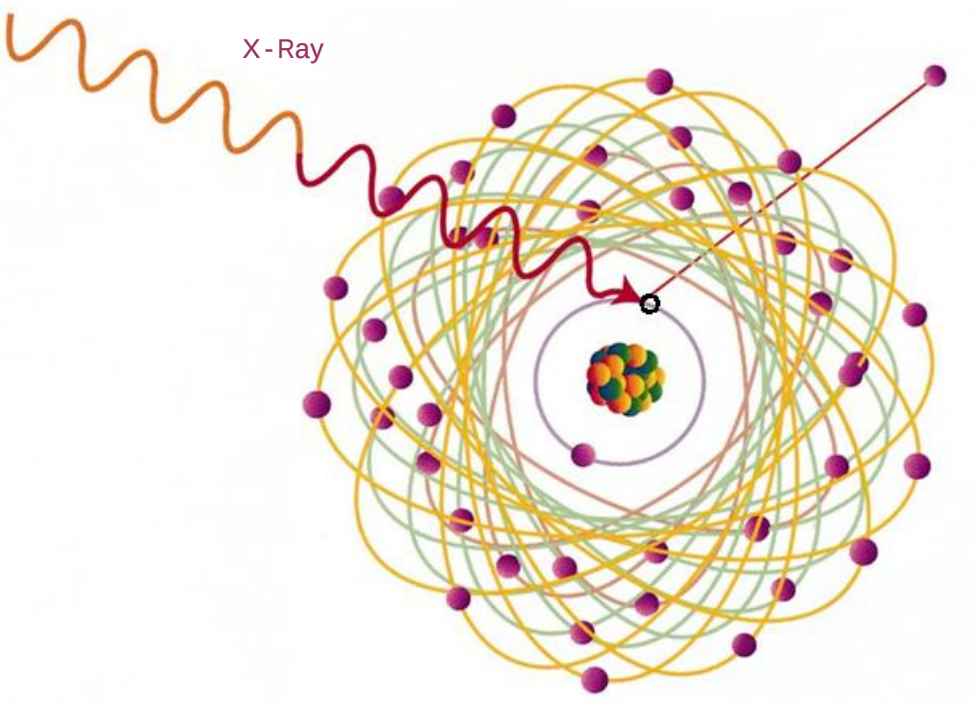

Figure 3.17. The photoionization process. An x-ray photon is absorbed and an electron ejected from the atom.In this case,the illustration shows the ejection of a 1s core electron(ww.p-ng.si/~arcon/images/fotoefekt.jpg).

The basic process of x-ray absorption is the excitation of electrons from deep core levels of a selected atom by the absorption of a photon. The phenomenon is schematized in Figure 3.17.

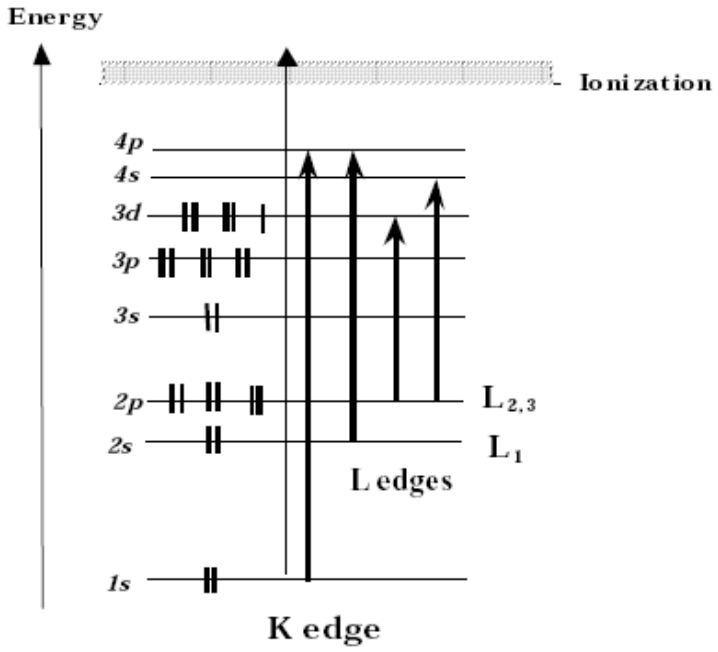

Figure 3.18. Scheme of the excitation of an electron by the absorption of a X-ray photon.(Koningsberger,1988)

Several processes can occur after the absorption of the photon and subsequent ejection of a photoelectron in order to return the atom to its ground state. An outer shell electron may fill the shell vacancy created through photoionization, which creates a fluorescent x-ray photon. Fluorescent yield is illustrated in Figure 3.19. The fluorescent photon that is emitted is at a lower energy than the absorbed photon and is characteristic of the absorbing element. As atomic number increases, the fluorescent yield, or the probability that an absorption event will create a fluorescent photon, increases (Teo, 1986). For example, the K-shell (*1s*) fluorescent yields for O (Z=8), Cl(Z=17), Fe(Z=26), Zn(Z=30), Cd(Z=48), and Pb(Z=82) are 0.0083, 0.097, 0.347 0.474, 0.843, and 0.967 respectively (Krause, 1979).

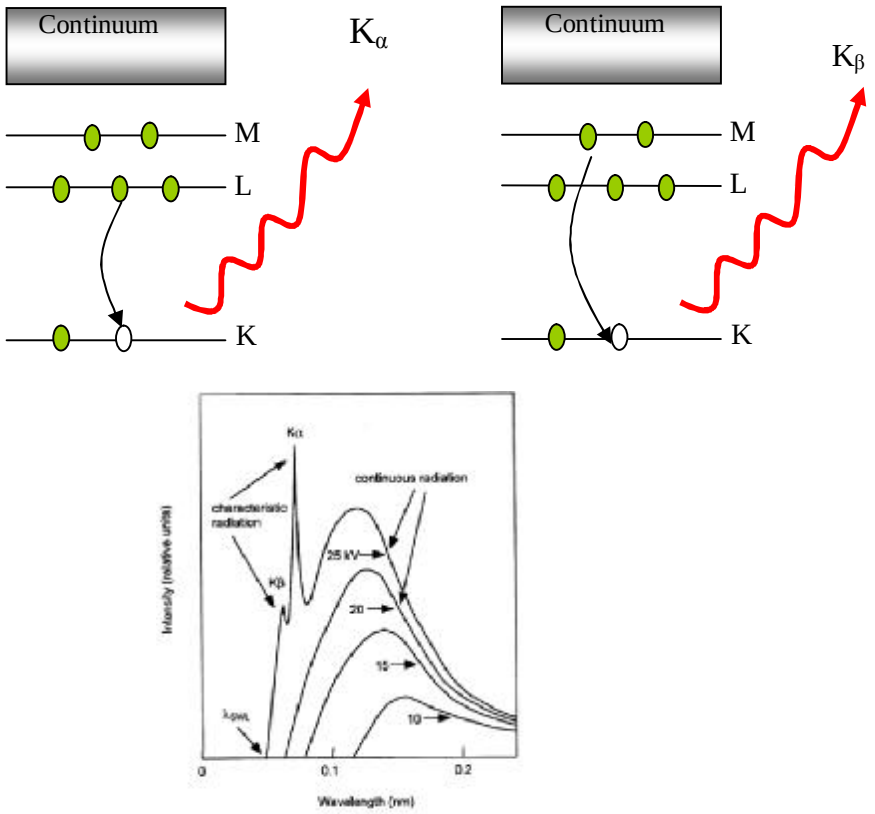

Figure 3.19. Fluorescent x-ray emission. One of the electrons in an outer shell fills the hole creating a photon. In this example the outer electron comes either from the L or M shell .In the former case the fluorescent radiation is referred to as the K_α line ,and in the latter K_β.

The other major process following an x-ray absorption event is the Auger effect. Auger yield is illustrated in Figure 3.20. In this case, the vacancy created by the photoelectron is filled by an electron dropping from a higher shell while the atom simultaneously ejects another electron. This additional electron is usually emitted from the same higher shell as the one that replaced the vacancy. This can be qualitatively thought of as an autoionization process, where the fluorescent photon created by the filling of the vacancy is energetic enough to ionize another electron from another shell of the same atom. However, the Auger effect is a one-step process where the atom readjusts to the initial vacancy rather than a two-step process. Finally, the photoionization of the atom can also create secondary electrons. These are created as the fluorescent x-ray or Auger electrons leave the atom and cause other

high shell electrons to be ejected. This can be thought of as a cascade effect, and can be produced in abundant quantities.

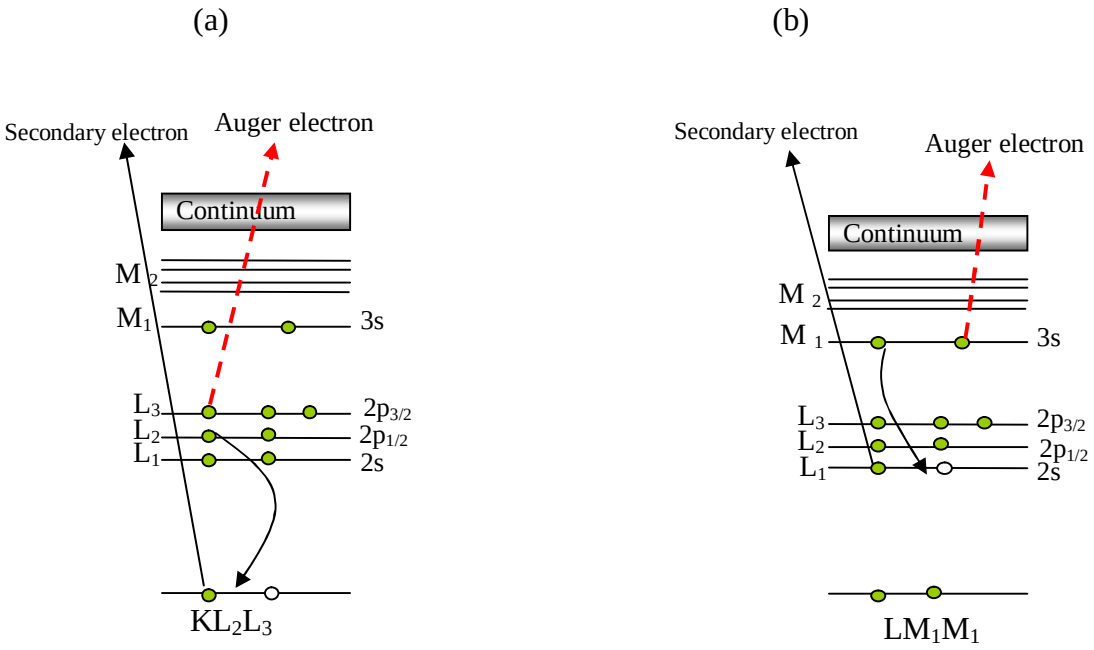

Figure 3.20. (a) and (b) Auger electron emission. The atom may also relax to its ground state energy by liberating an electron

X-rays also interact with matter through scattering processes. These are broken into two categories: coherent (elastic scattering) and incoherent (inelastic scattering). Coherent or Rayleigh scattering results from the interference between elastically scattered waves from individual atoms. In these cases, the photons are scattered by the atoms electrons that are bound tightly, and no ionization takes place. Since the scattering is elastic, there is no loss of energy, and thus the wavelength of the scattered radiation is the same. This is not true in general in a quantum mechanical description , where the incident x-ray photon has a momentum of $\hbar k$ and an energy of $\hbar\omega$. Energy may be transferred to the electron with the result that the scattered photon has a lower frequency relative to that of the incident one.The elastic scattering of x-rays is the main process that is exploited in investigations of the structure of materials , and in this case it mostly suffices to adopt a classical

approach .Of course momentum may be transferred even in an elastic scattering event , and this leads to the definition of the vector Q as

$$\hbar Q = \hbar k - \hbar k^{*} \qquad (3.6.)$$

Where ħk and ħk* are the initial and final momenta of the photon respectively. The vector Q is known as the wave vector transfer or scattering vector, and as we shall see it is natural variable to describe elastic scattering processes.Q is usually expressed in units of Å^{-1} (Nielsen, 2001)

In crystals, this coherent scattering from a periodic lattice produces what is known as Bragg diffraction.

Incoherent or Compton scattering takes place from interactions between the incident photons and loosely bound electrons. Part of the x-ray energy is transferred to the electron as the photon is scattered. Since energy is lost, the wavelength of the scattered x-rays will be shifted. For higher photon energies and heavier elements, the effects of scattering are several orders of magnitude less than that of absorption effects (Teo, 1986).

3.8.1. X-rays Absorption Coefficient

When discussing x-ray absorption, we are primarily concerned with the *absorption coefficient, $\mu(E)$* which gives the probability that x-rays will be absorbed according to Lambert-Beer's Law:

$$I(\hbar\omega) = I_o(\hbar\omega)e^{-\mu(E)t} \qquad (3.7.)$$

where I_o is the incident x-ray intensity on a sample, t is the sample thickness, and I is the intensity transmitted through the sample, as shown in Fig 3.21.

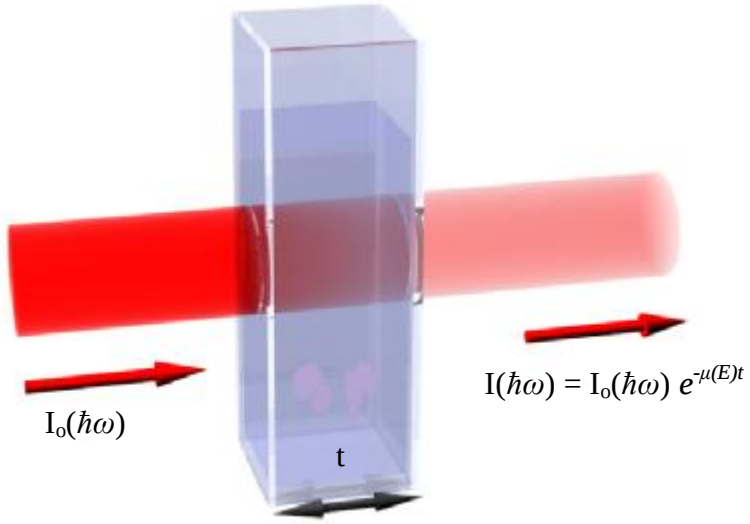

Figure 3.21. X- ray absorption measurements: An incident beam of monochromatic X- rays of intensity I_o passes through a sample of thickness t, and the transmitted beam has intensity I.

μ means also interactions of x-rays with atomic states. At most x-ray energies, the absorption coefficient μ is a smooth function of energy, with a value that depends on the sample density ρ, the atomic number Z, atomic mass A, and the x-ray energy E roughly as

$$\mu \approx \frac{rZ^4}{AE^3} \qquad (3.8.)$$

The strong dependence of μ on both Z and E is a fundamental property of x-rays. As the energy of the x-rays is increased, the absorption coefficient μ generally decreases gradually. This occurs until a critical energy is reached that where the coefficient increases abruptly by as much as an order of magnitude. Fig 3.22 shows the energy-dependence of μ for Xe.

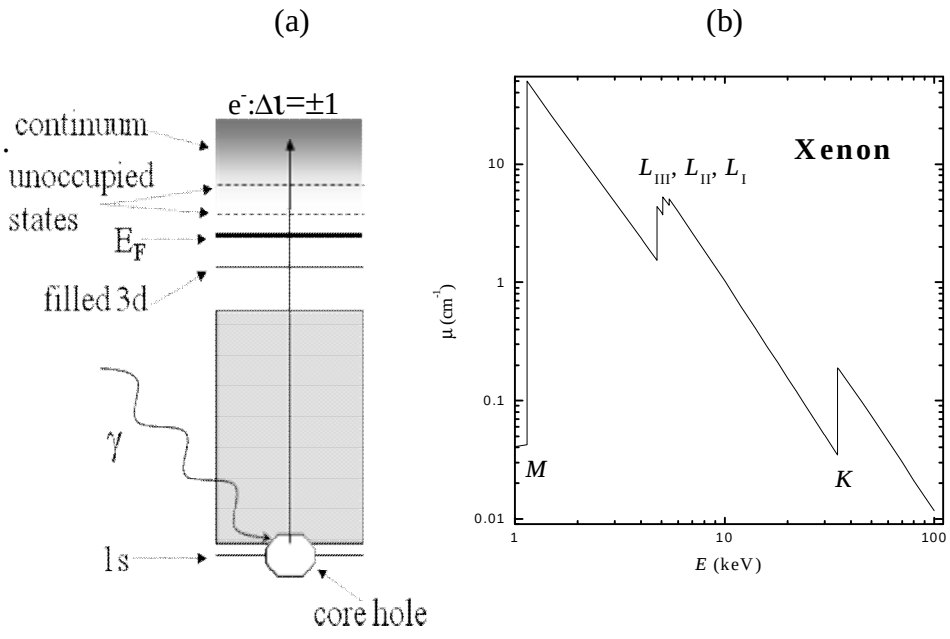

Figure 3.22. (a) X-ray absorption process by a core electron (b) The absorption cross-section μ Xenon element over the x-ray energy range of 1 to 100 keV. There are sharps which rise corresponding to the core-level binding energies of the atoms

When the incident x-ray has an energy equal to that of the binding energy of a core-level electron, there is a sharp rise in absorption edge corresponding to the promotion of this core level to the continuum. An illustration of x-ray absorption edges is given in Figure 3.23. This rapid change is due the x-ray photons reaching the energy at which an inner shell electron (*e.g.* the K shell (*1s*) or L shell (*2s* and *2p*)) can be ejected from the atom. The feature is called the absorption edge and is a unique characteristic of each element.

The absorption edge structure often consists of discrete absorption bands superimposed on the steeply rising continuum absorption edge.These discrete absorption bands are cau-sed by transitions of core electrons to discrete bound valence levels. The absorption edges that are of most interest are the K-edge (1s – 3p), followed by the three L-edges: L_1-edge (2s – 5p), L_2-edge ($2p_{1/2}$ – $5d_{3/2}$) and L_3-edge ($2p_{3/2}$ – $5d_{5/2}$) (J.Stöhr,2003). These edges are element specific and shifts to higher energies when the atomic number increases. Since the core levels depend on the element and its chemical environment, they also show chemical specificity. X-ray

absorption spectroscopy is therefore not only an element specific technique, but it is also sensitive to the immediate environment of the absorbing atom.

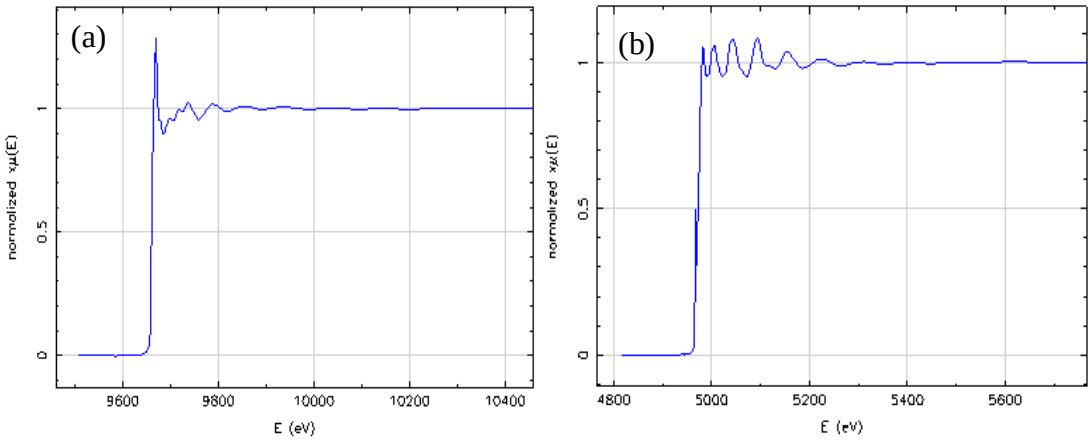

Figure 3.23. Sample x-ray absorption spectra for (a) Ti metal foil (b) Zn metal foil. (Data from our other experiment about Ti doped ZnO database).

3.8.2. The Regions of X-ray Absorption Spectroscopy (XAS)

X-ray absorption spectroscopy (XAS) uses features within and around the absorption edge to examine various coordination properties of the element of interest. Two major regions are discussed within the context of spectroscopy. Depending on photon energy, various physical processes lead to different features in the x-ray absorption spectrum, illustrated in the nickel K-edge spectrum of the magnet CsNiCr(CN)6 shown in Figure 3.24. It corresponds to the excitation of a Ni 1s electron. Such a spectrum is commonly (and roughly) divided in two regions, the X-ray Absorption Near Edge Structure (XANES) part and the Extended X-ray Absorption Fine structure (EXAFS) part. When the energy of the photon is less than the 1s binding energy Eo, electronic transitions to the first empty states occur. For a Ni^{2+} ion in a molecular complex ($3d^8$ configuration), the first empty states are the 3d molecular levels. The transitions to these states contribute to the band observed below the main edge in the region called pre-edge. Increasing the energy of the photons (but kept less than Eo), leads to a sharp increase of the absorption coefficient: this is the edge.

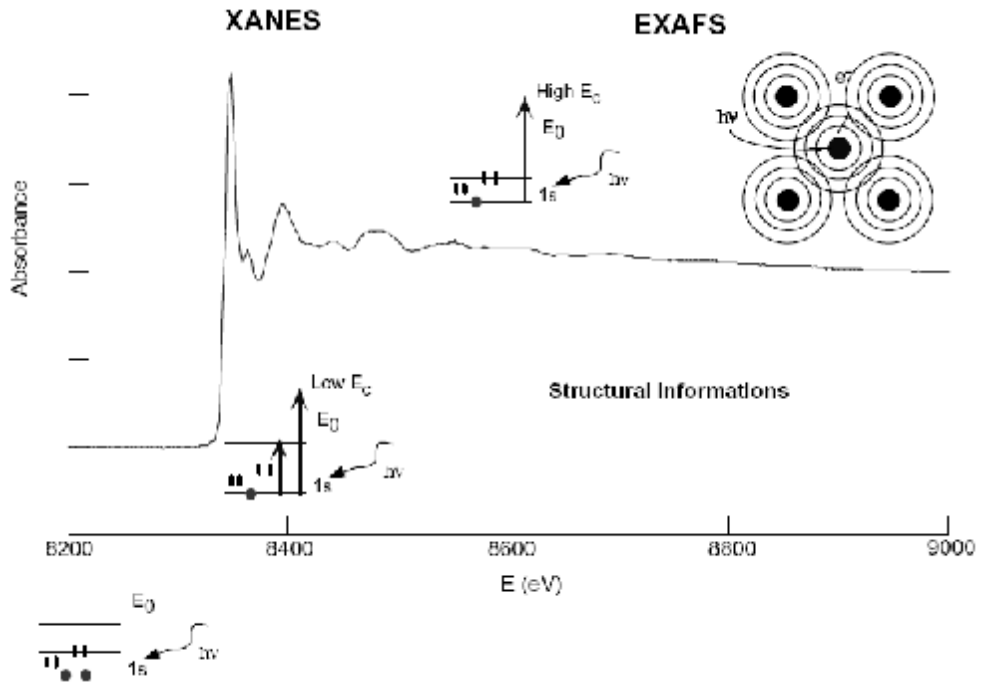

Figure 3.24. Ni K-edge x-ray absorption spectrum the molecule-based magnet CsNiCr(CN)6.(Koningsberger,1988)

When the energy becomes higher than E_o, a photoelectron is emitted with a kinetic energy E_c and transitions to continuum states occur. If the photoelectron is excited into the continuum with a high kinetic energy, the mean free path of the photoelectron is small (Figure 3.25) and a single scattering process takes place.

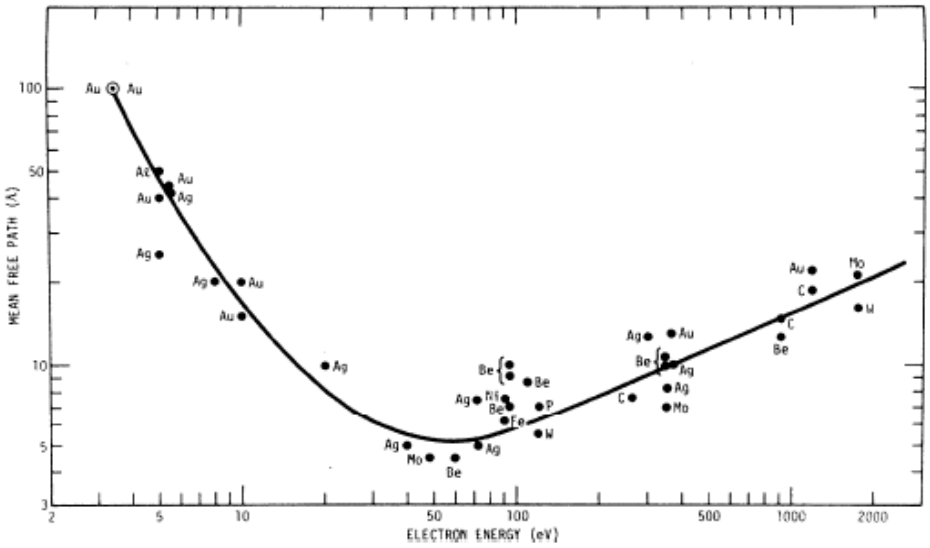

Figure 3.25. Universal curve for the electron mean free path as a function of the kinetic energy of the photoelectron (Koch , 1987).

This region, starting from about 50 eV after the edge, is the EXAFS region. EXAFS is sensitive to the short-range order and gives the radial distribution function around the absorber up to 4 or 5 Å at room temperature. At low kinetic energies, the mean free path of the photoelectron is longer and therefore, the photoelectron can be scattered by atoms located at larger distances and /or scattered many times (multiple scattering regime).This part of the spectrum is called the XANES region. It can be used to extract structural and electronic information on a selected atom, complementary to the ones coming from EXAFS.

The first is called the x-ray absorption near edge structure, or XANES for short. The XANES region generally consists of structure occurring in the pre-edge spectrum up to around 120 eV above the edge (Durham, 1988). Pre-edge features correspond to the excitation of core electrons to various bound states within the atom, i.e. transitions from the *1s* to the *nd*, (*n*+1)*s*, or (*n*+1)*p* orbitals for the K edge (Teo, 1986). The XANES features above the edge are generally due to a complex combination of effects including multiple scatterings, many body effects, band structures, etc (Bianconi, 1988). These structures provide information on the electronic configuration, orbital energetics, and site symmetry of the atom examined. Additionally, the edge position also provides information on the charge of the

absorbing atom, as a more positively charged atom will attract its core electrons more tightly, requiring slightly higher photon energies for photoionization (Williams and Lang, 1978). Unfortunately, the fundamental theory of XANES features is not as well understood as other aspects of XAS, and it is generally harder to calculate these features from first principles. Traditional quantitation by XANES involves using calibration curves based on either a pre-edge peak height or area vs. concentration in known standards (Szulczewski *et. al.*, 1997) or on edge energy shifts vs. the oxidation state of the standard (Bajt *et. al.*, 1994; Schulze *et. al.*, 1995).

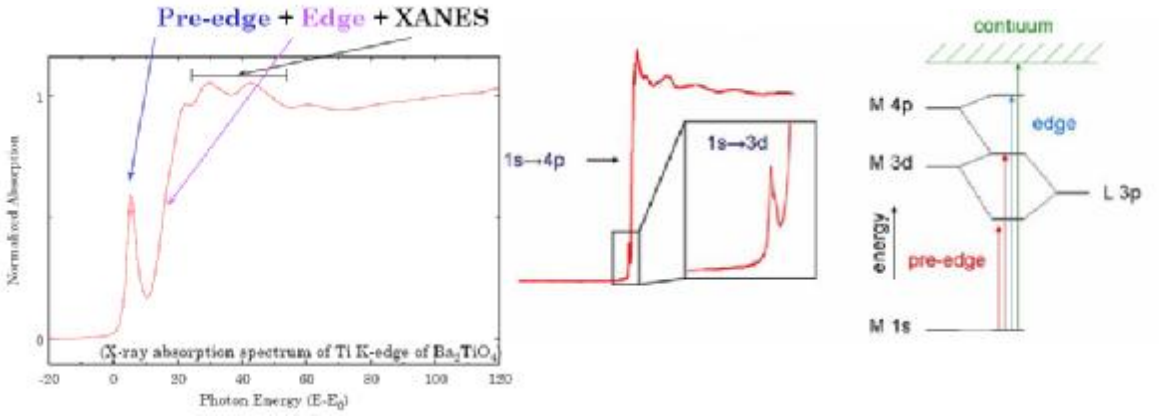

Figure 3.26. Typical spectrum and metal K-edge of XANES region (Bare, 2008)

XANES is strongly sensitive to the chemistry (formal oxidation state and geometry) of the absorbing atom. XANES directly probes unoccupied electronic states.

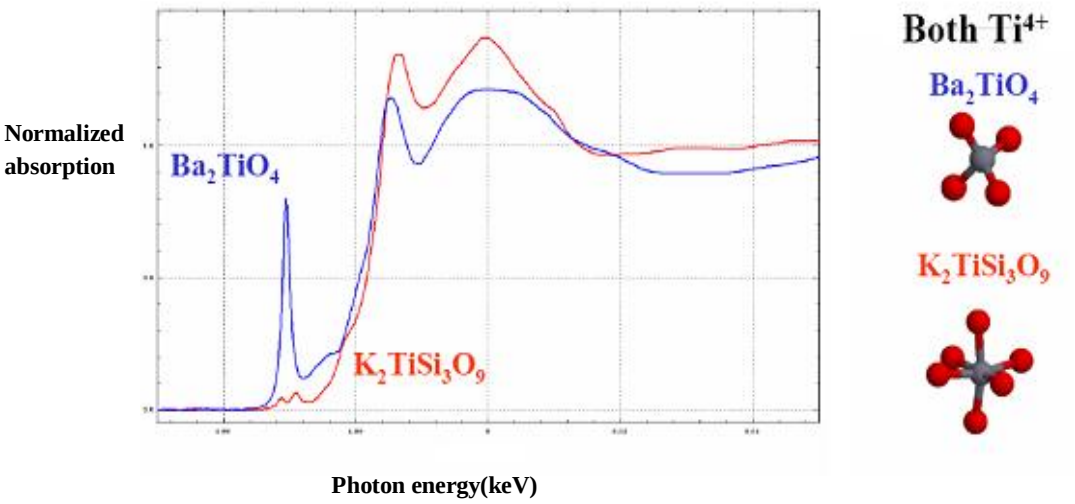

Figure 3.27. Ti K-edge XANES shows dramatic dependence on the local coordination chemistry (Bare, 2008)

3.8.3. EXAFS Region

The second region of interest in XAS is the Extended X-ray absorption fine structure (EXAFS). This region extends from the end of the XANES up to as much as 1200 eV above the edge. With the availability of the synchrotron radiation sources, x-ray absorption spectroscopy techniques (XAS) was developed into widely used tools for the structural research of materials by identifying the local structure around atoms of a selected type in the sample. In EXAFS (Extended X-ray Absorption Fine Structure) number and species of neighbour atoms, their distance from the selected atom and the thermal or structural disorder of their positions can be determined from the oscillatory part of the absorption coefficient above a major absorption edge. The analysis can be applied to crystalline, nanostructural or amorphous materials, liquids and molecular gases. EXAFS is often the only practical way to study the arrangement of atoms in materials without long range order. EXAFS spectroscopy is a powerful experimental tool to get structural information of the investigated material. EXAFS is the final state interference effect between the ejected photoelectron from the absorption process and it scattering from neighboring atoms. In a qualitative quantum mechanical sense, the probability that an inner shell core electron will absorb a photon depends on the difference between the initial state and the final states of the electron. The initial state consists of the localized core level

before the absorption event. The final state of the electron is that of the ejected photoelectron, which consists of photoelectron wave emanating from the atom. When, as in condensed matter, there are neighboring atoms, the outgoing photoelectron will be backscattered by these surrounding atoms. The intensity of the backscattered wave depends on numerous properties, including the neighboring atoms, the photoelectron wavelength, and the distance to the backscattering atoms. Thus the final state is a superposition of the outgoing wave and the sum of all backscattered waves. The constructive or destructive interference of these waves creates a modulation of the absorption coefficient above the edge. This is shown schematically in Figure 1.Where, (a):An x-ray photon is incident on an atom located on a lattice. The energy of the photon is high enough that it liberates an electron from a core state in the atom, and the photon is absorbed in the process.(b)-(c):The outgoing wavefunction of the photoelectron propagates from the absorbing atom as a spherical wave until it reaches one of the neighboring atoms.(d)-(e):The photoelectron wavefunction is scattered by the neighboring atoms, which then gives rise to a back scattered wave. The interference between the outgoing and back scattered wavefunctions gives rise to EXAFS oscillations in the absorption cross-section. (Nielsen, 2000)

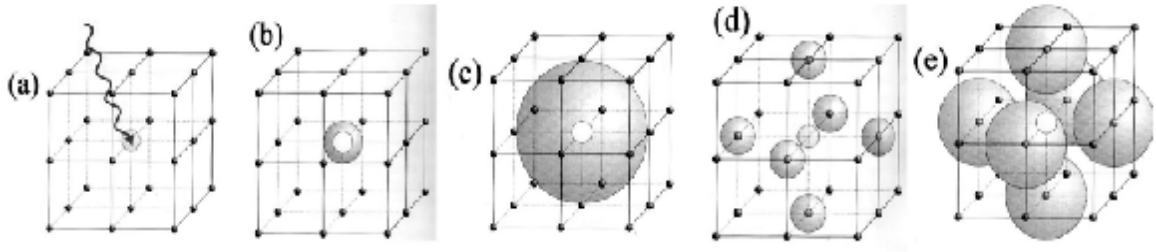

Figure 3.28. Schematic of an EXAFS process. (Nielsen,2001)

EXAFS appears above the absorption edges whenever the absorbing atom is closely surrounded by other atoms i.e. in solid state, in liquids or in molecular gasses. In case of free atoms, as for example in noble gasses or monatomic vapours (Rb vapour spectrum in Fig. 3.29), there is no EXAFS component in the absorption

spectrum. Also we can see difference between EXAFS and XANES process in Figure 3.30.

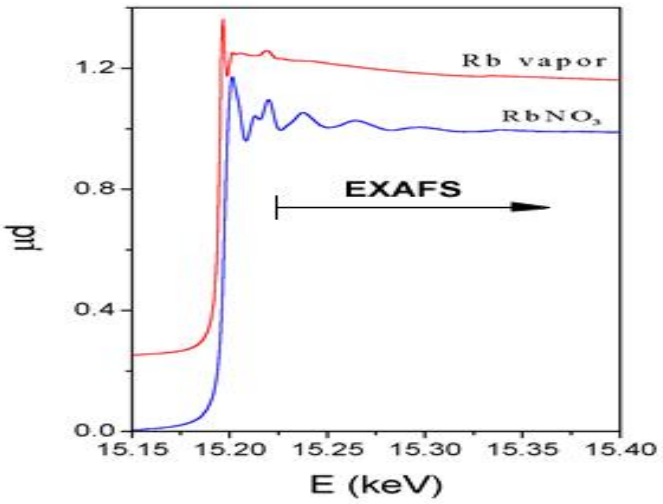

Figure 3.29. X-ray absorption spectra of RbNO3 water solution and rubidium vapour in the energy range of Rb K-edge (http://www.p-ng.si/~arcon/ exafs.htm)

(a) (b)

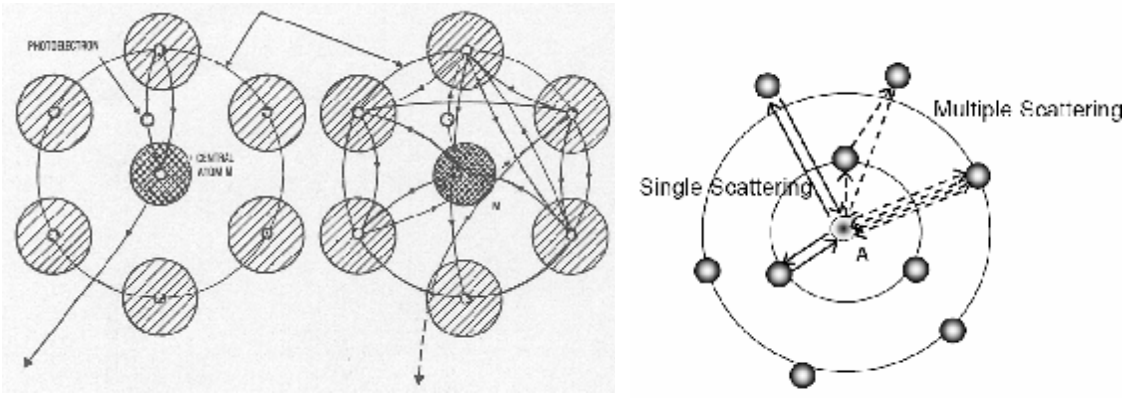

Figure 3.30. (a)An illustration of the EXAFS (left) and XANES (right) processes. EXAFS generally consists of single scattering events, where the outgoing photoelectron is scattered by a single neighboring atom. The XANES phenomenon is created by a complex set of multiple interactions with the neighboring atoms .(b)Scattering paths of an absorbing atom A on surrounding neighbors (Bianconi, 1988)

Many researchers have rigorously approached the theory of EXAFS. Kronig was one of the first investigators to propose that EXAFS was the result of a short-range order phenomenon rather than a large scale one (like diffraction). He proposed the current formulation of EXAFS as a final state wavefunction of the photoelectron caused by backscattering of local neighboring atoms (Kronig, 1932). A modern theoretical description of EXAFS based on ab initio parameters was developed in the early 1970's that has shown very good agreements with experimental data (Sayers ***et. al.***, 1970). The development of this theory has allowed the extraction of atomic parameters, such as coordination number, neighboring atom types, bond lengths, and disorder parameters. The modulations of the EXAFS (χ) normalized by "background" absorption can be given as:

$$\chi(E)=\frac{m(E)-m_o(E)}{\Delta m_o(E)} \tag{3.9.}$$

where $\mu(E)$ is the measured absorption coefficient, $\mu_o(E)$ is a smooth background function representing the absorption of an isolated atom, and $\Delta\mu_o$ is the measured jumpin the absorption $\mu(E)$ at the threshold energy E_o.

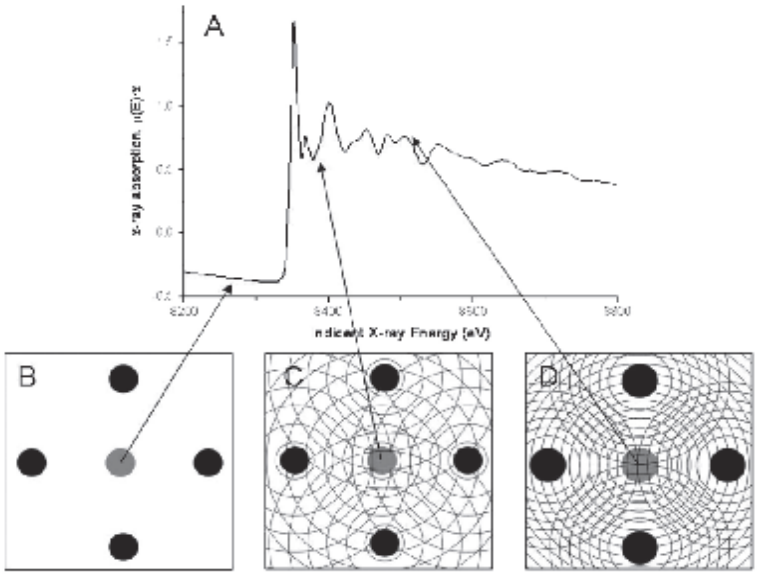

Figure 3.31.Illustration of the x-ray absorption process. (a) Nickel K-edge x-ray absorption spectrum of NiO. (b–d) Nickel absorber atom (gray filled circle) and four of six neighboring oxygen atoms (black filled circles). The crests of photoelectron waves produced by x-ray absorption by the absorber atom (Ni) and by scattering from neighboring oxygen atoms are shown as concentric circles about Ni and Oatoms, respectively. (b) At x-ray energies below the absorption edge no photoelectron is produced. (c) At energies close to but above the absorption edge, the photoelectron wavelength is longer than at higher energies. This particular wave produces a minimum in the oscillatory part of the absorption coefficient because the outgoing and scattered parts of the hotoelectron meet at a minimum at the absorbing atom; that is, the peak crests are completely out of phase at the center of the absorber atom. (d) At higher x-ray energies the wavelength of the photoelectron is shorter than shown in c. This particular wave produces a maximum in the oscillatory part of the absorption coefficient because the outgoing and scattered parts of the photoelectron are in phase and meet at a maximum at the absorber atom.(Kelly,2000)

EXAFS is best understood in terms of the wave behavior of the photo-electron created in the absorption process. Because of this, it is common to convert the x-ray energy to k (wave number), the wave number of the photo-electron, which has dimensions of 1/distance and is defined as

$$k = \sqrt{\frac{2m(E - E_o)}{\mathbf{h}^2}} \qquad (3.10.)$$

where E_o is the absorption edge energy and m is the electron mass. From energy to wave number conversion using Athena EXAFS data analysis programme is shown in figure 3.32.

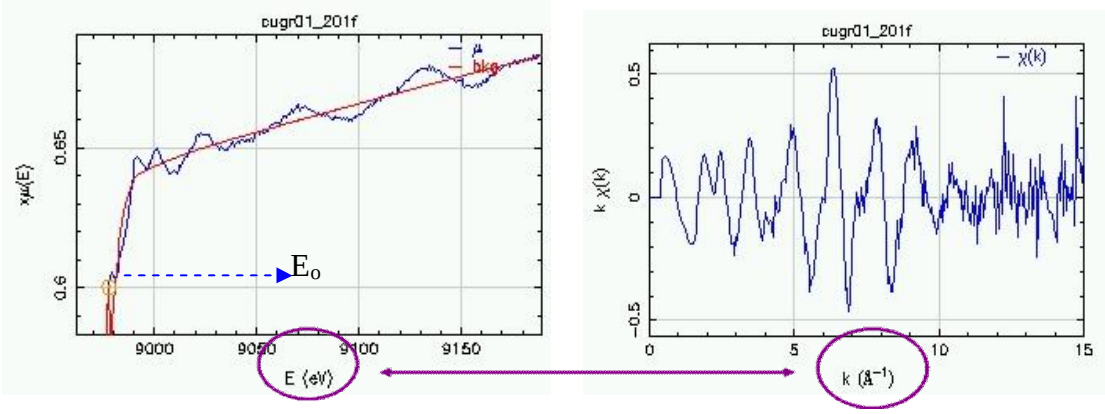

Figure 3.32. Energy to wave number conversion (Kelly, 2008)

The primary quantity for EXAFS is then χ(k), the oscillations as a function of photo-electron wave number, and χ(k) is often referred to simply as "the EXAFS". In this way, the EXAFS extracted from the Fe K-edge for FeO is shown in Fig 3.33 (left side). As you can see, the EXAFS is oscillatory and decays quickly with k. To emphasize the oscillations, χ(k) is often multiplied by a power of k typically k^2 or k^3, as shown in Fig 3.33 (right side). The different frequencies apparent in the oscillations in χ(k) correspond to different near-neighbor coordination shells which can be described and modeled according to the EXAFS Equation,

$$c(k) = \sum_j \frac{N_j f_j(k) e^{-2k^2 s_j^2}}{kR_j^2} Sin[2kR_j + d(k)] \qquad (3.11.)$$

where f(k) and δ(k) are scattering properties of the atoms neighboring the excited atom, N is the number of neighboring atoms, R is the distance to the neighboring atom, and σ^2 is the disorder in the neighbor distance. Though somewhat complicated, the EXAFS equation allows us to determine N, R, and σ^2 knowing the scattering amplitude f(k) and phase-shift δ(k). Furthermore, since these scattering

factors depend on the Z of the neighboring atom, EXAFS is also sensitive to the atomic species of the neighboring atom. (Newville, 2005)

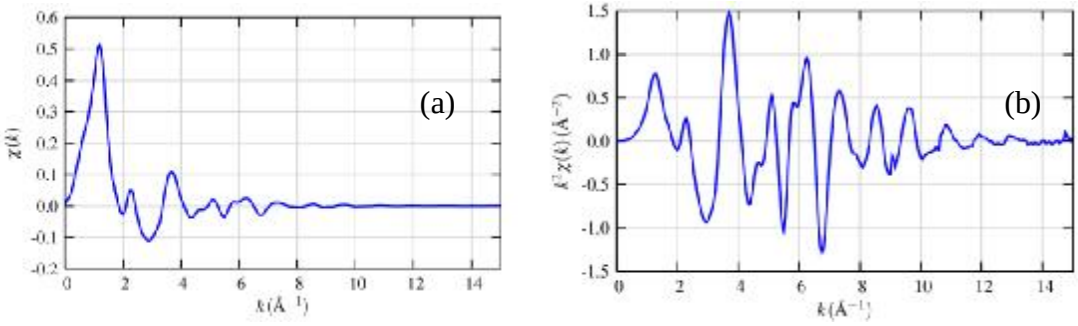

Figure 3.33. (a) Isolated EXAFS χ(k) for FeO , and (b) the k-weighted XAFS, k^2 χ(k) (Newville, 2005)

We start with the photoelectric effect, now shown in Fig 3.34, in which an x-ray is absorbed by a core-level with binding energy, and a photo-electron with wave number k is created and propagates away from the atom. When an x-ray has the energy of a tightly bound core electron level, E_0, the probability of absorption has a sharp rise. In the absorption process, the tightly bound core-level is destroyed, and a photo-electron is created. The photoelectron travels as a wave with wave number proportional to $(E - E_0)^{1/2}$

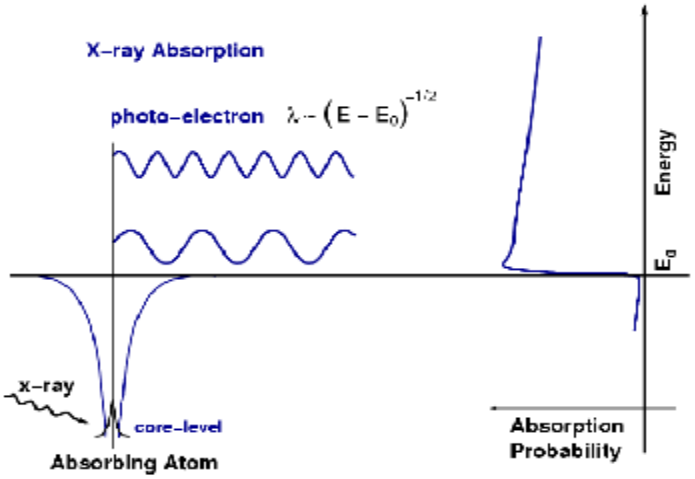

Figure 3.34. Illisturation of x-ray absorption through the photoelectric process. (Newville, 2005)

An important point for the discussion here is that the absorption due to a given core-level relies on there being an *available state* for the photo-electron: a quantum state at exactly the right energy, and also the right angular momentum state. If there is no available state, there will be no absorption from that core level. For example, at energies below the 1s binding energy, a 1s electron could only be promoted to a p valence level below the binding energy (or Fermi level). Since all the available valence levels are filled by the valence electrons, there is no state for the 1s electron to fill, and so there is no absorption from that core-level. There is still some absorption, of course, because higher level electrons can be promoted into the continuum.

When a neighboring atom is included in the picture (Fig.3.35), the photo-electron can scatter from the electrons of this neighboring atom, and the scattered photo-electron can return to the absorbing atom. Since the absorption coefficient depends on whether there is an available electronic state (that is whether there is an electron at the location of the atom and at the appropriate energy and momentum), the presence of the photo-electron scattered back from the neighboring atom will alter the absorption coefficient: This is the origin of XAFS.

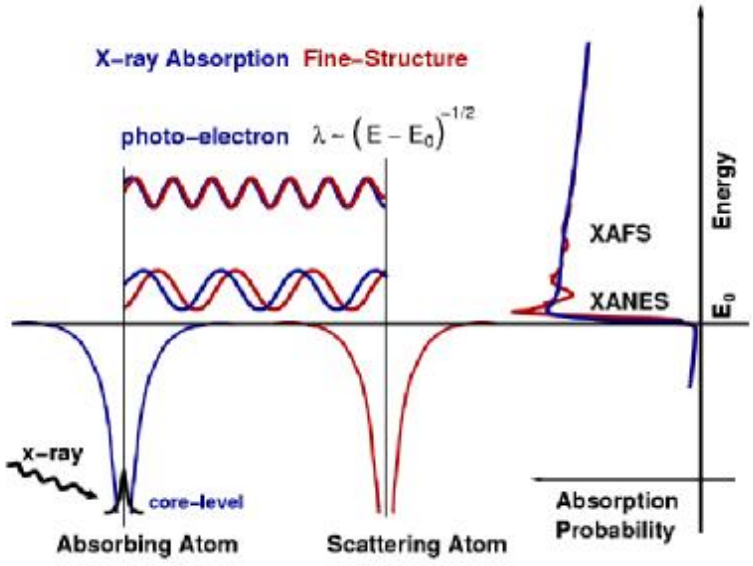

Figure 3.35. The modulates in the absorption coefficient μ(E), causing the EXAFS. (Newville, 2005)

X-ray absorption probability can be calculated using standard quantum theory. x-ray absorption is a transition between two discrete quantum states (from an initial state with an x-ray, a core electron, and no photo-electron to a final state with no x-ray, a core hole, and a photo-electron), we describe μ(E) per unit time from the ground state <i| to a final state |f> with Fermi's Golden Rule:

$$\mu(E) \alpha \sum_f |\langle i|H|f\rangle|^2 \delta(\hbar\omega - E_f + E_i) \quad (3.12.)$$

where <i| represents the initial state (an x-ray, a core electron, and no photo-electron), |f> is the final state (no x-ray, a core-hole, and a photo-electron), $\delta(\hbar\omega - E_f + E_i)$shows conservation of energy and H (Hamiltonian) is the interaction protobation. Since the initial state is closely bound to the probed atom, it is not really changed from the free atom core electron state. However, f, the final state, is affected by the local environment around the atom, because the electron is ejected to outside the valence shell. We can split the final state into two parts: one which reflects the free atom's final state, and an extra part that reflects the effect of placing the atom in its local environment:

$$|f\rangle = |f_o\rangle + |\Delta f\rangle \quad (3.13.)$$

where f_0 is the unperturbed state, and Δf is the alteration to the state due to the addition of the neighboring atoms. To be more specific, the interaction Hamiltonian can be written from field theory as:

$$H_{int} = \frac{-e}{mc}\vec{A}.\vec{p} + \frac{e^2}{2mc^2}\vec{A}.\vec{A} - \vec{m}.\vec{B} \quad (3.14.)$$

where the quantum field theory $\vec{A}$ is a 4-vector:

$$Aa \sum_{k,a} e_v [a_{k,a}(t) e^{i\vec{k}.\vec{r}} + a^{\Theta} e^{i\vec{k}\vec{r}}] \quad (3.15.)$$

k is the wave vector for some part of the total field, and ϵ is the corresponding polarization. There are two operators: the a operator, and the $a^{\dagger}$ operator, which correspond to creator and annihilating operators for individual photons of a given k vector and polarization. What we need is a single annihilator operator which will destroy an incoming x-ray photon and couple the initial core state to a near free electron state in the continuum of the material in question. In the interaction Hamiltonian H_{int} ,only the $\mathbf{A} \cdot \mathbf{p}$ term leads to a single annihilator operator, since $\boldsymbol{B}=$ Ñ**x*A*,** and $\mathbf{A} \cdot \mathbf{A}$ will lead to 4 second order annihilate, annihilate-create, create-annihilate, and create-create, which are irrelevant since we examine one photon. Therefore, we drop all terms except the annihilator term and obtain the interaction (and thus the absorption) between the final and initial states, for a given photon of wave vector $\vec{k}$;

$$m(E)\ a\ |\langle f|H_{int}|i\rangle|^2\ a\ |\langle f(0g)|\ e_m a_{k,a}(t)\ e^{\vec{ikr}}\ |i\ (1g\ of\ k,\ e)\rangle|^2 \qquad (3.16.)$$

It is therefore easy to see that the nature of the incoming photon, by virtue of its wavevector, will mix with the initial and final states. Going back to our "bare" and added final states, we expand the equation above by changing $\langle f|$ to $\langle f_o|$ and $\langle \Delta f|$:

$$m(E)\ a\ |\langle fo|H_{int}|i\rangle|^2\ [1+Df\ |H_{int}|i\rangle \frac{\langle f_o|H_{\text{int}}|i\rangle^*}{|\langle f_o|H_{\text{int}}|i\rangle^2} + C.C.] \qquad (3.17.)$$

where C.C. is the complex conjugate of the second term. We then define:

$$m(E) = m_o(E)[1+c(E)]\ so, \qquad (3.18.)$$

$$c(E)\ \alpha\ \langle \Delta f|H_{int}|i\rangle \qquad (3.19.)$$

where m_o is the smooth-line absorption given by $\alpha\ Z^4$, $c(E)$ and is the fine structure which deviates from the expected absorption.

If we assume that the outgoing photoelectron (in other words, the Δf, the portion of the wave function that is not a bound state to the absorbing atom) is a traveling spherical wave which bounces back with scattering properties $f(k)$ and $\delta(k)$ from a neighboring atom a distance R away:

$$<Df|=(\varphi(k,r))_{scatteredatR}=\frac{e^{ikR}}{kR}(2kf(k)e^{id(k)})\frac{e^{ikR}}{kR}\,e^{ikr} \qquad (3.20.)$$

and that the initial wave function $|i>$ is nearly a $\delta(r)$function because the electron is a tightly bound core level near the nucleus, then:

$$\chi(k)\ a\ \int drd(r)=j(k,0)=\frac{e^{ikR}}{kR}(2kf(k)e^{id(k)})\frac{e^{ikR}}{kR}+C.C. \qquad (3.21.)$$

where C.C. is the complex conjugate. Where $f(k)$ and $\delta(k)$ are scattering properties of the neighboring atom (Wu, 2004). These scattering factors depend on the Z of the neighboring atom, as shown in Fig 3.36. These scattering factors make EXAFS sensitive to the atomic species of the neighboring atom. Combining these terms in and including the complex conjugate to make sure we end up with a real function, we get

$$\chi(k)=\frac{f(k)}{kR^2}\sin\{2kR+d(k)] \qquad (3.22.)$$

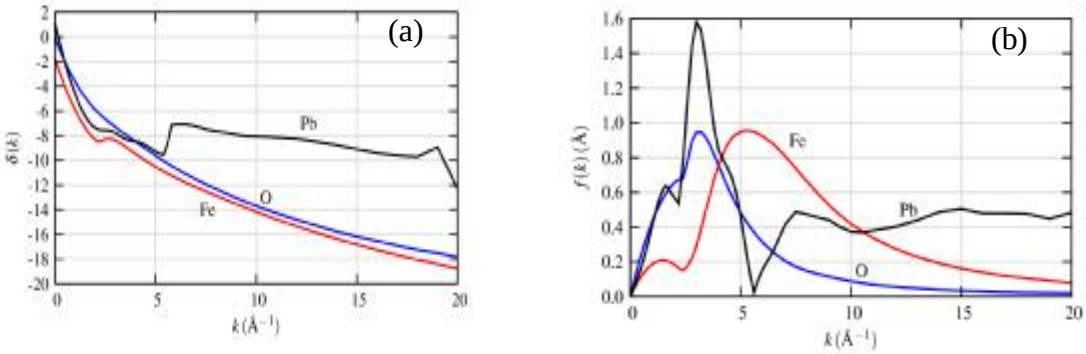

Figure 3.36. (a) Functional forms for *f(k)* and (b) δ(k) for O, Fe, and Pb showing the dependence of these terms on atomic number Z. The variations in functional form allow Z to be determined (±5 or so) from analysis of the EXAFS.(Newville,2005)

f(k) is an amplitude reduction factor which accounts for many-body effects at the central atom (Teo, 1986).The total phase shift of the photoelectron from the backscattered shell is given by δ*(k).* This total phase shift is illustrated in fig. 3.37.

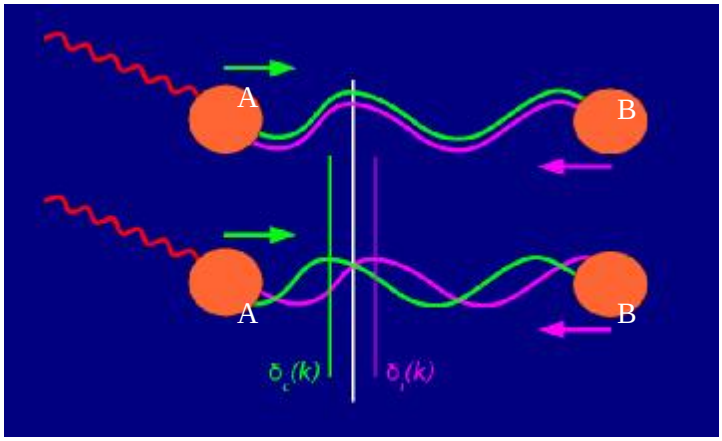

Figure 3.37. Illustration of phase shift (Stern, 1988)

which looks much like the XAFS equation above. The treatment here was for one pair of absorbing atom and scattering atom, but for a real measurement we'll average over millions of atom pairs. Even for neighboring atoms of the same type, the thermal and static disorder in the bond distances will give a range of distances that will affect the XAFS. As a first approximation, this disorder will change the XAFS equation to

$$\chi(k)=\frac{Ne^{-2k^2s^2}f(k)}{kR^2}\sin[2kR+d(k)] \qquad (3.23.)$$

where N is the coordination number and σ^2 is the mean-square-displacement in the bond distance R. More sophisticated and general approaches to thermal and static disorder, including non-Gaussian distributions of atomic distributions are possible (and routinely used in analysis), but are beyond the scope of the treatment here. $e^{-2k^2s^2}$ is also called Debye-Waller factor. The effect of Debye –Waller is shown in fig 3.38.

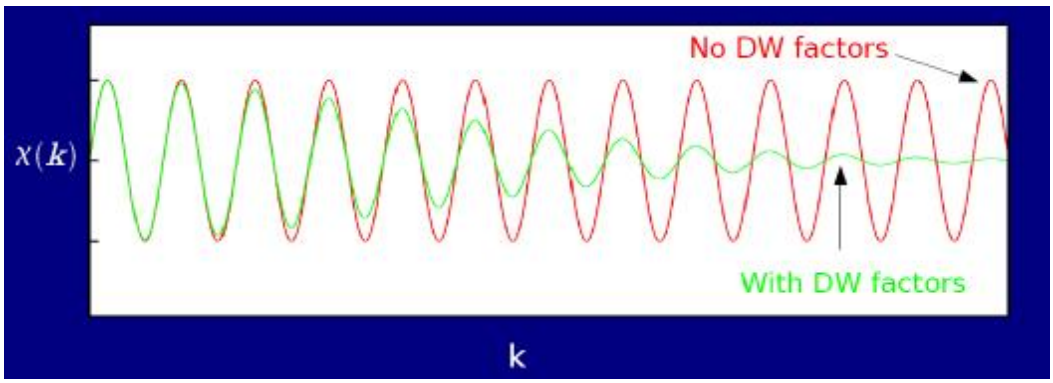

Figure 3.38. Debye-Waller factor (Stern, 1988)

Of course, real systems usually have more that one type of neighboring atom around a particular absorbing atom. This is easily accommodated in the XAFS formalism, as the measured XAFS will simply be a sum of the contributions from each scattering atom type (or *coordination shell*, as it is often called – the terms *coordination sphere* and *scattering path* are also used),

$$\chi(k)=\sum_j \frac{N_j e^{-2k^2s_j^2} f_j(k)}{kR_j^2}\sin[2kR_j+d(k)] \qquad (3.24.)$$

where *j* represents the individual coordination shell of identical atoms at approximately the same distance from the central atom. In principle there could be many such shells, but as shells of similar Z become close enough (i.e., within a 0.05A° of each other), they become difficult to distinguish from one another.

We neglected the fact that the photo-electron can also scatter *inelastically* from other sources other conduction electrons, phonons, and so on. In order to participate in the XAFS, the photo-electron has to scatter from the neighboring atom and return to the absorbing atom *elastically* (i.e., at the same energy) as the outgoing photo-electron. In addition, the photo-electron has to make it back to the absorbing atom before the excited state decays (i.e., before the core-hole is filled). Photoelectron and core hole have finite lifetimes. To account for both the inelastic scattering and the *core-hole lifetime*, we use a damped spherical wave

$$\psi(k,r) = \frac{e^{ikr} e^{-2r/l(k)}}{kr} \qquad (3.25.)$$

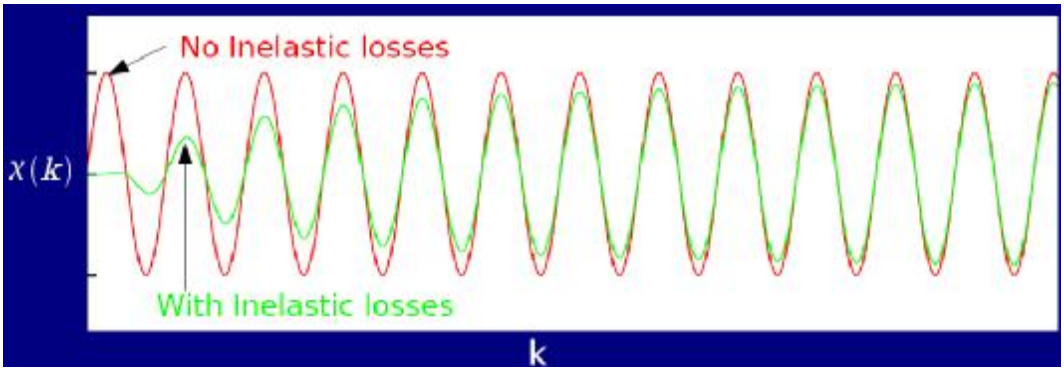

Figure 3.39. Inelastic losses (Stern, 1988)

as the photo-electron wave-function where λ is the mean-free-path of the photo-electron (that is, how far it typically travels before scattering inelastically and before the core hole is filled). The mean-free-path is typically 5 to 30°A and has a significant but fairly universal dependence on *k*, shown in Fig14. Including the λ(k), the EXAFS equation becomes

$$\chi(k)=\sum_j \frac{N_j e^{-2k^2 s_j^2} e^{-2R_j/l(k)} f_j(k)}{kR_j^2} \sin[2kR_j + d(k)] \qquad (3.26.)$$

from this equation, we can draw a few physical conclusions about XAFS. First, because of the λ(k) term and the R^{-2} term, XAFS is seen to be an inherently *local probe*, not able to see much further than 5 or so Angstroms from the absorbing atom. Second, the XAFS oscilations will consist of different frequencies that correspond to the different distances for each coordination shell. This will lead us to use Fourier transforms in the analysis. Finally, in order to extract the distances and coordination numbers, we need to have accurate values for the scattering amplitude and phase shifts *f(k)* and δ(k).

In short, the physical model which gives the formula is the following:

1) the kinetic energy of the ejected electron (by the photon) is enough to treat the electron as a free electron. The wave function which describes the interaction of the electron with the atomic potentials is a plane wave.

2) the electron is simply scattered by the neighbors atoms. The interference between the outgoing wave and the scattered one is responsible of the absorption coefficient modulations.

3) the absorber and the scatterer have to be close to give this interference phenomenon. The process is local, the characteristic interaction distance is given by the mean free path λ.

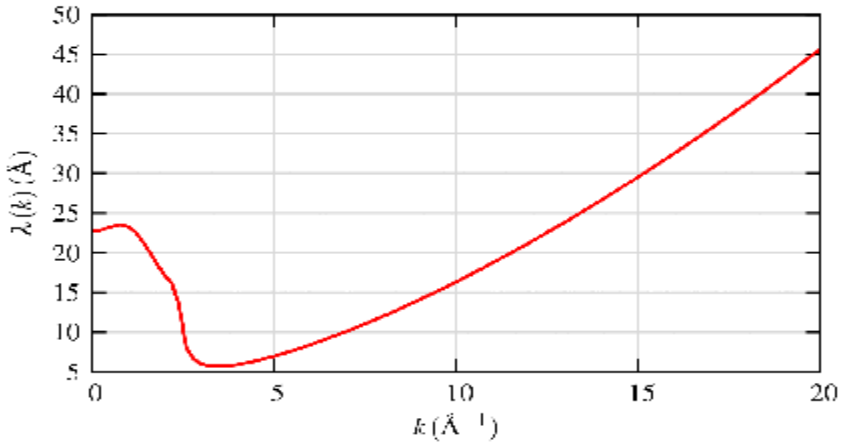

Figure 3.40. The photo-electron mean-free-path for XAFS λ(k),, representing how far the photo-electron can travel and still participate in the XAFS. This term includes both the inelastic scattering of the photo-electron, and the effect of the finite lifetime of the core-hole.(Newville, 2004)

It has been shown by Sayers, *et. al.*, 1971, that the isolated EXAFS can be Fourier transformed to determine the bond distances of the scattering atoms as a radial distance from the central absorbing atom. This analysis provided a key step in the development of modern XAS theory (Sayers *et. al.*, 1971). The transform actually only gives a pseudoradial distribution function (RDF), as corrections for phase shifts must be applied to get the real distances. Figure 15 shows several of the steps in the data reduction process, from the raw spectrum, the normalized “unit step” spectra, the isolated EXAFS, and the Fourier transformed RDF.

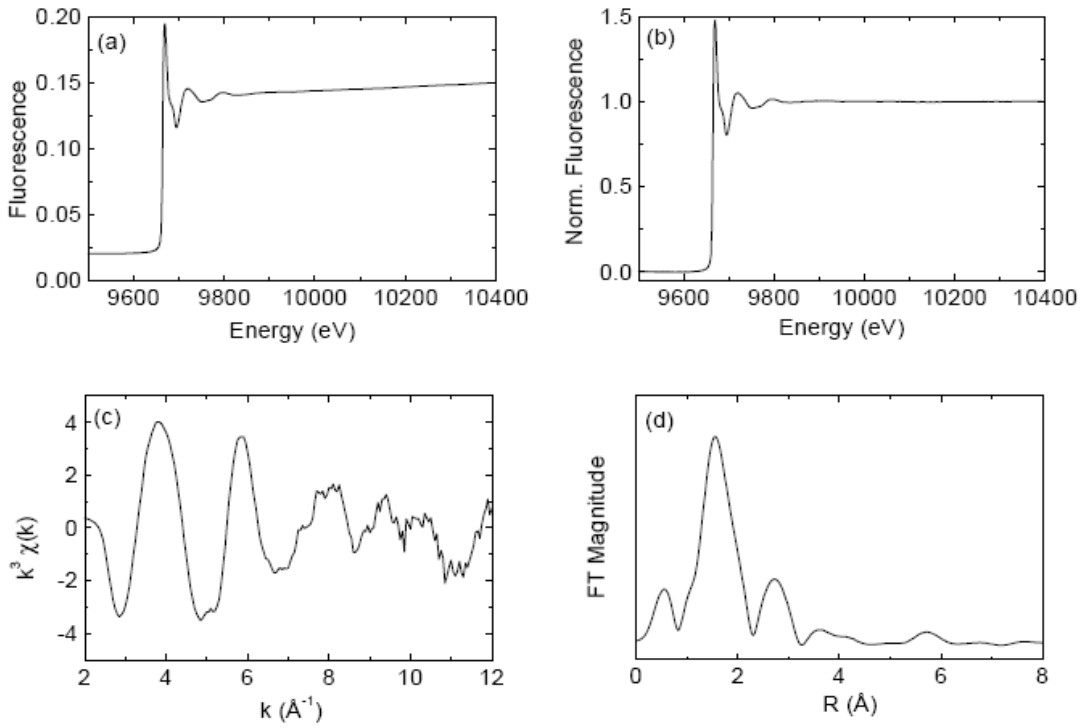

Figure 3.41. Plots showing the various steps in the data reduction steps in the analysis of EXAFS data: (a) raw data, (b) normalized spectra, (c) isolated and weighted EXAFS signal, (d) radial distribution function.

3.9. Data Analysis

3.9.1. Introduction

All EXAFS datas were analyzed by IFEFFIT which includes ATHENA and ARTEMIS programme. IFEFFIT is a command-line program and an interactive program for XAFS analysis. It includes high-quality algorithms specific to XAFS Analysis: For background removal, it uses the AUTOBK algorithm, and for fitting EXAFS chi(k) and FEFFIT with graphical display of XAFS data and general data manipulation. IFEFFIT was developed primarily by Matt Newville at CARS, the Consortium for Advanced Radiation Sources, at The University of Chicago. It is introduced a new software package for analysis of XAS data. This package is based on the Ifeffit library of analytical and numerical algorithms and uses the perl/Tk

graphics toolkit. The two main components are Athena, a program for XAS data processing, and Artemis, a program for EXAFS data analysis using theoretical standards from Feff. These programs provide high quality analytical capabilities in a manner that is accessible to novices yet powerful enough to meet the demands of an expert. The programs run on all major platforms and are freely available under the terms of a free software license. Paralel to xafsX and rmcxas programs for XAFS data processing and the EXAFS data analysis, respectively, ATHENA and ARTEMIS programs (Ravel 2005) were used as well. The ATHENA and ARTEMIS use the programmer's interface to IFEFFIT (Newiville 1993). The ATHENA is used for data processing (spectra normalization and background subtraction by AUTOBK algorithm). The ARTEMIS takes the experimental $\chi(k)$ function and compares it with a theoretical that is build-up using the theoretical EXAFS paths previously calculated with FEFF 8.2. The FEFF input files were created using ATOMS (Ravel, 2001) and ZnO crystallographic data built in ARTEMIS.

3.9.1.1. ATHENA Software

ATHENA is used for all the main steps in data processing including conversion of raw data to $\mu(E)$ spectra, background subtraction, Fourier transforming and plotting. As such it is useful for data visualization at the beamline as well as for processing of data in preparation for data analysis. The normal view of the ATHENA window is shown in Fig. 3.42(a) and (b)

(a)

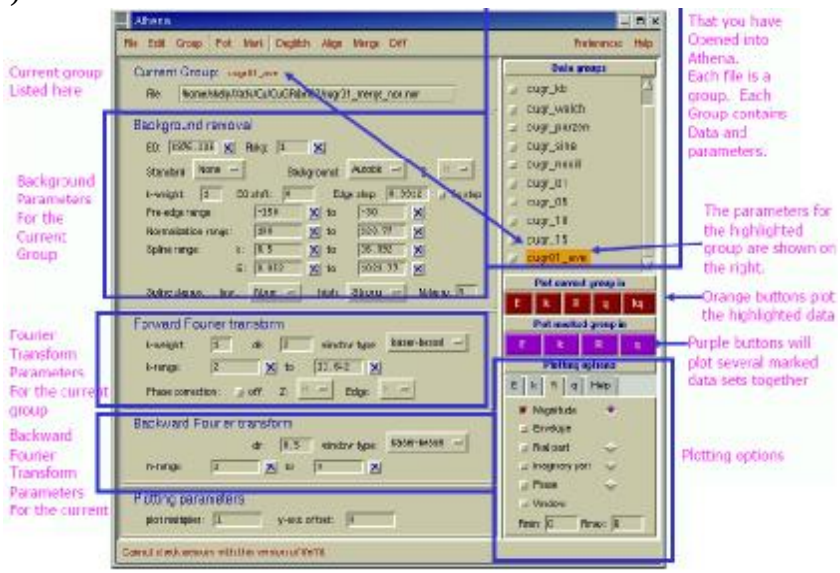

(b)

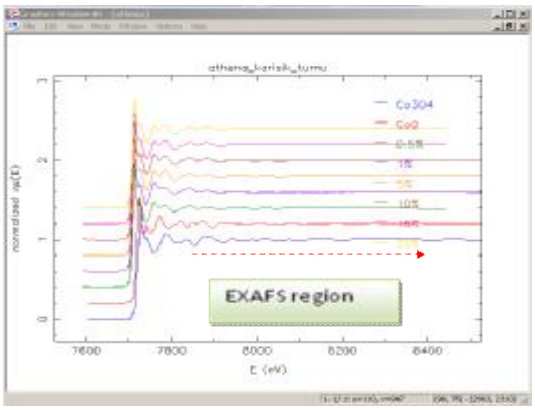

Figure 3.42.(a)The main window of the ATHENA program (b)The data sets imported int The analysis parameters for the selected data set are displayed in the main panel on the left.

Data conversion from its raw form is handled in a flexible manner, creating μ(E) spectra from transmission, fluorescence or electron yield experiments. The conversion utility allows for on-the-fly summation of data from a multi-element detector. Alternately, each column of multi-element data can be imported as individual data groups for later inspection and summation. ATHENA also supports powerful preprocessing of data as it is imported, including automated deglitching, truncation, alignment and constraint of analysis parameters.(Ravel,2005)

we can summary in the following the features of ATHENA;

• Convert raw transmission or fluorescence data into μ(E) spectra

• Deglitch by point selection or by an algorithm

• Merge spectra and compute the standard deviation spectrum

• Align and calibrate data

• Compute difference spectra for XANES, dichroism, and EXAFS

• Remove background using the Autobk algorithm

• Normalize to Cromer Liberman calculations

• Perform forward and backward Fourier transforms with optional central atom phase corrections

• Do log-ratio/phase-difference analysis

• Fit peak shapes to XANES data

• Do data truncation and data smoothing

• Plot individual or many data sets in k-, R-, or back-transform k-space

• Constrain background removal and Fourier transform parameters between data sets in a flexible way

• Process and visualize large quantities of data easily

• Use of theoretical fitting standards from Feff

• Fit using single or multiple data sets

• Fit using single or multiple Feff calculations

• Co-refinement of a background spline to uncover correlations between the background
and the fitting parameters

• Fit using one or more values for the k-weight

• Set arbitrary constraints between and restraints on fitting parameters

• Plot in k, R, or back-transformed k-space

• Plot the data, the best-fit function and the background spline as well as the individual
paths

• Report on fitting statistics, including error bars on and correlations between variables

ATHENA provides tools for the analysis of near-edge spectra. There are utilities for calculation of difference spectra, for fitting line shapes (arctangent, Gaussian, Lorentzian) to spectra, and for fitting linear combinations of standard spectra to unknown spectra. ATHENA can also import and display the results of FEFF8 calculations (Ankudinov et al., 1998) for comparison with measured data.

3.9.1.2. ARTEMIS Software

ARTEMIS works within the framework of FEFF's multiple-scattering path expansion (Zabinsky et al., 1995; Rehr & Albers, 1990).This means that the data are described as a summation of one or more scattering paths as computed by FEFF. For each path, the XAFS equation must be evaluated. This means that values of the parametric terms in the EXAFS equation, N, S^2_0, E_0, R and σ^2, must be specified for each path included in the fit. The path expansion and how it is parameterized and used in a fit is described elsewhere (Newville et al., 1995; Ravel, 2000). As discussed in those references, EXAFS analysis can be quite subtle and complicated. By providing a graphical forms-based mechanism for handling the many bookkeeping chores required by FEFF and IFEFFIT, ARTEMIS makes basic analysis chores simple and sophisticated analysis problems tractable. Shown in Fig. 3.43 is the ARTEMIS window in its data view. The dataprocessing parameters, including the range of the Fourier transform from k-space and the fitting range in R-space, are set in the main window. The far right panel is used to control how plots are displayed. The middle panel is a list of all data sets, FEFF calculations and paths used in the fit. This list is integral to the generation of plots and is used to determine which view is displayed in the main window. Other views (not shown) allow the user to set fitting parameters, to examine log files from previous fits, to manage FEFF calculations or to manage individual FEFF paths and the mathematical expressions used to evaluate the terms in the EXAFS equation.ARTEMIS includes access to the functionality of the ATOMS (Ravel, 2001) program, which converts crystallographic data into a format suitable for FEFF. This interface can read crystallographic data either in the form of an ATOMS input file or a crystallographic information file

(CIF) (Hall et al., 1991). These data are then converted into a FEFF input file or can be converted into a form suitable for export to a molecule viewer. For materials that are not crystalline or do not have a crystalline analogue, FEFF input files prepared in some other way can be imported directly into ARTEMIS.A simple interface to FEFF is included in ARTEMIS. This is little more than a simple text editor for altering the contents of the input file as needed and a button for launching an external instance of FEFF. Fortunately, this simple interface is quite adequate for the needs of EXAFS data analysis. After the FEFF run, ARTEMIS displays a page containing a concise interpretation of the paths computed by FEFF including the path distances, degeneracy, atomic species in the path, whether the path is single- or multiple-scattering,and estimated importance of the path. ARTEMIS has tools for organizing and plotting the results of the calculation, including plotting the individual contributions of each path in both k- and R-space.

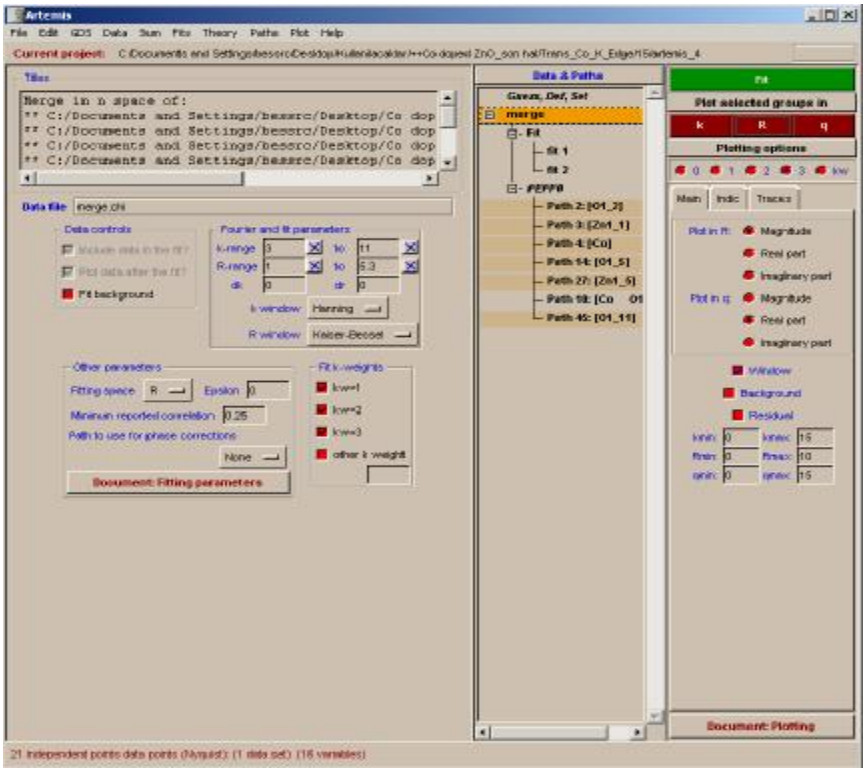

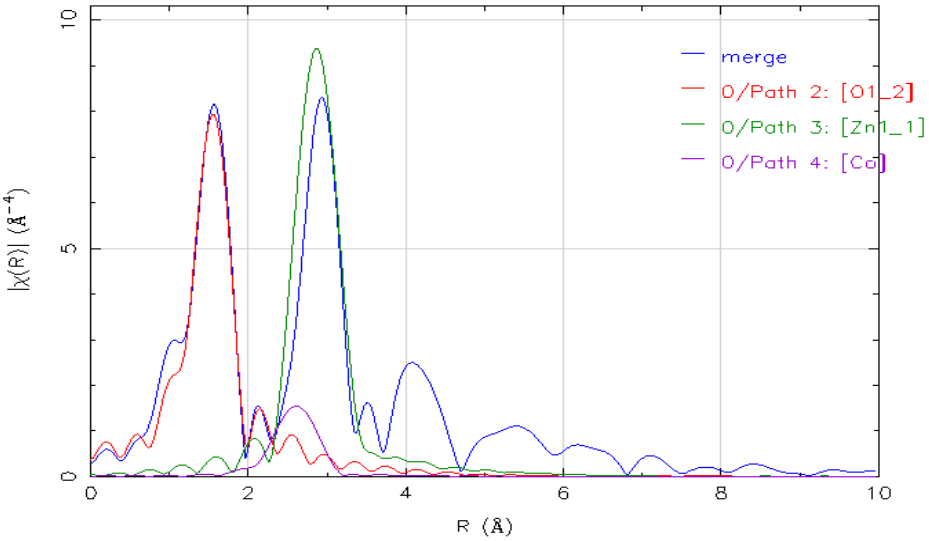

Figure 3.43 .The main window of the ARTEMIS program. Shown in the main panel is the view for setting the Fourier transform and fit range parameters. The middle panel lists all data sets and FEFF paths used in the fit and provides a history of all fits performed within the project. The panel on the right contains plotting controls.

4. EXPERIMENTAL RESULTS

4.1. Synthesis Products

The chemical analysis by Atomic Absorption Spectroscopy (AAS) shows that the actual Co concentration in the synthesized nanoparticles is systematically higher compared to the nominal concentration of the precursor mixture used in figure 4.1. It is also observed that the evaporation rate of the precursor mixture as determined from its mass loss is enhanced with increasing Co concentration (Fig. 4.1 (b)) which may explain the systematic deviation of actual and nominal Co concentration.

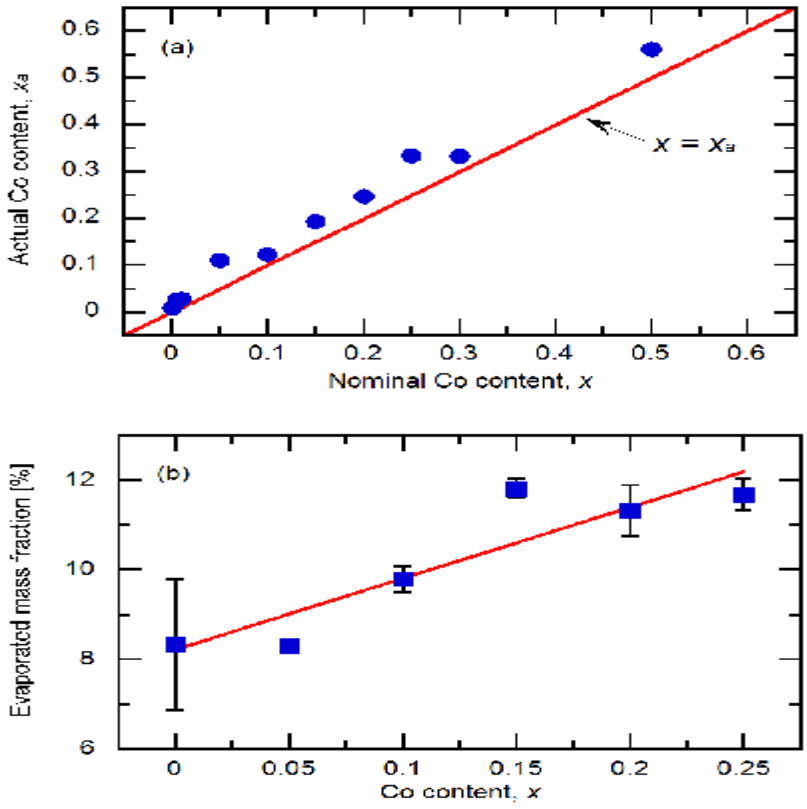

Figure 4.1. (a) Correlation between actual, x_a, and nominal, x, Co content, (b)precursor evaporation rate as a function of Co content

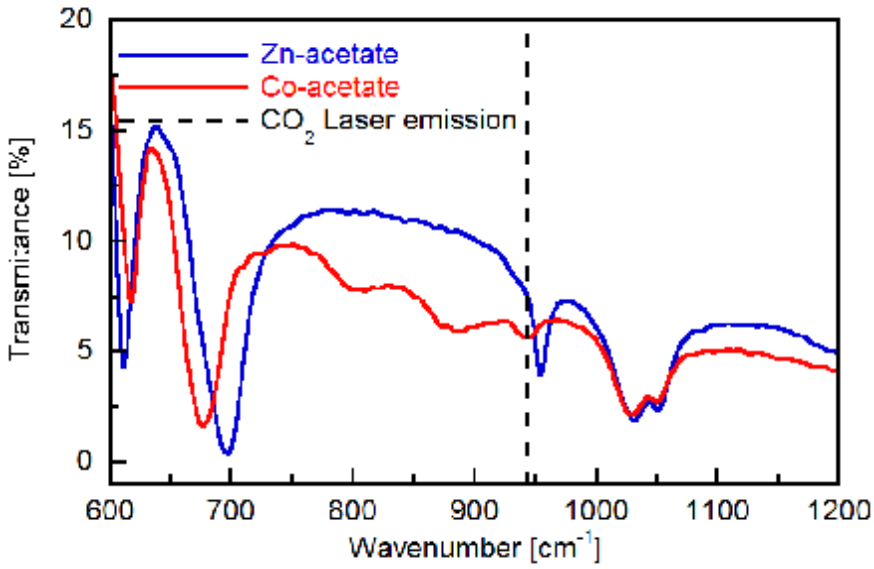

Figure 4.2. Comparison of FTIR spectra of the two precursor materials and the emission line of the CO_2 laser (wavelength of 10.6 μm).

In figure 4.2 shows Fourier transform infrared (FTIR) spectroscopy. Fourier transform infrared (FTIR) spectroscopy is a measurement technique for collecting infrared spectra. Instead of recording the amount of energy absorbed when the frequency of the infra-red light is varied (monochromator), the IR light is guided through an interferometer. After passing through the sample, the measured signal is the interferogram. Performing a mathematical Fourier transform on this signal results in a spectrum identical to that from conventional (dispersive) infrared spectroscopy.

In figure 4.3 XRD patterns of as-synthesized $Zn_{1-x}Co_xO$ nanoparticles are presented. The substitution of Co did not cause remarkable changes in the diffraction patterns for the Co content of $x \leq 0.25$. Rietveld refinement of XRD data shows that those particles are of wurtzite structure, while in particles with Co concentration $x \geq 0.30$ CoO and Co_3O_4 are present as additional phases (Fig. 4.4).

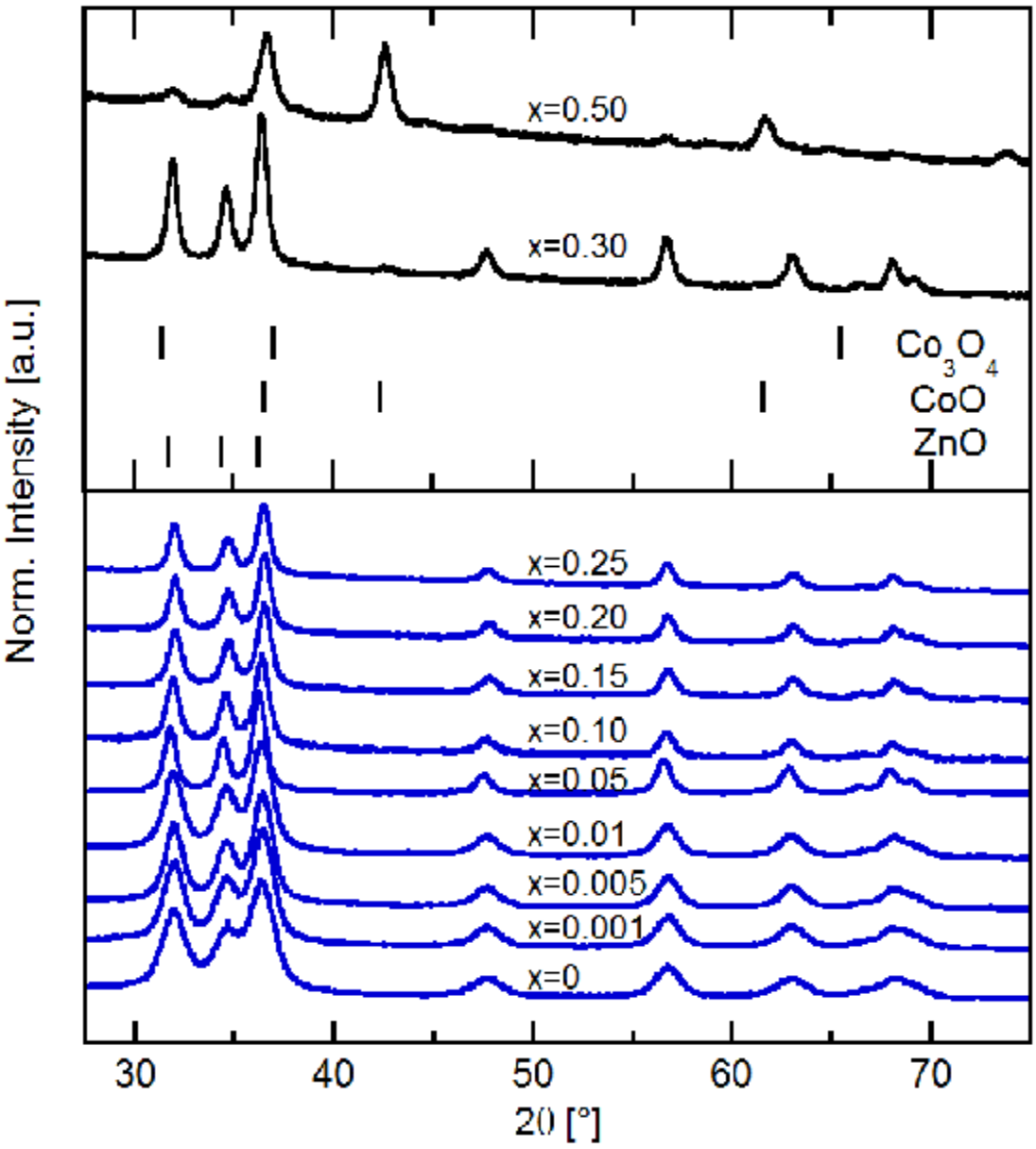

Figure 4. 3. XRD patterns of as-synthesized $Zn_{1-x}Co_xO$ nanoparticles (vertical bars are three most pronounced Bragg reflections for wutrtzite ZnO, CoO and Co_3O_4).

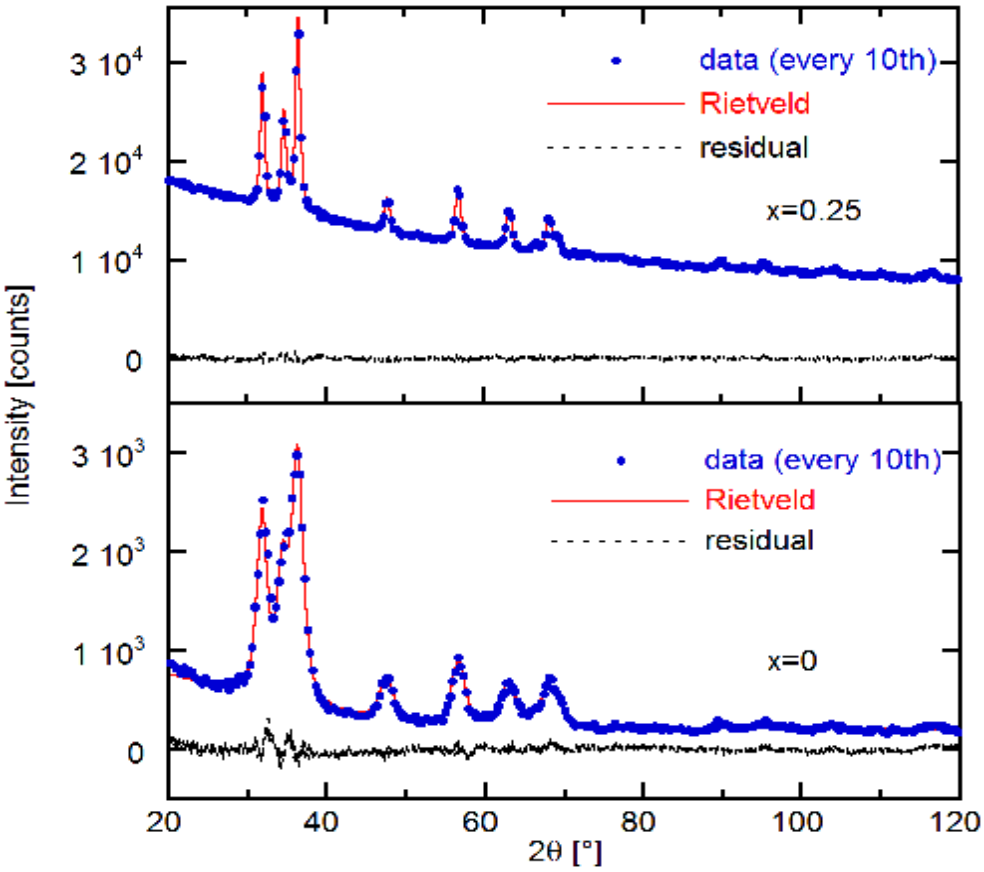

Figure 4.4. Rietveld refinements of the patterns for samples with Co content of $x = 0$ and $x = 0.25$.

The maximum Cobalt solubility in the wurtzite ZnO, for which the particles are still single-phase, varies greatly for samples of the same nominal composition but prepared by different methods (Duan 2008, Jayaram 1999, Risbud 2003, Kolesnik 2004, Schaedler 2006). Recently, Straumal et al. found that the solubility of Co and Mn increases with decreasing the grain size (Straumal 2004, Straumal 2009). They show that decreasing the grain size increases the solubility of Co in ZnO from 2 at. % in the bulk and up to about 40 at. % in polycrystalline samples with the grain size below 20 nm. The Co solubility limit in our particles is about $x_a = 0.33$ ($x = 0.25$), Fig. 4.3. In our system, the particle size ranges from about 9 nm for undoped samples (Fig. 4a) up to 20 nm for the sample with Co content of $x = 0.25$. Further Co addition causes the generation of second phases: CoO in the sample with nominal Co content of $x = 0.30$ ($x_a = 0.332$) and CoO and Co_3O_4 in the sample with $x = 0.50$ ($x_a = 0.56$).

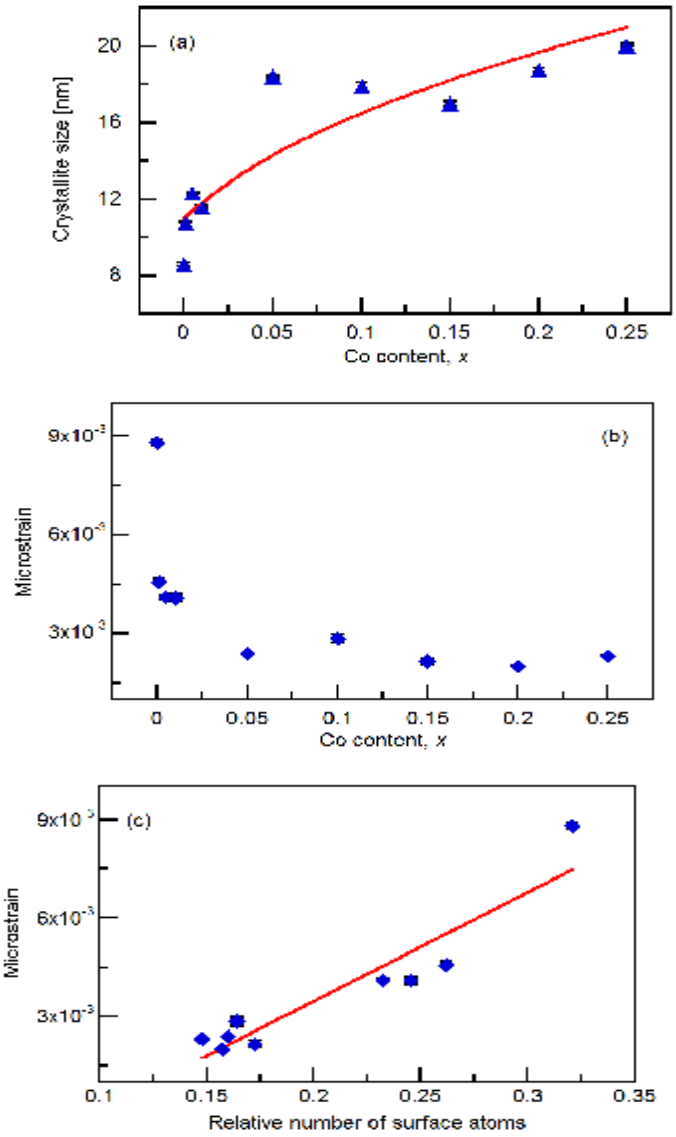

Figure 4. 5. (a) Crystallite size fit according to monodisperse coagulation and (b) microstrain as a function of actual Co content in $Zn_{1-x}Co_xO$ samples and (c) as a function of the relative number of atoms on the particle surface .

This is consistent with the finding of Straumal et al. The incorporation of Co ions into the wurtzite structure leads not only to a decreasing crystallite size (coherent diffracting domain size d) but also to a decrease of the microstrain, Fig. 4.5 (b). The origin for the increase in crystallite size with increasing Co content is opposite to other doping elements such as Chromium or Aluminum (Brehm 2006 and Jin 2007) where impurity drag is slowing down particle growth by coalescence. One

possible explanation for the increasing crystallite size is the increasing evaporation rate with increasing Co content in the precursor mixture (Fig. 4.5). The decrease in microstrain is probably due to the increasing surface to volume ratio with decreasing crystallite size as it correlates with the crystallite size. Since the valence of Co and Zn in Co doped ZnO is identical and the ionic radius for both is similar the microstrain is varying little above Co contents of $x = 0.05$ as is the crystallite size. These observations are consistent with the large Co content above which only second phase formation is observed.

4.2. Structural Characterization: Long Range Order

A solid is crystalline if it has long-range order. Once the positions of an atom and its neighbours are known at one point, the place of each atom is known precisely throughout the crystal. Most liquids lack long-range order, although many have short-range order. Short range is defined as the first- or second-nearest neighbours of an atom.Up to $x_{Co} = 0.05$ the X-ray diffractograms could be refined using a single wurtzite phase (Fig. 4.3). The lattice parameters of $Zn_{1-x}Co_xO$ wurtzite obtained from Rietveld refinements are presented in Fig. 4.6. It is found that Co substitution causes an elongation along the *a*-axis, while no significant change for the *c*-axis is observed. As a result also the unit-cell volume increases and the c/a ratio decreases. A similar behavior is reported by Kolesnik et al. (Kolesnik 2004). Considering that the ionic radius of tetrahedrally coordinated Co^{2+} (0.58 Å) is only slightly smaller than Zn^{2+} (0.60 Å) (Shannon, 1976), no change in *c*- or *a*-direction are expected. Jin et al. report similar observation concerning the *c*-axis in Co-doped films (Jin, 2001). The elongation along the *a*-axis up to $x = 0.005$ is possibly result of lattice relaxation (Woltersdorf, 1981) due to a crystallite size effect (Fig. 4.5(a)). For higher Co contents the increase in the unit cell volume and the decrease in the c/a ratio is less steep and can no longer be size related as the crystallite size remains constant but is obviously due to the incorporation of Co into the wurtzite lattice. Above $x = 0.25$ a rocksalt phase is observed. The c/a ratio is decreasing below 1.6 at $x = 0.25$ (Fig. 4.7) for which also the transition from wurtzite to rocksalt occurs with increasing pressure

at 9 GPa in case of pure ZnO (Desgreniers, 1998). However, with increasing pressure, the unit cell volume decreases opposite to our observation (Fig. 4.6).

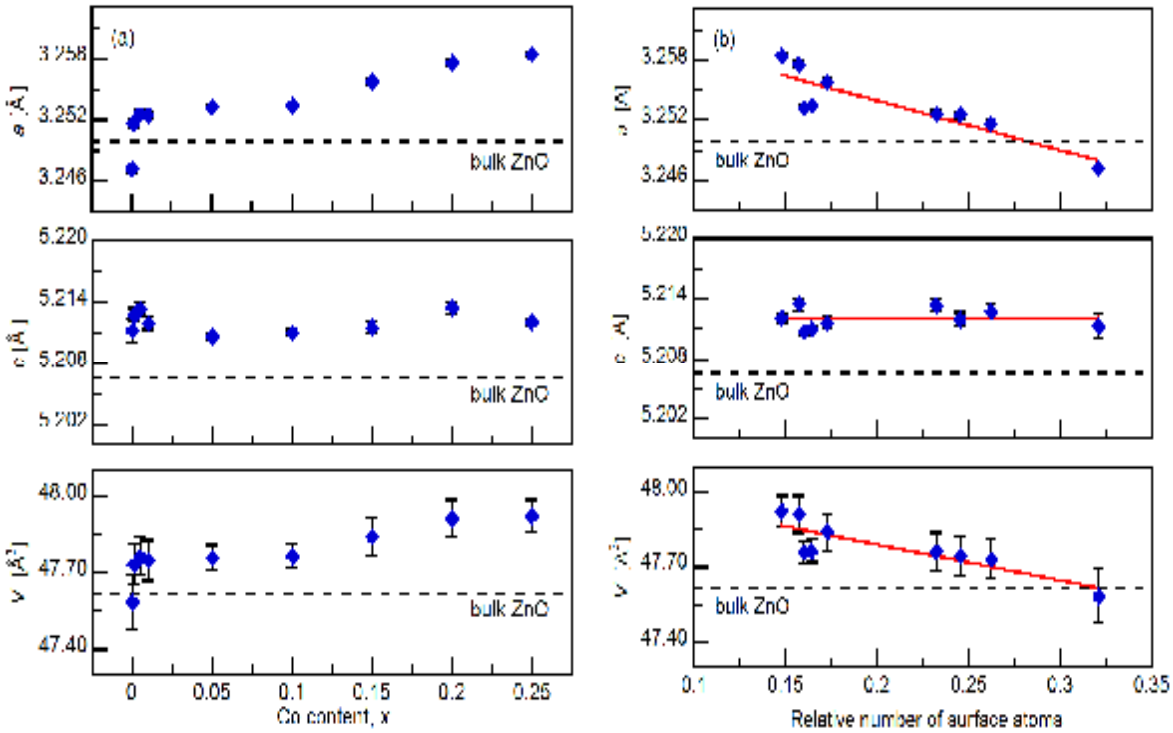

Figure 4.6. (a) Lattice parameters *a* and *c* and unit-cell volume of the $Zn_{1-x}Co_xO$ samples (bulk values for ZnO are literature data) as a function of Co content and (b) relative number of surface atoms

The oxygen positional parameter in *c*-direction, *u*, describes the relative position of the anion to the cation sublattice in wurtzite (Desgreniers, 1998) and *u*c/a* for an ideal wurtzite lattice would be 3/8 (Kisi 1989) which is observed for pure ZnO nanocrystals close to the bulk value (Fig. 4.7).

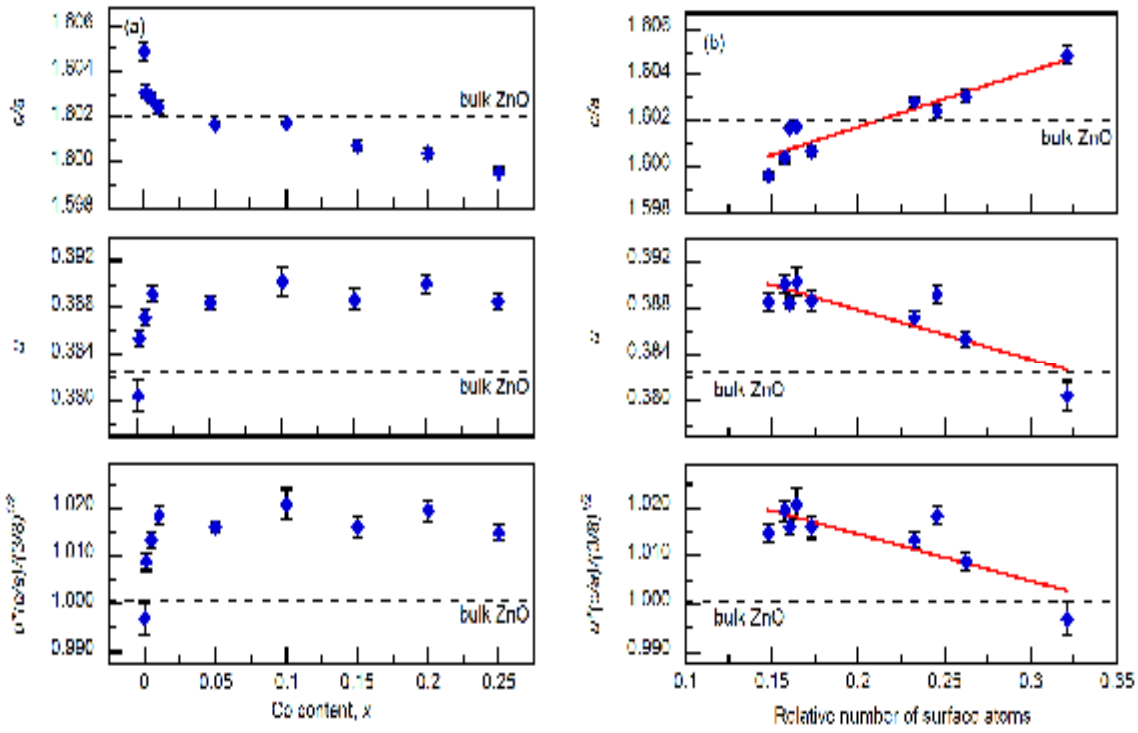

Figure 4.7. (a) Structural parameters determined from Rietveld refinement as a function of Co content and (b) as a function of relative number of surface atoms

For Co contents above x = 0.005 the only structural parameter which is significantly changing is the lattice constant a and correspondingly the unit cell volume and the c/a ratio. These samples have all a relatively large crystallite size of about 18 nm and a low microstrain (Fig. 4.5). Therefore, the variation in the lattice constant a must be due to the incorporation of Co into the wurtzite lattice and not a size effect but is probably an electronic effect of the $3d^7$ ion Co^{2+}.

4.3. Structural Characterization: Local Structure

Element specific X-ray absorption spectroscopy can provide information about the distribution and location of Co in the wurtzite lattice complementary to X-ray diffraction which is not sensitive to segregation or the formation of small precipitates of second phases. Therefore, samples for which XRD data showed only single wurtzite phase, $x \leq 0.25$ have also been studied by XAFS. Figure 4.8 shows

normalized Co and Zn *K*-edge XANES spectra of the $Zn_{1-x}Co_xO$ together with reference spectra of Co metal, CoO, and Co_3O_4, and theoretical XANES spectra for Co-doped ZnO. The EXAFS data are also analyzed using ARTEMIS and FEFF8 programme. ARTEMIS is a program for analyzing EXAFS data and uses chi(k) as it‘s input. FEFF8 is used as external program to calculate basic spectra for XANES fitting. ARTEMIS works within the framework of FEFF’s multiple-scattering path expansion (Zabinsky et al., 1995; Rehr & Albers, 1990).This means that the data are described as a summation of one or more scattering paths as computed by FEFF. FEFF8 is self-consistent real space multiple-scattering code for simultaneous calculations of x-ray absorption spectra and electronic structure. Output includes extended x-ray absorption fine structure (EXAFS), full multiple scattering calculations of various x-ray absorption spectra (XAS) and projected local densities of states (LDOS).

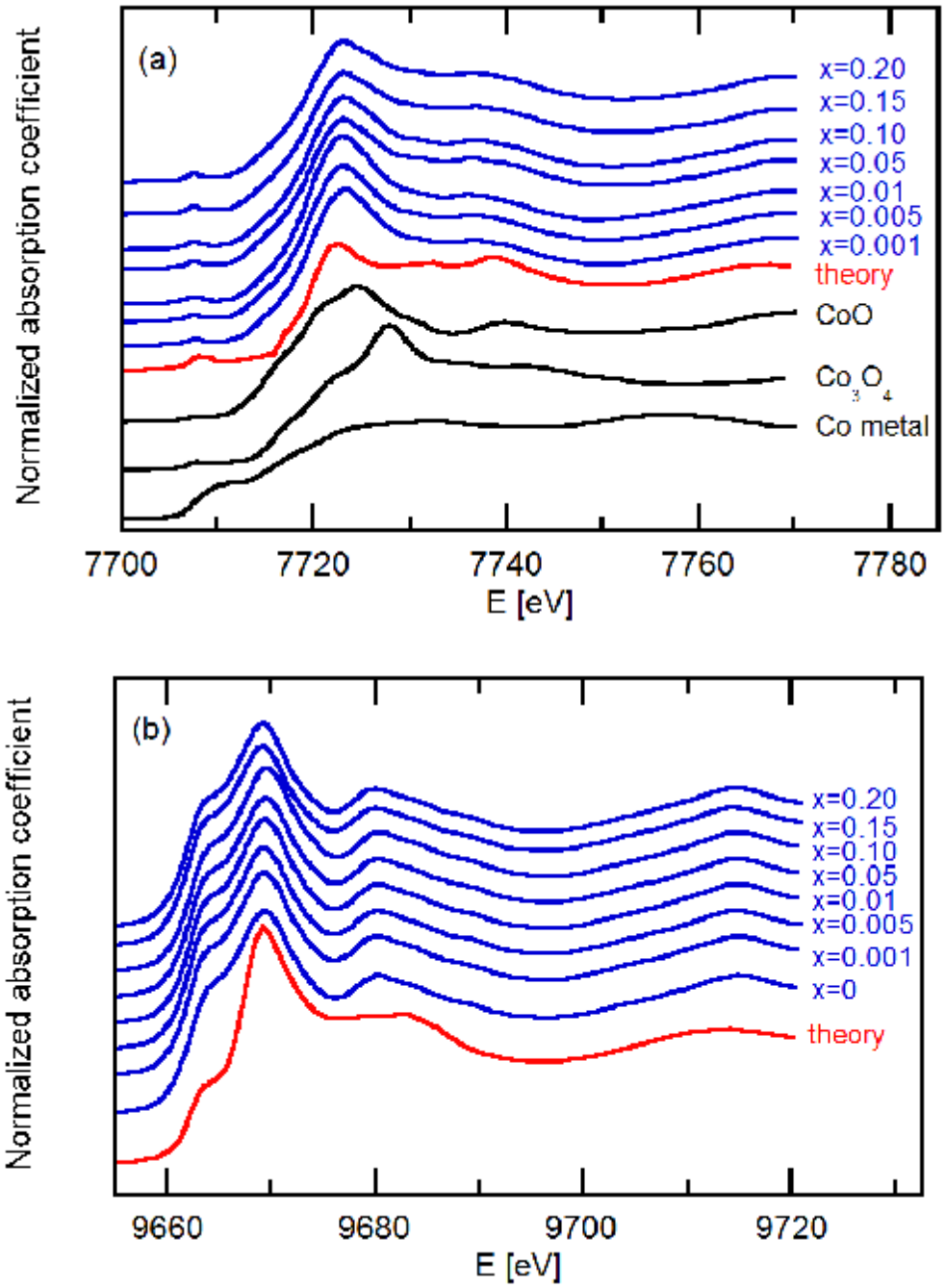

Figure 4.8. (a) Co *K*-edge XANES spectra of $Zn_{1-x}Co_xO$, CoO, Co_3O_4, Co metal and theoretical calculation for Co-doped ZnO and (b) Zn *K*-edge XANES spectra for $Zn_{1-x}Co_xO$ and theoretical calculation for Co-doped ZnO.

Full multiple scattering simulations using FEFF 8 (Newville,2000) are used to compute theoretical XANES spectra. Comparing the XANES spectra of Zn_{1-}

$_xCo_xO$ with the spectra of the CoO reference, reveals that the Co is present in the Co^{2+} valence state. The existence of Co metal and cobalt oxides can be excluded using fingerprint methods due to the different spectral features of $Zn_{1-x}Co_xO$ as compared with that of cobalt oxides. The small pre-edge peak at about 7708 eV appears due to the transition of Co 1*s* electron to 4*p*-3*d* hybridized states in tetrahedral symmetry (Sun 2008). The shoulder above the absorption edge in the Zn-K-edge XANES spectra at 9680 eV (Fig. 4.8(b)) is related to the 'solid-state effect' due to scattering contribution of high coordination shells (Liu 2008). The XANES simulations for Co replacing Zn substitutionally in the wurtzite lattice are in very good agreement with the experimental spectra.

It is difficult to detect the local structure at Co atoms in a ZnO lattice using EXAFS because the atomic numbers differ little (Z = 27 for Co and Z = 30 for Zn). However, the agreement factor worsens significantly for the Co spectrum when the Co amplitude and phase functions are replaced by their Zn counterparts. Additionally, in Co-doped ZnO samples Co-Co distances decrease with increasing Co contents whereas the coordination number of Co-Co pairs increases. These values differ significantly from CoO and Co_3O_4. Therefore, information about the local structure of Co in ZnO can be extracted by data analysis from the experimental EXAFS spectra.

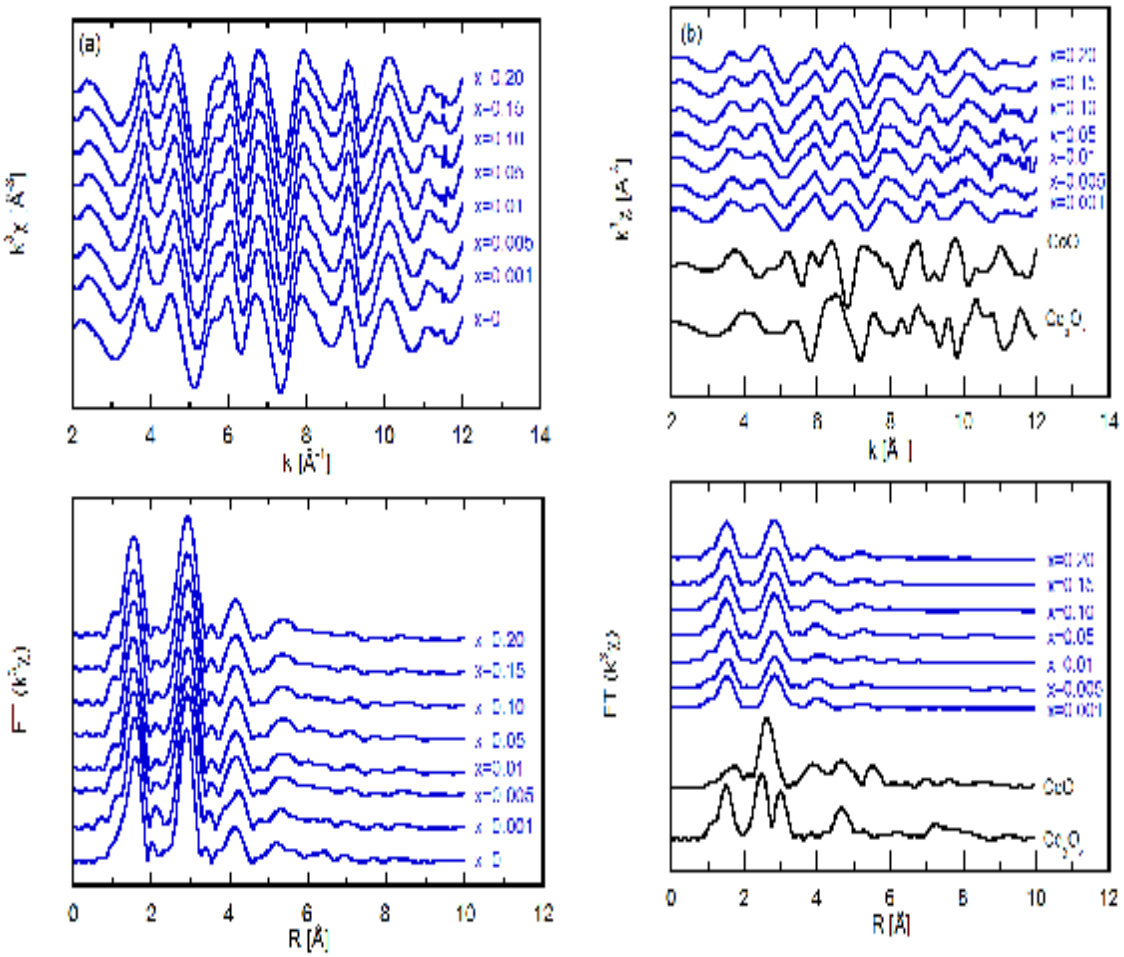

Figure 4.9. EXAFS spectra (top) and radial structure functions (bottom) on Zn *K*-edge (a) and Co *K*-edge (b) for $Zn_{1-x}Co_xO$.

The Co *K*-edge EXAFS for $Zn_{1-x}Co_xO$, and the Zn *K*-edge for ZnO powder, as well as their Fourier transforms are shown in fig. 4.9 (a) and (b), respectively and the Zn *K*-edge EXAFS for $Zn_{1-x}Co_xO$, and the Zn *K*-edge for ZnO powder, as well as their Fourier transforms are shown in Fig. 4.9(c) and (d) respectively. From Fig. 4.9 (a)it can be seen that the spectra as well as the amplitude of the Fourier transforms for $Zn_{1-x}Co_xO$ are very close to that of pure ZnO indicating that Co is replacing Zn substitutionally. From the radial structure functions (no phase shift correction applied) of ZnO and $Zn_{1-x}Co_xO$ (Fig. 4.9(b))three peaks can be observed. The first peak at about 1.6 Å is due to the Co-O coordination in the first shell, the second peak at about 2.5 Å corresponds to the Zn(Co)-Zn coordination in the second shell, and the third at about 4 Å arises from the third coordination shell comprising of nine

oxygen atoms and multiple scattering. Positions and amplitude of the first and second peaks do not change significantly with increasing Co content.

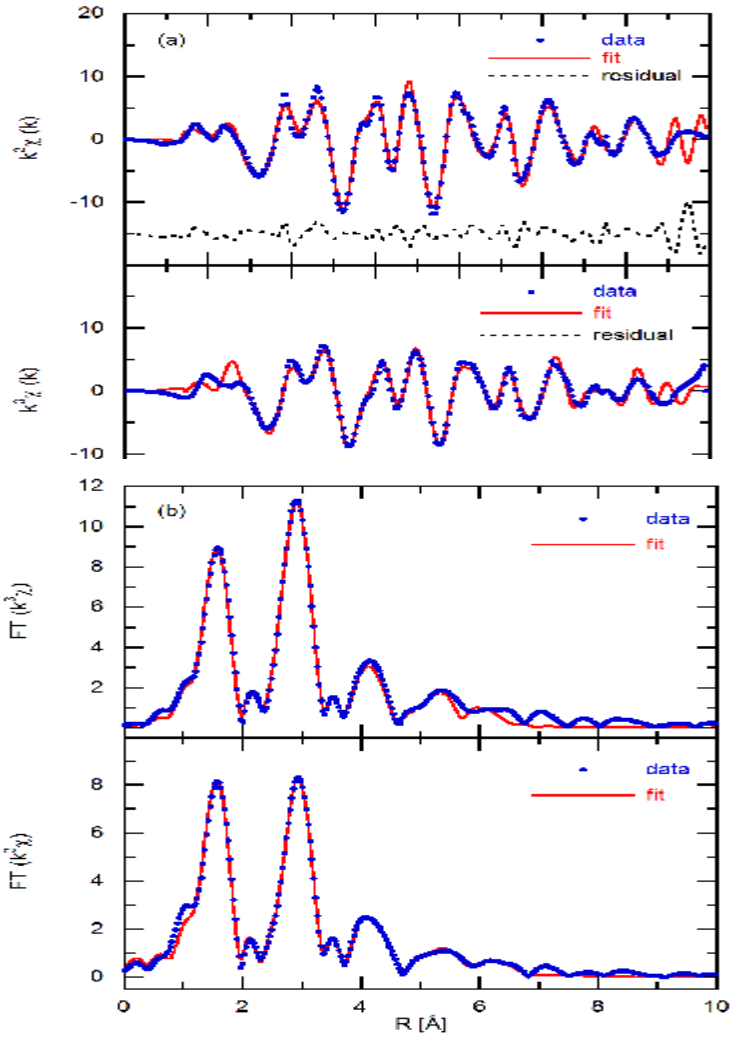

Figure 4.10. (a) ARTEMIS fit of the Zn- (top) and Co *K*-edge EXAFS spectra (bottom) of $Zn_{0.85}Co_{0.15}O$ and (b) corresponding radial structure functions

The first four peaks are fitted for all samples using ARTEMIS including multiple scattering (see Fig. 4.10 for $Zn_{0.85}Co_{0.15}O$). The results are in good agreement with the experimental data up to about 6 Å. Data in the k = 3-12 $Å^{-1}$ range was fourier transformed, and fitted in real space in the R =1-6.6 Å range for best fitting at $Zn_{0.85}Co_{0.15}O$ nano-composite using a Hanning window function in ARTEMIS. The ARTEMIS option for simultaneous fits with all three k weightings 1, 2, and 3 was used.

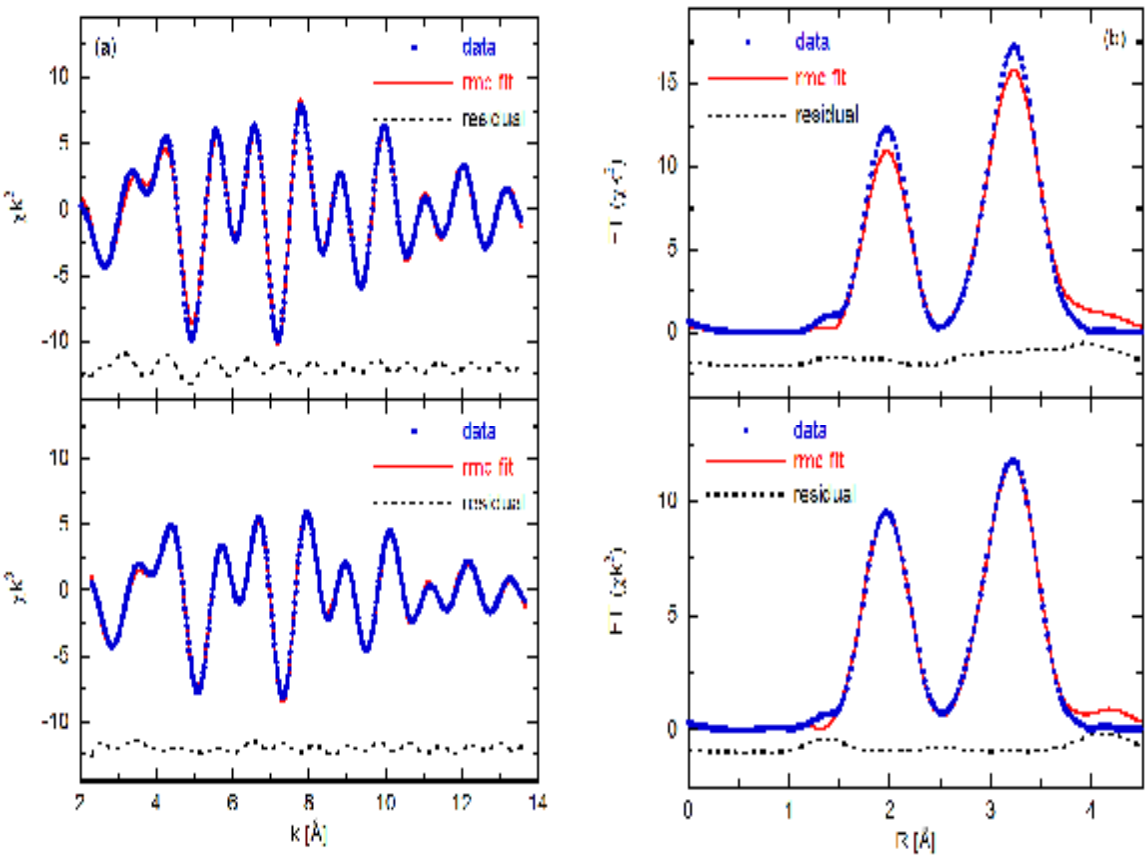

Figure 4.11. RMC analysis of EXAFS spectra of $Zn_{0.80}Co_{0.20}O$ using a single, mutual model for(a) Zn *K*-edge (top) and Co *K*-edge spectra (bottom) and (b)their phase corrected radial structure functions.

Samples with x > 0.005 are also analyzed using RMC (Fig. 4.11) again in good agreement with the experimental data. Partial pair distribution functions derived from RMC analysis of the EXAFS spectra are shown in Fig. 4.12 for $Zn_{0.8}Co_{0.2}O$. The agreement between the two different, independent fitting

approaches is excellent. Only the Debye-Waller factors obtained from the ARTEMIS fits are systematically smaller compared to the second moments determined from RMC partial pair distribution functions. Since ARTEMIS uses a Gaussian distribution and the second moment is determined from numerical distributions, the deviation is likely to originate from the non-Gaussian shape of the distribution functions (Fig. 4.12).

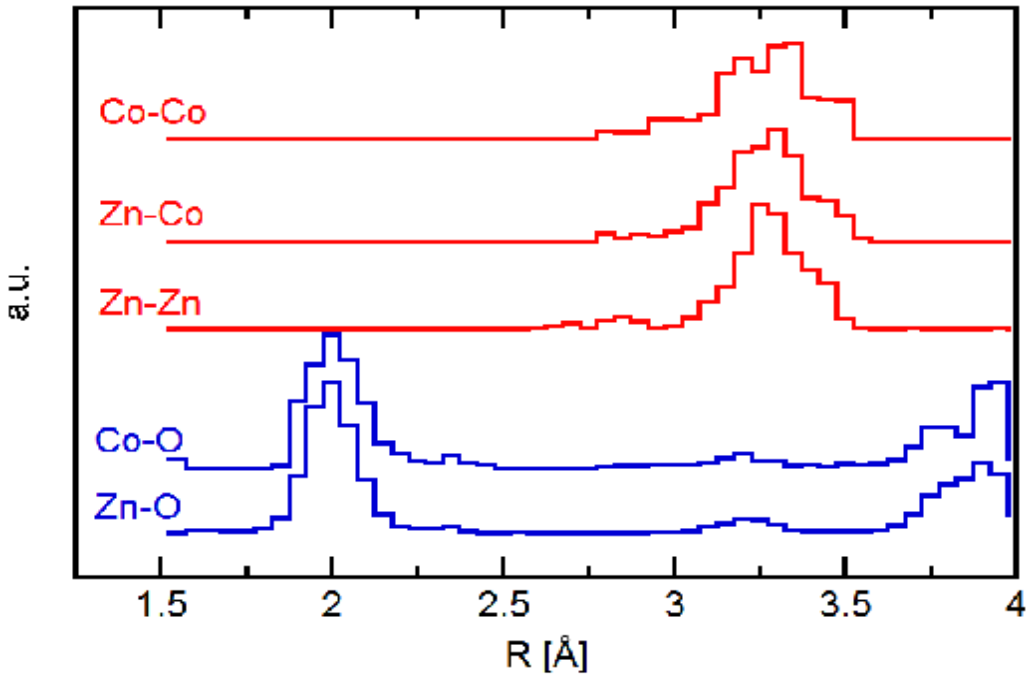

Figure 4.12. Partial pair distribution functions for $Zn_{0.80}Co_{0.20}O$ derived from RMC analysis of EXAFS data.

The first four peaks are fitted for all samples using ARTEMIS including multiple scattering (see Fig. 4.13,14,15,16,17,18 for x=0.1,0.5,1,5,10,20 for $Zn_{1-x}Co_xO$ respectively).The results of the ARTEMIS fits (interatomic distances, coordination numbers and Debye-Waller factors) and the RMC analysis (moment analysis of the partial pair distribution functions up to the second moment) are compiled and compared in Table 1 for all doped samples as well as pure ZnO and bulk reference samples (CoO and Co_3O_4).

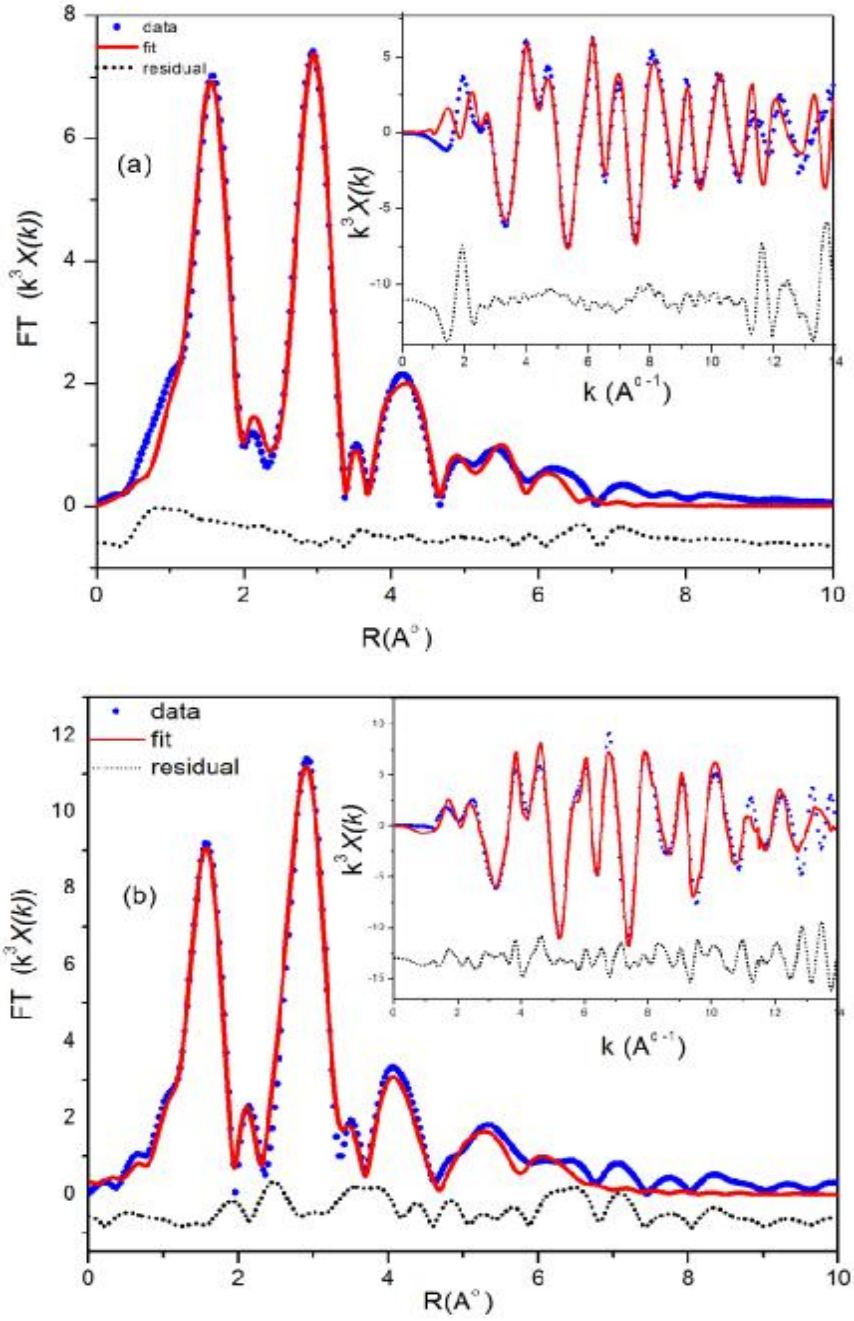

Figure 4.13. (a) ARTEMIS fit of the Co *K*-edge and (b) Zn *K*-edge radial structure functions of $Zn_{0.999}Co_{0.001}O$ and insets show EXAFS spectra .

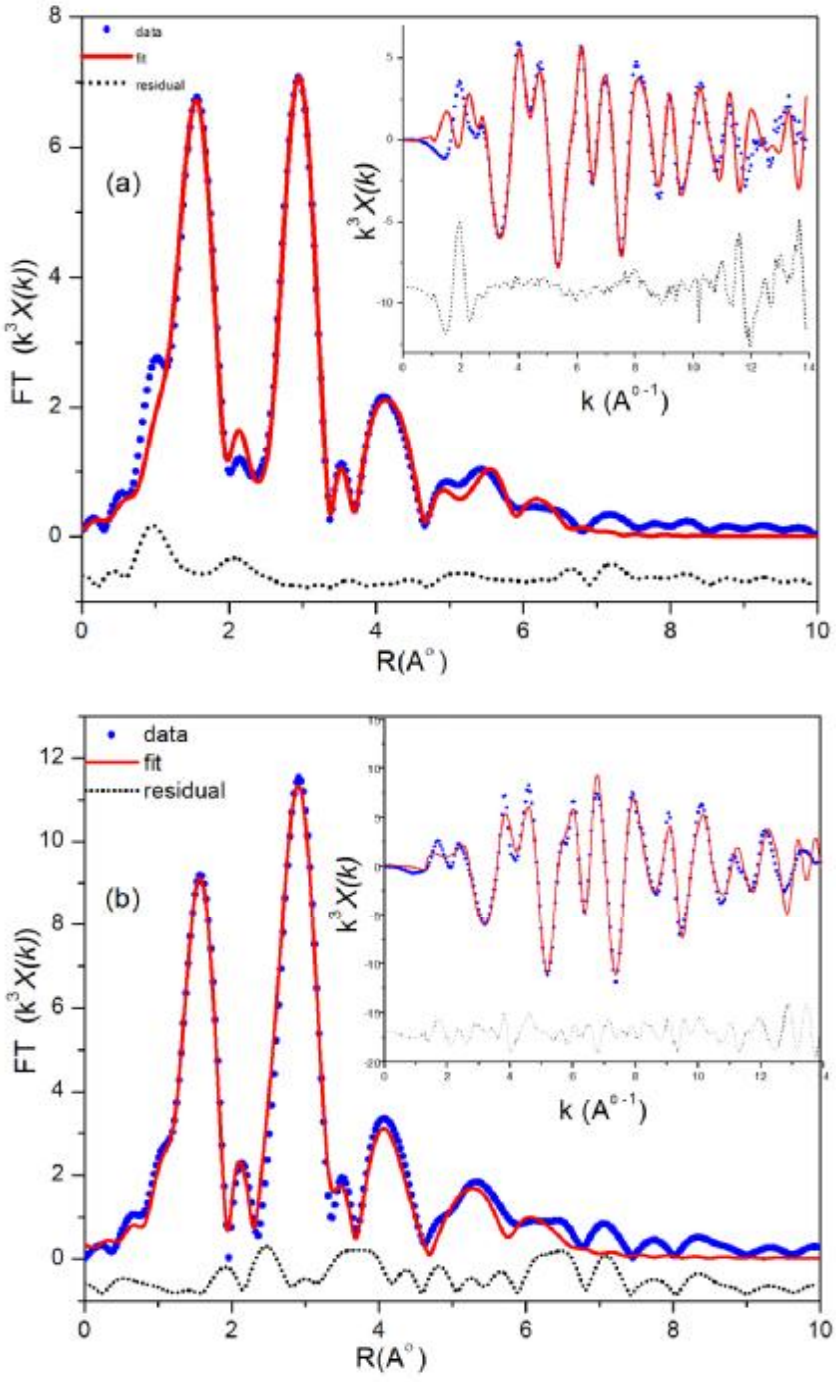

Figure 4.14. (a) ARTEMIS fit of the Co *K*-edge and (b) Zn *K*-edge radial structure functions of $Zn_{0.995}Co_{0.005}O$ and insets show EXAFS spectra .

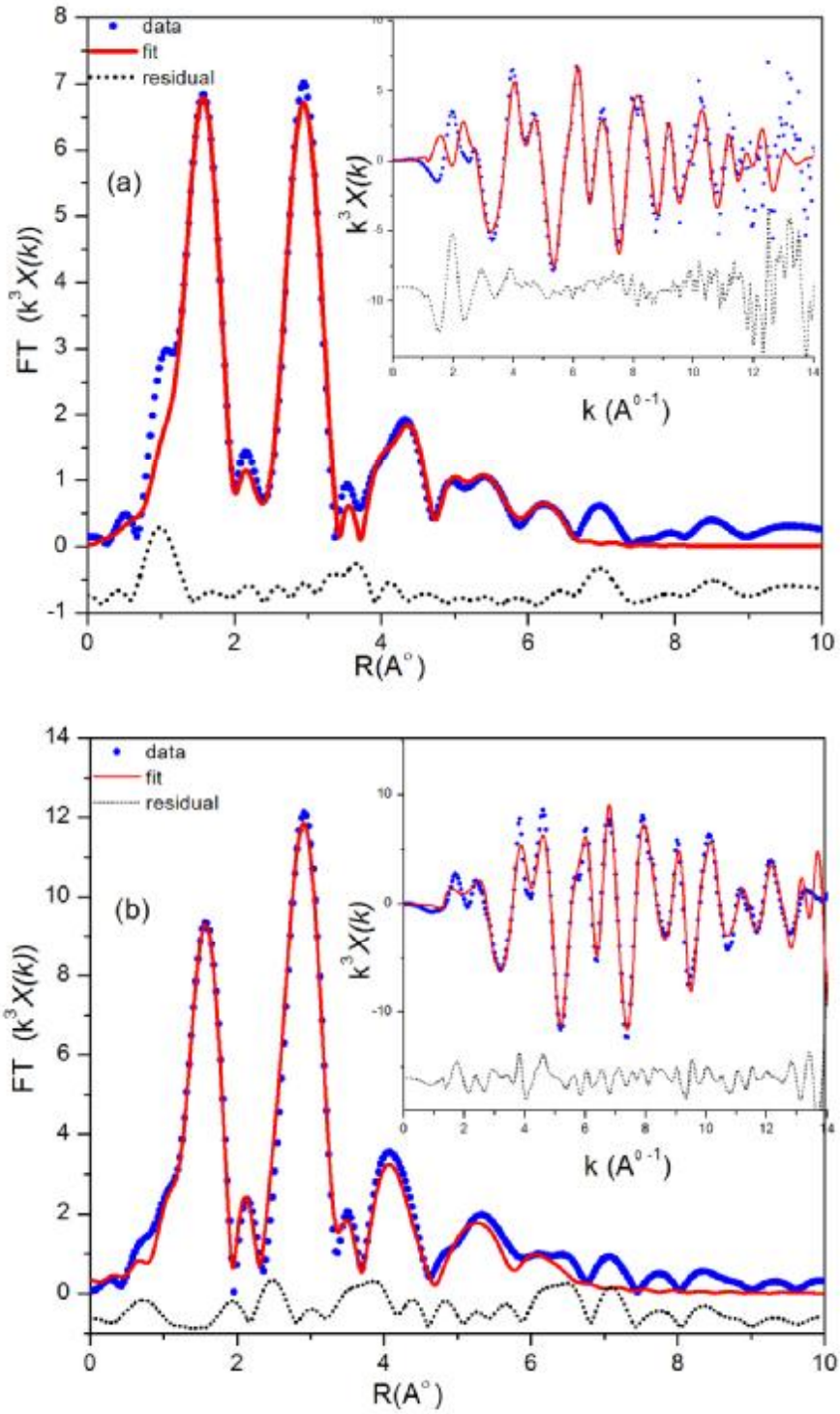

Figure 4.15. (a) ARTEMIS fit of the Co *K*-edge and(b) Zn *K*-edge radial structure functions of $Zn_{0.99}Co_{0.01}O$ and insets show EXAFS spectra .

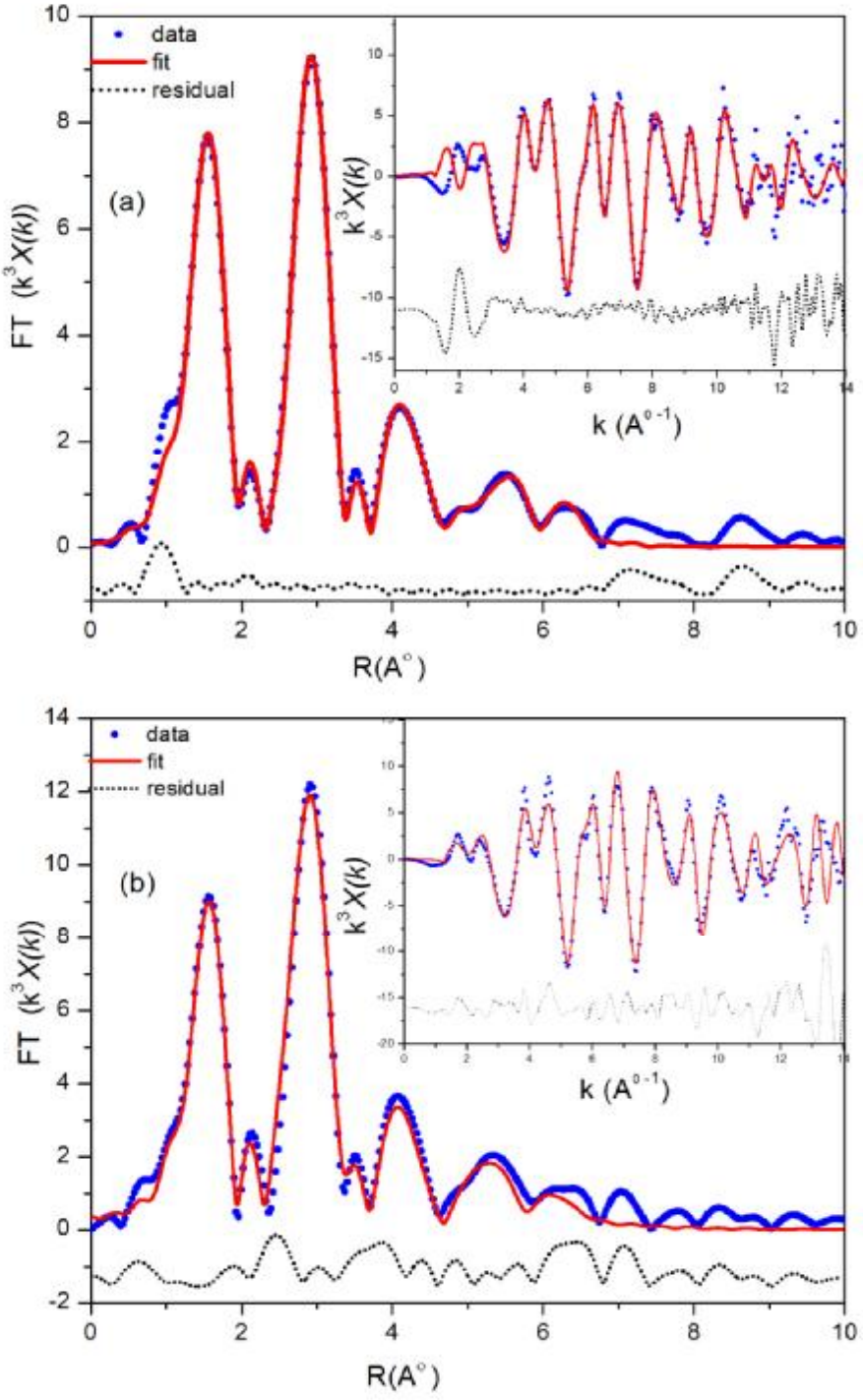

Figure 4.16. (a) ARTEMIS fit of the Co *K*-edge and (b) Zn *K*-edge radial structure functions of $Zn_{0.95}Co_{0.05}O$ and insets show EXAFS spectra .

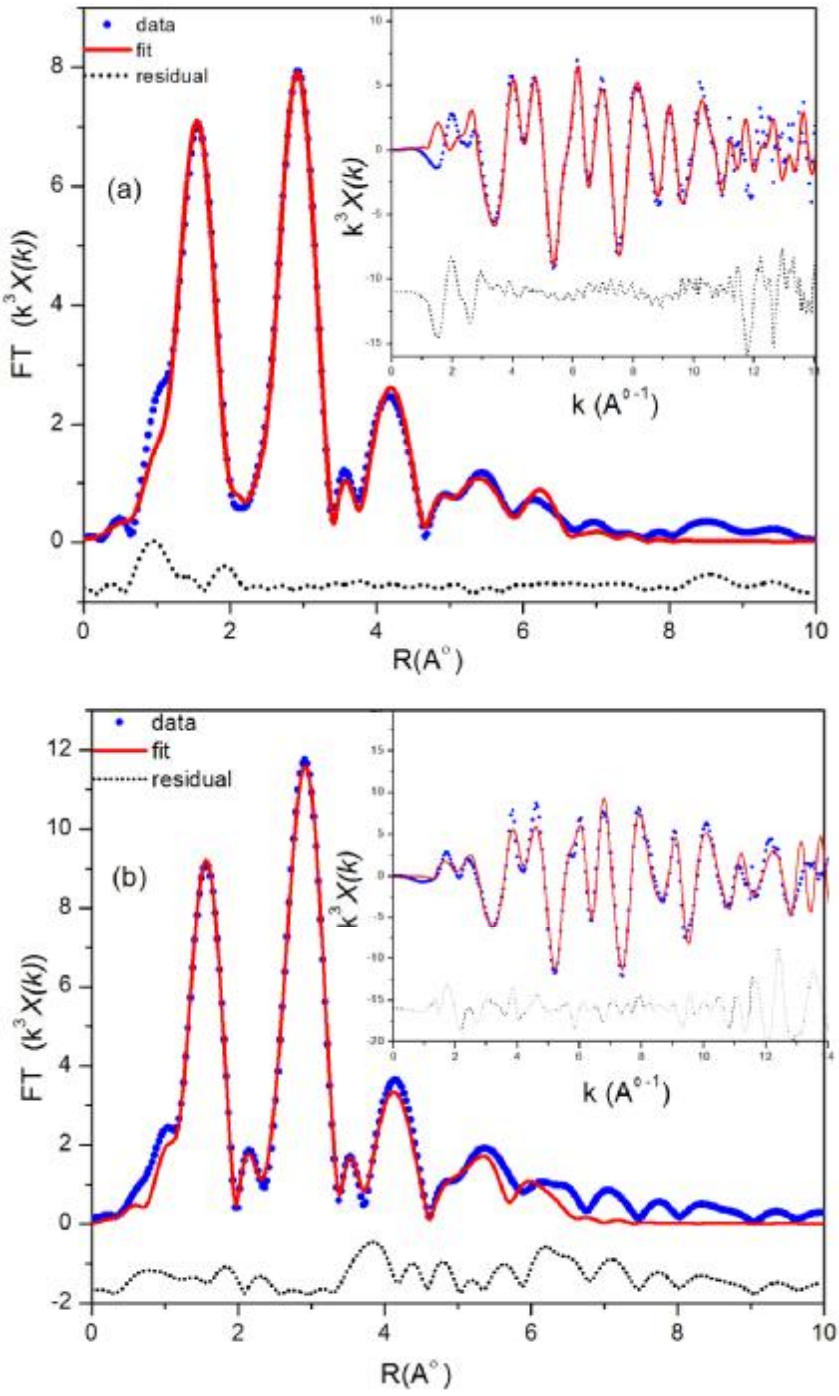

Figure 4.17. (a) ARTEMIS fit of the Co *K*-edge and (b) Zn *K*-edge radial structure functions of $Zn_{0.90}Co_{0.10}O$ and insets show EXAFS spectra .

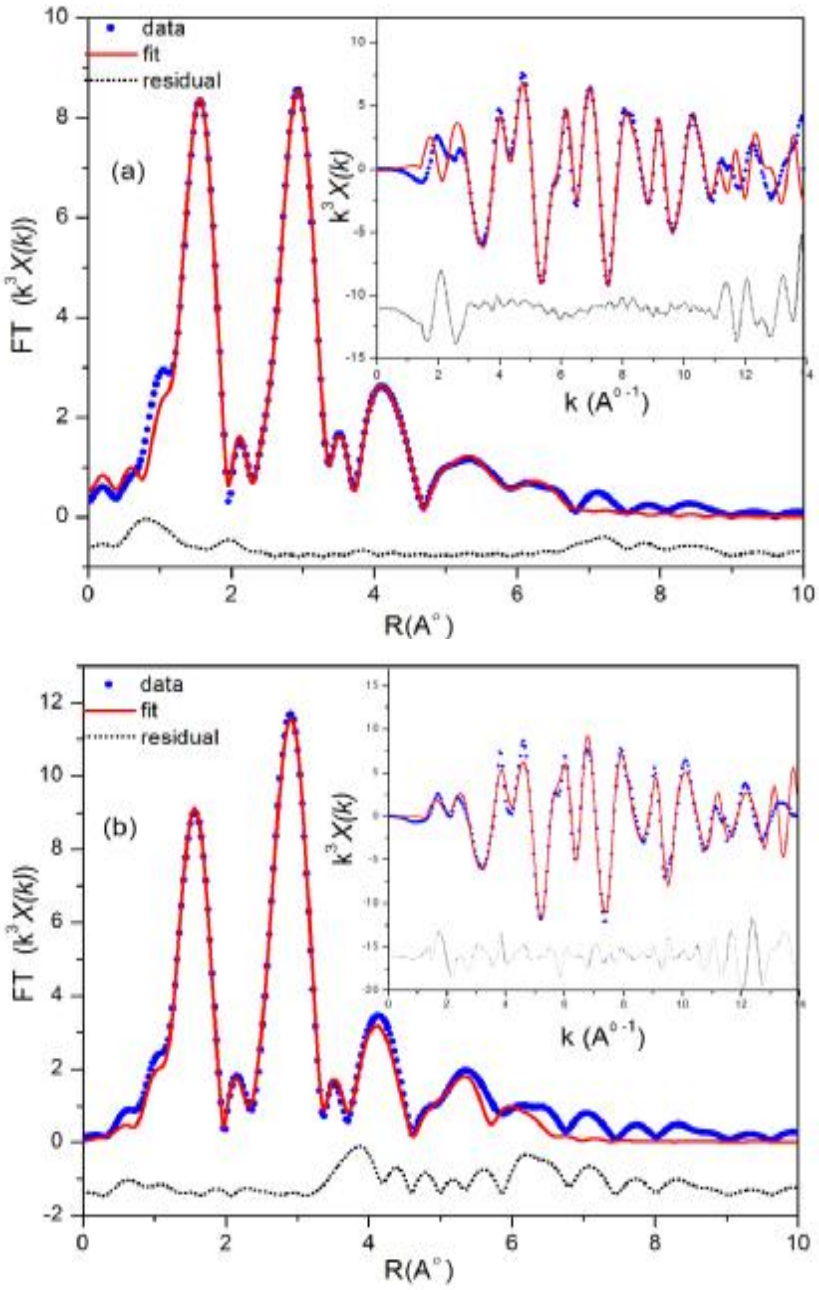

Figure 4.18. (a) ARTEMIS fit of the Co *K*-edge and(b) Zn *K*-edge radial structure functions of $Zn_{0.80}Co_{0.20}O$ and insets show EXAFS spectra .

Table 4.1. Results of EXAFS data analysis using ARTEMIS and RMCxas for Co-doped ZnO and Co oxides. na: *not analyzed* b:*values in the brackets are only from one bin in pair distribution function due to low Co content*

Method of Analysis **x (Co)**	**Shell**	**RMC N**	**ARTEMIS N**	**RMC R[Å]**	**ARTEMIS R[Å]**	**RMC** $\sigma^2[10^{-3}Å^2]$	**ARTEMIS** σ^2 $[10^{-3}Å^2]$
0 (ZnO)	Zn-O	3.6(7)	3.8(2)	1.96(2)	1.97(1)	7(2)	5.4(2)
	Zn-Zn	11(2)	11.4(2)	3.24(2)	3.22(1)	13(4)	11.3(1)
0.001	Co-O	na	4.3(1)	na	2.01(2)	na	9(1)
	Co-Zn		11.9(1)		3.22(2)		18(4)
	Co-Co		0.011(0)		3.21(0)		17(2)
	Zn-Co		0.011(2)		3.21(2)		9(1)
	Zn-Zn		11.4(2)		3.23(2)		9(1)
0.005	Co-O	na	4.27(1)	na	2.01(2)	na	10(2)
	Co-Zn		11.34(1)		3.22(2)		17(5)
	Co-Co		0.06(0)		3.21(0)		17(2)
	Zn-Co		0.06(0)		3.21(2)		11(2)
	Zn-Zn		11.9(1)		3.23(2)		11(3)
0.01	Co-O	3.9(6)	3.96(7)	2.02(2)	2.00(2)	10(3)	7(2)
	Co-Co	(0.06)	0.11(1)	(3.21)	3.21(2)	na	18(4)
	Co-Zn	na	11.3(1)	na	3.21(0)	na	18(1)
	Zn-O	3.2(7)	3.3(2)	1.95(2)	1.96(2)	7(3)	10(4)
	Zn-Co	0.12(2)	0.114(1)	3.23(2)	3.21(2)	19(5)	14(3)
	Zn-Zn	9(2)	11.3(2)	3.25(3)	3.23(4)	12(4)	14(3)
0.05	Co-O	4.0(9)	3.7(5)	2.00(3)	1.97(4)	9(5)	6(2)
	Co-Co	0.38(8)	0.6(2)	(3.25(3))	2.94(3)	14(3)	4(15)
	Co-Zn	na	10.5(2)	na	3.20(4)	na	12(10)
	Zn-O	4.0(8)	3.8(1)	1.98(2)	1.97(1)	9(5)	6(1)
	Zn-Co	0.7(1)	0.57(2)	3.23(3)	3.20(2)	13(4)	8(3)
	Zn-Zn	11(3)	10.8(2)	3.24(3)	3.23(4)	12(5)	8(3)
0.10	Co-O	4.0(6)	3.8(5)	2.03(2)	1.98(3)	14(5)	7(2)
	Co-Co	1.1(2)	1.1(1)	3.25(2)	2.93(3)	10(3)	8(7)
	Co-Zn	na	10.4(2)	na	3.20(5)	na	13(7)
	Zn-O	3.8(7)	3.9(1)	1.98(2)	1.97(2)	12(6)	6(1)
	Zn-Co	1.5(3)	1.2(1)	3.23(2)	3.10(3)	18(4)	6(5)
	Zn-Zn	10(2)	10.7(3)	3.23(2)	3.24(2)	11(3)	10(2)
0.15	Co-O	4.0(8)	3.7(5)	2.01(3)	1.97(4)	12(6)	7(2)
	Co-Co	2.1(5)	1.7(2)	3.23(3)	2.95(2)	16(5)	12(10)
	Co-Zn	na	9.5(2)	na	3.20(10)	na	12(7)
	Zn-O	4.0(8)	3.4(2)	1.98(2)	1.97(1)	9(5)	4(5)
	Zn-Co	2.0(4)	1.8(2)	3.24(3)	3.20(2)	17(6)	5(7)
	Zn-Zn	10(2)	9.7(4)	3.22(3)	3.24(2)	19(9)	6(2)
0.20	Co-O	4.0(8)	3.73(5)	2.01(3)	1.97(4)	12(6)	6(2)
	Co-Co	2.6(5)	2.24(1)	3.22(3)	2.95(2)	24(8)	12(10)
	Co-Zn	na	8.9(3)	na	3.20(10)	na	14(10)
	Zn-O	4.0(8)	3.6(2)	1.98(2)	1.97(1)	9(5)	5(2)
	Zn-Co	2.6(6)	2.37(2)	3.24(3)	3.20(2)	19(8)	4(10)
	Zn-Zn	9(2)	9.5(4)	3.23(3)	3.25(3)	24(12)	10(3)
1.00 (CoO)	Co-O	5.8(8)	5.7(5)	2.10(3)	2.1(3)	46(10)	20(5)
	Co-Co	11(2)	11.4(3)	3.04(3)	3.02(3)	26(7)	13(7)
1.00 (Co_3O_4)	Co-O	5.0(8)	3.5(4)	1.96(2)	1.96(2)	20(8)	3.3(10)
	Co-Co	5(1)	10(2)	2.88(2)	3.4(2)	10(3)	10(3)

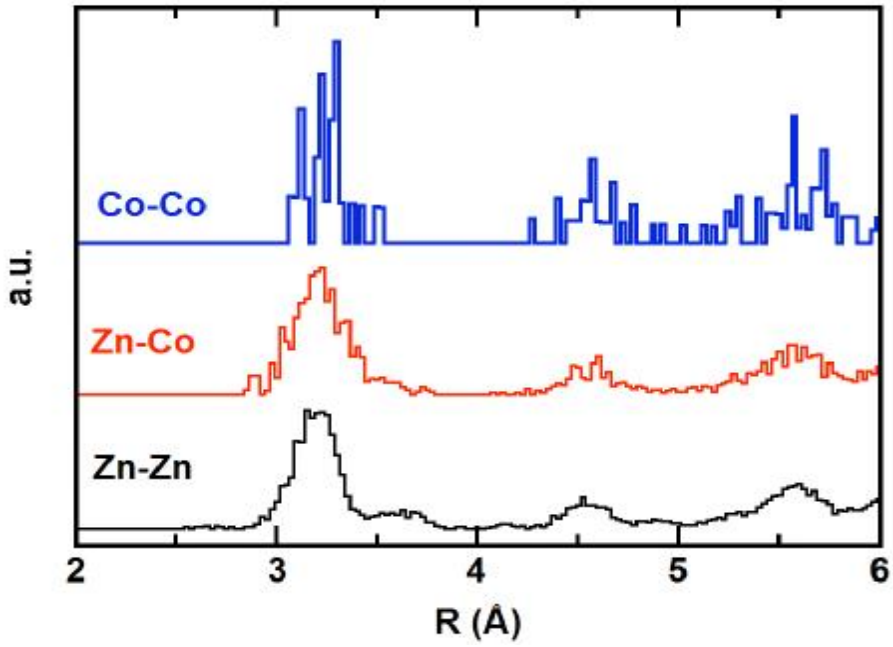

Figure 4.19. Partial pair distribution functions for $Zn_{0.90}Co_{0.10}O$ derived from RMC analysis of EXAFS data.

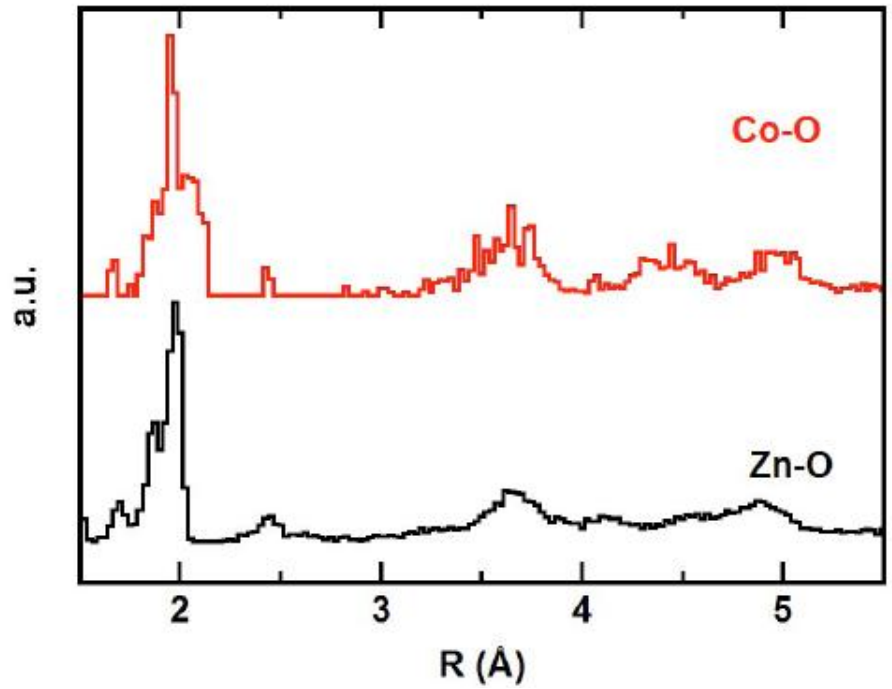

Figure 4.20. Cation-Oxygen pair distribution for Co doped ZnO

Figure 4.21 shows a typical TEM image of only ZnO (a) and the 1% and 10%Co doped ZnO (b) and (c) nanocrystal prepared by CVS method respectively. In

this figure Co concentration varied at different sampling points. Thereby, from TEM we measure particle size and if we can measure size more than 100 particles than one can get information about particle size distribution by fitting the data (particle size) using log-normal distribution

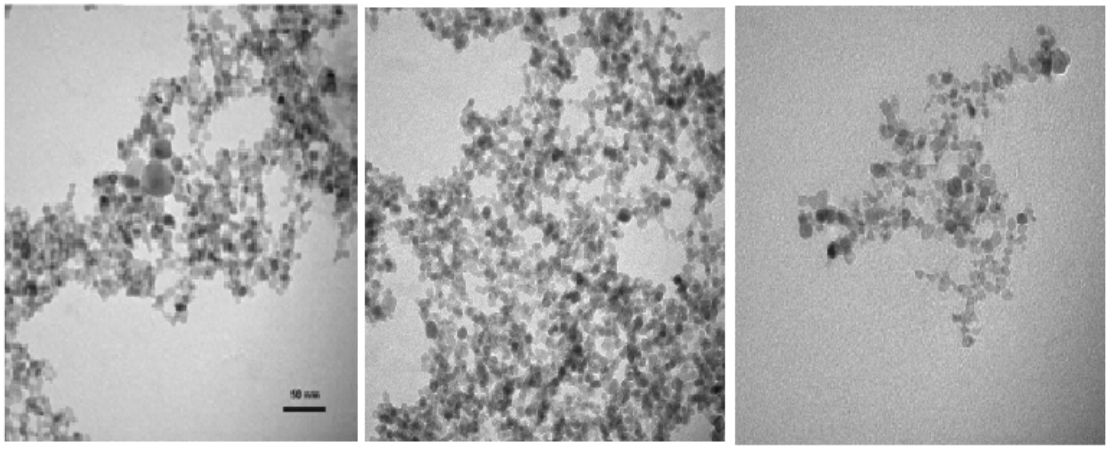

Figure 4.21. TEM images for Co doped ZnO (a) Only ZnO (b)1%Co and (c) 10% Co

In the Table 1 it can be seen that the interatomic distances of Co-O and Co-Zn in Co-doped ZnO samples are close to the Zn-O and Zn-Zn distances in pure ZnO. The partial pair distribution function for Co-Co, Co-Zn and Zn-Zn overlap and are not split. This shows that Co^{2+} ions occupy Zn sites in the ZnO wurtzite structure for doping levels *x* below 0.25. The Co doping cyrstal structure is also simulated in Figure 4.22.

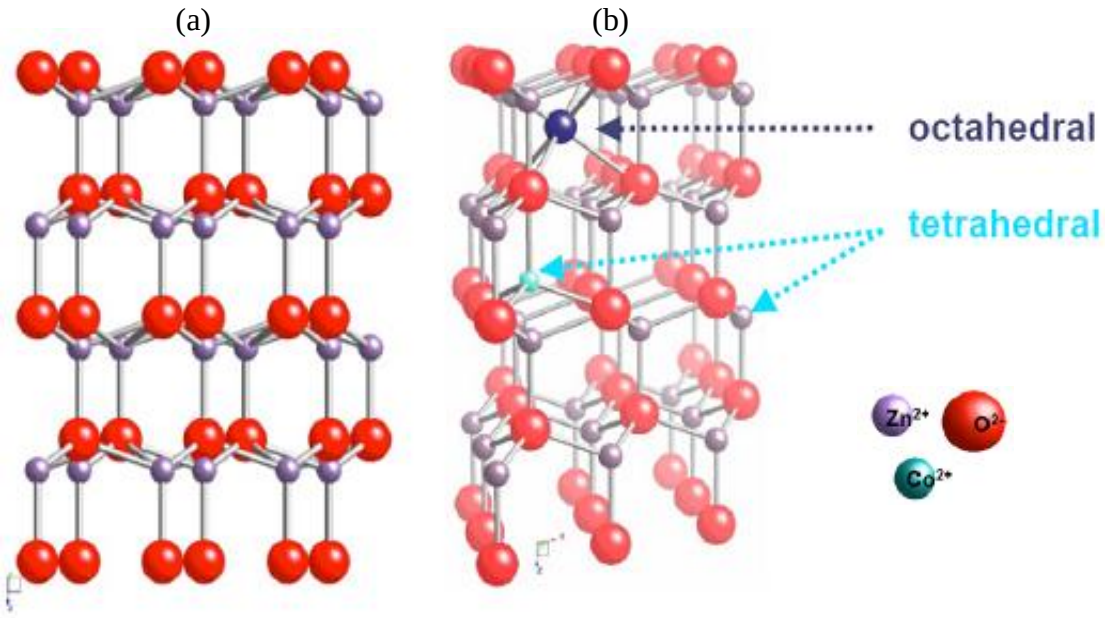

Figure 4.22.(a) Wurtzite structure (b) Co doping crystal structure in ZnO nanostructure

Figure 4.23 displays the interatomic distances as a function of Co content as determined from the RMC analysis together with the second moment. The Co-O distances deviate systematically to marginally larger distances compared to Zn-O distances whereas the cationic distances overlap within the error bars. Both do not change as a function of Co content. Only the second moment increases slightly at higher Co contents which could an indication for a precursor state to the phase transformation to rock salt structure at even higher Co contents.

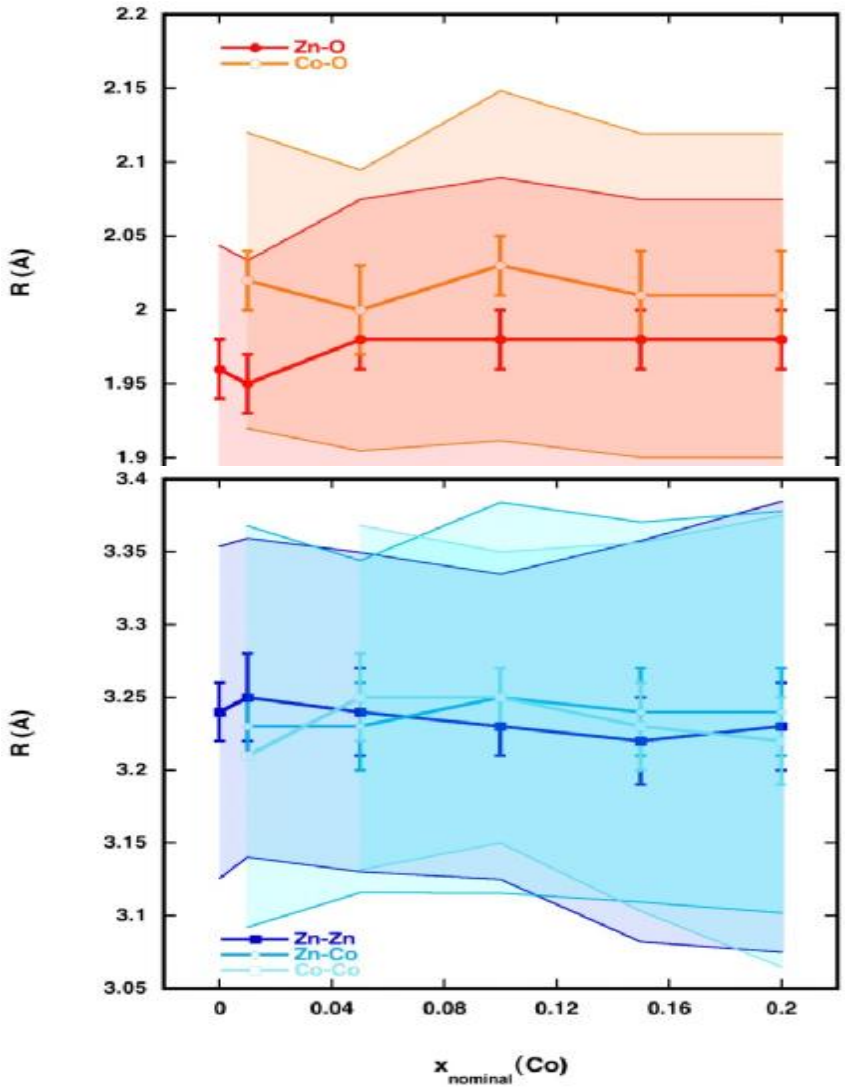

Figure 4.23. Displayed are the nearest and next nearest interatomic distances according to RMC data analysis as a function of cobalt content as determined from moment analysis of the corresponding partial pair distribution functions (taken from Table 1). The shaded areas represent the square root of the second moment (R +/- $(\sigma^2)^{1/2}$ [Å].

5. CONCLUSION AND DISCUSSION

Dilute ferromagnetism in semiconductors with Curie temperatures (*Tc*) above 300 K are materials of high technological interest due to their potential use in spin based electronic devices operable at room temperature. Additionally, the current technological trends towards device miniaturization are driving the development of materials research strongly in the direction of functional nanomaterials. Therefore, fabrication of well characterized nano dilute magnetic semiconductor systems is becoming increasingly important.

In this work, we have studied local structure of $Zn_{1-x}Co_xO$ nanoparticles (x=0.001-0.20), obtained by CVS method by using XRD and EXAFS method. In EXAFS method, all measurements for transmission and fluorescence was collected at room temperature. An example of the data quality achieved and the data analysis performed using by ARTEMIS programme and these datas was compared with the Reverse Monte Carlo Method (RMC) using the rmcxas program. Samples with $x \leq 0.20$ are also analyzed using RMC in good agreement with the using ARTEMIS. Also, for theoretical calculation we used real space multiple scattering method FEFF8 code and theoretical calculations for Cobalt doped ZnO support our measured ones. In contrast to reports in the literature our sample material shows a single phase behavior up to high Co concentrations(x=0.25). A combination of XAFS and EXAFS analysis shows also that the Oxygen defects play an insignificant role in these samples. It was fitted to different shells revealing pair correlations of the individual neighbors. These results, compared with XRD measurements, reveal the correlation between doping concentrations and non-isotropic strain in the nano particles.

As a conclusion, $Zn_{1-x}Co_xO$ nanoparticles for the Co contents of $x \leq 0.25$ are single phase. The crystallographic structure parameter varies continuously with increasing Co content probably due to a size rsp. surface effect for x below 0.005 and electronic effects originating from the 3d element for x above 0.005. At $x = 0.25$ the c/a ratio approaches values close to the wurtzite-rocksalt transition observed at high pressure in pure ZnO however at decreasing density. The XANES spectra are

consistent with Co replacing Zn substitutionally as is also shown by detailed analysis of the EXAFS spectra. The structural variations are very subtle for both the long range order as well as the local order up to $x \leq 0.25$. Therefore, from the structural point of view, $Zn_{1-x}Co_xO$ nanoparticles prepared by chemical vapor synthesis using laser flash evaporation as precursor delivery method is a good candidate for ferromagnetic semiconductor material.

In addition, it can be said that EXAFS method is a powerful technique to investigate the local structure around absorbing atom as the very low content samples.

Finally, structural and electronic investigations using EXAFS and XRD method will be helping to develop highly efficient electron emitters in the future.

6. FUTURE PROSPECTS

A Semiconductor doped with a transition metal (TM) is a good candidate to fabricate photo cathodes which is called electron emitters and highly efficient electron emitters are crucial components in devices such as hybrid solar cells, field emitters, and UV or X-ray photon detectors. Novel preparation methods utilizing nanoparticles are promising avenues to rationally design and generate films with high electron yield. This can be achieved by adjusting crystallographic orientation, morphology, microstructure, doping and composition to yield high photon absorption with low scattering losses, low work function, long-term mechanical, chemical and radiation stability under operating conditions. However, the large parameter space and the lack of fundamental knowledge on the correlation between properties and functionality is presently the main obstacle to use rational design rules in applications.

The work of this PhD thesis is part of an international collaboration focused on the rational design of ZnO, TiO_2, and HfO_2 based semiconductor photo cathodes. Moreover, the goal of this collaboration is to establish a feedback protocol facilitating optimization of the process parameters to produce the films, by performing electronic and structural characterization, and finally applying a basic understanding of electron yield and transport. In future, the final product will be used either in hybrid solar cells (partially supported by Degussa) or for high efficiency x-ray-electron photocathodes, e.g. x-ray streak cameras (timing program at APS). Wide angle x-ray scattering data and x-ray absorption fine structure data were taken and analyzed for various sample systems. It was focused on the traditional EXAFS- and XANES-analysis whereas the collaborators in Germany performed another analysis approach, using the reverse monte-carlo (RMC) method combining scattering and spectroscopy data. It uses structural and electronic properties derived from x-ray spectroscopy measurements to simulate the electric field distribution within the cathode and the electron trajectories through the material. The results of these simulations are used to predict optimized

morphologies and dopant concentrations resulting in design rules for nano materials with optimized functionality.

The final goal of the structural and electronic investigations is to correlate structural defects, strain, and doping with electronic properties which are investigated by the group of Prof. Bacher (University Duisburg-Essen/Germany) using luminescence measurements resolved in time and space in order to analyze the characteristic recombination times of photo-generated carrier decay times and Kelvin force probe microscopy for both local determination of the work function and the local distribution of the electrical potential.

On the basis of these first results combined with measurements of electronic properties, it was also performed initial simulations of the electric field distribution in various morphologies. Using a multi-physics simulation package (COMSOL) a model was developed which is presently being extended to integrate the electron trajectories. The features of COMSOL allow much flexibility so that charging and shielding effects, and even damage effects, as a function of the carrier density can be simulated. A first example is the pyramid structure formed by self-organization of TiO_2 nano-particles shown in figure 6.1. coated with a thin high dielectric media like HfO_2.The simulations can be performed for various geometries(cylindrical or aerogel) and dielectric constants simulating various doping concentrations.

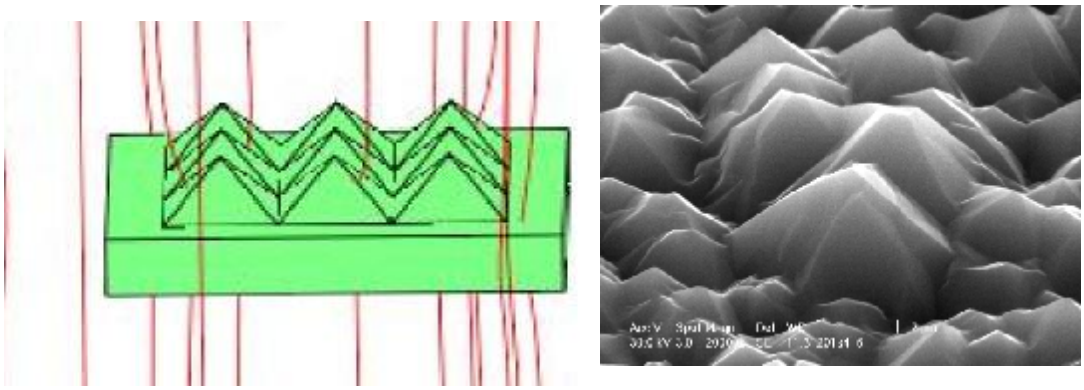

Figure 6.1.Simulation of the electric field distribution of a TiO_2 sample structure with a pyramid-like surface morphology and 1V potential difference from the surrounding environment. For a high dielectric constant the field is always perpendicular to the surface leading to a collimating effect of emitted electrons.

The model will be extended to include the effects of the electron current ejected by the cathode and to predict the electron energy and angle distribution. The investigation of various compound systems will be another focus of this subtask.

Characterization of the electron yield and electron distribution is the third aspect of me. Together with an engineer I developed a sample current total yield detector which will be finally combined with a hemispherical electron analyzer and fast multi-channel plate detector system. An overview drawing is shown in fig 6.2. This existing unit is ultra high vacuum UHV compatible and permits measurement of the sample total yield current. We use this quantity to characterize the overall efficiency of the cathode material. A first test of the unit showed excellent noise and background behavior. As a result we were able to measure currents down to the pA-range. The typical current measured at an APS bending magnet beamline is about 1nA-10nA. Encouraged by these results we used the system as EXAFS detector. The results show a superior data quality for the thin films in comparison to conventional fluorescence EXAFS data (13 element Ge-detector). Within the next year the system will be combined with the analyzer system. This will give us the ability to determine the energy distribution of the emitted photo electrons. We aim for a low energy cut-off of about 3eV-5eV. To satisfy the needs of photo cathode

development in the solar energy area we plan to expand the measurement to the optical and UV-regime. Appropriate laser systems are available.



Figure 6.2. Schematic view of the sample electron total yield detector developed by me. The system is designed using the triaxial principle which dramatically reduces the electronic noise. The extraction grid is designed in a way which allows one to implement an additional electron lens system imaging the electron source ontto the entrance slit of the hemispherical analyzer.

In collaboration with experts in fast and ultrafast detector design I will also implement time resolving techniques to characterize the time distribution of the photo-electrons. First tests of the time response have already been performed and modifications to the cathode layout are on the way, which will allow us to couple the RF-power created by the bunched x-rays or laser photons into the amplifier unit without impedance mismatches.

Finally, we can say that Co doped ZnO nanoparticles produced by chemical vapor synthesis (CVS) will perform to fabricate highly efficient photo cathode and this photo cathodes will be used for x-ray streak cameras or hybrid solar cells.

REFERENCES

ANKUDINOV ,A L., RAVEL B., REHR J J., ALBERS R C., AND CONRADSON S D, 1998. Phys. Rev. B 58 7565

ARČON I., MOZETIČ M., KODRE A., JAGIELSKI J., TRAVERSE A.,2001. EXAFS study of NiAl in thin films, J. Sinch. Radiation 8 493-495

ARČON I., MIRTIČ B., KODRE A., 1998 (Determination of valence states of chromium in calcium chromates by using X-Ray Absorption Near-Edge Structure (XANES) Spectroscopy, J. Am. Ceram. Soc. 81/1 222-224)

ATWOOD D. 1999, "Soft X-rays and Extreme Ultraviolet Radiation Principles and Applications" Cambridge University Press.

BAJT S.S., DELANEY S. R., GEOCHIM J., 1994Cosmochim. Acta, 54, 5209-5214

BARATON, M.-I. AND MERHARI, L. ,2004. Advances in air quality monitoring via nanotechnology. Journal of Nanoparticle Research, Vol. 6, p. 107.117

BARE SIMON R., 2008 APS XAFS School, Aug 4-8,

BARUCHEL J., HODEAU J.L. LEHMANN, M.S., REGNARD J.R., SCHLENKER C.EDS., 1993 Neutron and synchrotron radiation for condensed matter studies,Springer-Verlag, Les éditions de physique, Vol. 1, p. 323-361

BIANCONI A., KONINGSBERGER D. C, AND PRINS R.1988 XANES Spectroscopy;New York, , pp 573-662

BIZEK, H. M., 1996 "The Advanced Photon Source List of Parameters," Argonne National Laboratory,

BOULOUDENINE, M.; VIART, N.COLIS, S. KORTUS, J. DINIA, A., 2005Appl. Phys. Lett., 87, 052501

BOULOUDENINE M., VIART N., COLIS S., KORTUS J., DINIA A. 2005, Appl. Phys. Lett., 87 052501

BREHM, J., U. WINTERER, M., HAHN, H., 2006 J. Appl. Phys., 100, 064311

COMBE, N., CHASSAING, P. M., DEMANGEOT, 2009 F. Phys. Rev. B 79 , 045408CONG, C. J. HONG, J. H.LIU, Q. Y.LIAO, L.,ZHANG, 2006 K. L. Solid State Comm., 138, 511

CHAMBERS, S. A. DROUBAY, T. C. WANG, C. M.,ROSSO, K. M., HEALD, S. M.,SCHWARTZ, D. A., KITTILSTVED, K. R., GAMELIN, D. R. ,2006Mater. Today , 9, 28

CHAMBERS S. A. and FARROW R. F. C., 2003 MRS Bulletin, , 28(10), 729 - 733.

CHAMBERS A. and YOO Y. K., 2003 MRS Bulletin, , 28(10), 706 - 707.

CHENG ,X. M. and CHIEN C. L., 2003, J. Appl. Phys. 93, 7876

CHISHOLM F., LEE J. S., KHIM Z. G., PARK Y. D., WILSON R. G., 2003Appl. Phys. Lett., , 83(26), 5488 - 5490

CUI J. B. and GIBSON U. J., 2005.Appl. Phys. Lett. 87, 133108

DEKA S., PASRICHA R., JOY P. A., 2004 Chem. Mater., 16, 1168 - 1169

DESGRENIERS,1998, S. Phys. Rev. B, 58, 14102

DIETL, T., OHNO, MATSUKURA H., CIBERT, F., FERRAND J.D. 2000Science , 287, 1019

DUAN, L. B. CHU, W. G. YU, J. WANG, Y. C. ZHANG, L. N. LIU, G. Y.

DUKE P., 2000 Synchrotron Radiation (Oxford, UK,)

DURHAM, P. J. KONINGSBERGER, D. C. AND PRINS, R., JOHNWILEY ED.1988Theory of XANES;New York, ED C. K., 1979 .Synchrotron radiation: techniques and applications , Topics in current physics, Springer,

EDELSTEIN, A. S. and CAMMARATA, R. C. (Eds.) 1996. Nanomaterials: synthesis, properties and applications. Bristol, Institute of Physics Publishing. 596 p

EDELSTEIN, A. S. and CAMMARAT, R. C.,1988 Nanomaterials: synthesis, properties and applications. Bristol, Institute of Physics Publishing. P. 13.54

EDWARD W. ,2004 “XAFS: Context, theory, practice” UCSD Physics 152A March 4,

EL-SHALL, M. S. and EDELSTEIN, A. S. 1996. Formation of clusters and nanoparticles from supersaturated vapor and selected properties

ENCYCLOPEDIA BRITTANNICA.
http://www.britannica.com/EBchecked/topic/650351/X-ray

GAUDON, M. ,TOULEMONDE, O., DEMOURGUES, A., 2007 Inorg. Chem., 46, 10996

HAN, A. R.; HWANG, S.J. ZHAO, Y. KWON, Y.U. J. 2008 Magn. Magn. Mater., 320, 1591

HALL S., ALLEN, F. & BROWN, I. , 1991. Acta Cryst. A47, 655–685

HEALD, D. A. SCHWARTZ, K. R. KITTILSTVED, D. R. GAMELIN, 2006,Mater. Today 9 28

HEALD, S. M. AND PRINS, R., ED. , 1988 JOHN WILEYEXAFS with synchrotron raditation;Koningsberger, New York, , pp 119-161

HELMUT W., 1998 "Synchrotron Radiation Primer" Stanford Synchrotron Radiation Laboratory, SSRL October,

HINDS, W. C. B., WILLEKE P. A., , EDS K., 2001WILEY Physical and Chemical Changes in the Particulate Phase. In Aerosol Measurement pp 83

HOFMANN, A. ,2004, Synchrotron Radiation Cambridge, UK,

HOFMANN ,A. 1978 "Quasi –Monochromatic Radiation fron undulators" Nucl.Instrum. and Meth. 152,17and "Theory of Synchrotron radiation " Stonford Synchrotron Radiation Laboratory report ACD-Note 30(unpublished)

HUANG M. ,MAO H. S., FEICK H., YAN H,. WU Y., KIND H., WEBER E., RUSSO, R. and YANG P., 2001 Science 292, 1897

ICHINOSE N., OZAKI, Y. AND KARSU, S. 1992. Superfine particle technology. London, Springer- Verlag. 223 p

IWASAWA Y., 1996 "X-ray absorption fine structure for catalysts and surfaces" By Published by World Scientific,

JACKSON J.D., Classical Electrodynamics .1999 Wiley, New York,.Third edition.

JAYARAM, V. RAJKUMAR, J. ,RANI, B. S. ,1999 J. Am. Ceram. Soc., 82, 473.

JIN, W., LEE, I.K., KOMPCH, A.DÖRFLER, U. ,WINTERER, M., 2007J. Europ. Ceram. Soc., 27, 4333

JIN W., LEE I. K., KOMPCH A., DÖRFLER U., and WINTERER M., 2007, J. Eur. CeramSoc. 27 4333

JIN Z., T. FUKUMURA, KAWASAKI M., ANDO K., S AITO H., SEKIGUCHI T., Y. OOZ.Y, MURAKAMI M., MATSUMOTO Y., HASEGAWA T., AND

JENKINS H. R., WILEY J. and SONS,2000,"X-ray techniques:Overview" in Encyclopedia of Analytical Chemistry,

JIN, Z. F., T., KAWASAKI, M.; ANDO, K. SAITO, H. SEKIGUCHI, T.; YOO, Y. Z. MURAKAMI, M. MATSUMOTO, Y. HASEGAWA, T.

KOINUMA, H., 2001Appl. Phys. Lett., 78, 3824

KAMAROV A., M.PJABCHENKO V., S. TERLETSKII, O. V., ZHERU I. I. AND R. IVANCHUCK D., 1977 Zh. Eksp. Teor. Fiz, 73, 608

KAMAT, P. V. AND MEISEL, D. 2003. Nanoscience opportunities in environmental remediation. C.R. Chimie, Vol. 6, p. 999.1007

KAS J., 2000 “Theory and Calculation of X-Ray Absorption”,

KELLY S.2008 “Basics of EXAFS data analysis” Argonne National Laboratory, Argonne, IL,APS Summer School,

KELLY S. et al.,2000 “Analysis of Soils and MineralsUsing X-ray Absorption Spectroscopy”,Chapter 14

KIHARA K., DONNAY G., 1985 The Canadian Mineralogist 23 647

KIM J. H., KIM H., KIM D., IHM Y. E., AND CHOO W. K., 2002J. Appl. Phys. 92, 6066

KIM, Y.I. , PAGE, K.; SESHADRI, R., 2007Appl. Phys. Lett., 90, 101904

KIM K.J. 1989 “ Characteristic of Synchrotron Radiation” pp.565-632 in Physics of Particle Accelerators,AIP Conference Pronceding 184(Amer .Inst. of Physics.New york)

KIM K.J. ,1995 “ Optical and power chacteristic of Synchrotron Radiation Sources” Opt.Engr.34,342

KISI, E. H., ELCOMBE, M. M. ,1989, Acta Cryst. C45, 1867KITTILSTVED K. R. and GAMELIN D. R., AM J.. 2005 Chem. Soc. 127, 5292

KOCH E. 1987 ‘’Handbook on Synchrotron Radiation’’, North Holland Pub. Corp.,

KODRE, I. ARČON, 2000, Proceedings of 36th International Conference on Microelectronics, Devices and Materials, MIDEM, Postojna, Slovenia, October 28-20, p. 191-196 Vol. Iaand Ib 1983, Vol. II

KOLESNIK S., B. DABROWSKI, J. MAIS, 2004 J. App. Phys., 95 2582

KOLESNIK, S.; DABROWSKI, B., 2004MAIS, J. J. App. Phys., 95, 2582

KONINGSBERGER D.C. , PRINS R., 1988 X-ray Absorption, Principles, techniques of EXAFS, SEXAFS and XANES, John Wiley & Sons, New York, ISBN 0-471-87547-3

KONINGSBERGER D. C. and PRINS R.,1988 X-ray absorption. Principles and applications: techniques of EXAFS, SEXAFS andXANES, eds. (Chemical Analysis Vol. 92, Wiley,)

KONINGSBERGER and R. PRINS EDS. 1988, X-ray absorption. Principles and applications: techniques of EXAFS, SEXAFS and XANES D. C. Chemical Analysis Vol. 92, Wiley,)

KHARE N., KAPPERS M. J., WEI M., BLAMIRE M. G., AND MAC MANUS DRISCOLL J. L. , 2006 Adv. Mater. 218, 1449

KRAUSE, M. O. 1979 J. Phys. Chem. Ref. Data, 8, 307

KRONIG, R. D. L. Z. 1932 Phys., 75, 468

KRUIS, F. E., FISSAN, H. and PELED, A. 1998. Synthesis of nanoparticles in the gas phase for electronic, optical and magnetic applications . a review. Journal of Aerosol Science, Vol. 29(6), p. 511.535

LAI, BKHOUNSARY, A.SAVOY, R. MOOG, L. GLUSKIN, E., 1993"Undulator A Characteristics and Specifications," Argonne National Laboratory,.

LEE, E.C.; CHANG, K. J. 2004 Phys. Rev. B, 69, 085205.

LEEN H-J., EONGS-Y. J, CHO C. R. and PARK C. H., 2002Appl. Phys. Lett., 81(21),4020 - 4022

LIU T., XU H., CHIN W. S., YONG Z., WEE, A.T.S. 2008 J. Phys. Chem. C 112 3489.

LIU X., PREWITT C. T., 1990 Phys. Chem. Minerals, 17 168.

LIU B. and ZENG H. C., 2004. J. Am. Chem. Soc. 126, 16744

LIU, X.-C. SHI, E.-W. CHEN, Z.-Z. ZHANG, H.-W. SONG, L.-X. WANG, H.YAO, S.-D., 2006 J. Cryst. Growth, 296, 135.

LUTTEROTTI L. and SCARDI P., 1990, J. Appl. Cryst., 23 246.

LIU, X., PREWITT, C. T. 1990Phys. Chem. Minerals, 17, 168.

MARGARITONDO, G.,1988 Introduction to Synchrotron Radiation; Oxford University Press:New York,

MATSUMOTO Y., MURAKAMI M., SHONO T., HASEGAWA T., FUKUMURA T. , KAWASAKI M., 2007 Phys. Rev. B **76**, 115320

MILLS D.M. , 1999Lecture notes , APS ,Argonne

MOULIN C. CARTIER DIT, BRIOIS V. LAGARDE P., VILLAIN F., and VERDAGUER M., 2001x-ray absorption spectroscopy in molecular magnetism Universidad de Zaragoza Publicationes , pp. 251-284

MULLER J.E, 1984 EXAFS and Near-edge structure III, Springer Proc. Phys., 2, 7.

NEWVILLE M. AND RAVEL B. ATHENA, ARTEMIS, HEPHAESTUS, 2005. data analysisfor X-ray absorption spectroscopy using IFEFFIT J. Synchrotron Rad.12, 537–541

NEWVILLE, M., RAVEL, B., HASKEL, D., REHR, J. J., STERN, E. A. & YACOBY, Y., 1995. Physica B, 208/209, 154–156.

NEWVILLE, M., 2001J. Synchroton Rad., 8, 322.

NEWVILLE M. ,2004 “Fundamentals of XAFS”, , Revision 1.6 July 22,

NORBERG N. S., KITTILSTVED K. R., AMONETTE J. E., KUKKADAPU R. K., SCHWARTZ D. A., AND GAMELIN, D. R. ,2004 J. Am.Chem. Soc. 126, 9387 NIELSEN ALS J ,DES MCMORROW,. “Elements of Modern X-Ray Physics”, 2001

NORTON D. P., OVERBERG M. E., PEARTON S. J., PRUESSNER K., BUDAI J. D., BOATNER L. A., YAN M. S-S., REN C., WANG X., XIN Y., ZHOU Z. X. MEI L. M., REN M. J., CHEN Y. X., LIU Y. H. and GARMESTANI H. ,2003, Appl. Phys. Lett., , 84(13), 2376 - 2378.

NORTON D. P, OVERBERG M. E., PEARTON S. J., PRUESSNER K., BUDAI J. D.,BOATNER L. A., CHISHOLM M. F., LEE J. S., KHIM Z. G., PARK Y. D., WILSON R. G., 2003 Appl. Phys. Lett., , 83(26), 5488 - 5490

PARK J. H., 2004 M. G. KIM, H. M. JANG, AND S. RYU, Appl. Phys. Lett. 84, 1338

PAN Z. W., DAI Z. R., and WANG,Z. L. 2001 Science 291, 1947

PRELLIER W., FOUCHET A. AND MERCEY B., , 2003 J. Phys. Condens. Matter, 15, R1583 -R1601

RAMACHANDRAN S., A. TIWARI, J.NARAYAN,2004,, Appl. Phys. Lett. 84(25), 5255 – 5257

RAVEL, B. ,2001. J. Synchrotron Rad. 8, 314–316.

RAVEL, B. NEWVILLE, M. 2005J. Synchroton Rad., 12, 537.

REHR J. J. and ALBERS R.C., (2000)Rev. Mod. Phys. 72, 621

REHR, J. J. ALBERS, 1990 R. C. Phys. Rev. B, 41, 8139. RADOVANOVIC P. V. and D. R. GAMELIN, 2003 Phys. Rev. Lett. 91, 157202

RISBUD A. S., SPALDIN N. A., CHEN Z. Q., STEMMER S. and SESHADRI R. 2003, Phys. Rev. B., , 68, 205202-1 - 205202-7.

RIETVELD, H. M. 1969, J. App. Cryst. 2, 65.

RODE K., ANANE A., MATTANA R., CONTOUR,J. –P. O. DURAND and LEBOURGEOIS R. , ., 2003 Appl. Phys. Lett, 93(10), 7676 - 7678

SAMSON J. and EDERER D., 1998 Vacuum Ultraviolet Spectroscopy I and II (Academic Press, San Diego,).

SATI P., HAYN R., KUZIAN R., RÉGNIER S., SCHÄFER S., STEPANOV A., MORHAIN C. , DEPARIS C., M LAÜGT., GOIRAN M., and GOLACKI Z., 2006. Phys. Rev. Lett. 96, 017203

SATO K. and KATAYAMA H. –Y., 2000Jpn. J. Appl. Phys., Part 239, L555 Physica E Amsterdam10, 2512001

SATO, K.; KATAYAMA-YOSHIDA, H. 2001 Physica E, 10, 251.

SATO K. and KATAYAMA-YOSHIDA H., 2000, Japan. J. Appl. Phys., 39, L555 – L558.

SAYERS, D. E.; LYTLE, F. W.; STERN, E. A. 1970Adv. X-ray Anal., 13, 248.

SAYERS, D. E.; STERN, E. A.; LYTLE, F. W. 1971, Phys. Rev. Lett. 27, 1204.

SCHNEIDER, L. ZAITSEV, S. V. JIN, W.; KOMPCH, A. WINTERER, M. ACET, M. BACHER, 2009G. Nanotechnology, 20, 135604.

SCHULZE, D. G.; SUTTON, S. R.; BAJT, S. 1995Soil Sci. Soc. Am. J., 59, 1540-1548.

SCHWARTZ D. A., NORBERG N. S., NGUYEN Q. P., PARKER J. M., GAMELIN D. R. , 2003 J. Am.Chem. Soc., , 125, 13205 - 13218.

SHANNON, R. D. ,1976, Acta Crystallogr. A 32, 751.

SHARMA P., GUPTA A., OWENS F. J., INOUE A., and RAO K. V., J. MAGN2004. Magn. Mater. 282, 115

SHI T. AND SANYUAN Z., ZHIHU S.and SHIQIANG W., WENHAN L., 2007 Applied physics letters 90, 102108

SHI, T., ZHU, S.,SUN, Z.,WEI, S.,LIU, W., 2006 Appl. Phys. Lett. 2007, 90, 102108.SCHAEDLER, T. A.,GANDHI, A. S., SAITO, M.,RÜHLE, M., GAMBINO, R.,LEVI, C. G. J. Mater. Res., 12, 791.

SLUITER M. H. ,KAWAZOE ,SHARMA F. Y., INOUE, P., RAJU A. A. R., ROUT C. , and WAGHMARE U. V., 2005 Phys. Rev. Lett. 94, 187204

SUN Z. H.,WENSHENG Y.,GUOBIN Z.,1 HIROYUKI O.I,ZIYU W.,QINGHUA L.,WENQING W.,TONGFEI S.,ZHIYUN P., PENGSHOU X.,and SHIQIANG W. ,2008 physical review b 77, 245208

STÖHR J., NEXAFS Spectroscopy, 1992 Vol. 25 of Springer Series in Surface Sciences (Springer, Heidelberg,).

STERN E. A. , 1988 Theory of EXAFS, Edited by Koningsberger and Prins

STRAUMAL, B.; BARETZKY, B.; MAZILKIN, A.; PROTASOVA, S.; MYATEV, A.; STRAUMAL, P., 2009J. Eur. Ceram. Soc., 29, 1963.

SZULCZEWSKI, M. D.; HELMKE, P. A.; BLEAM, W. F. 1997Environ. Sci. Technol. , 31,2954-2959.

TEO. B. K. EXAFS, 1986 Basic Principles and Data Analysis; Springer-Verlag: New York,.

TIANZ.R., VOIGT, LIU J. A. J., MCKENZIE B., MCDERMOTT M. J., RODRIGUEZ M. A. , KONISHI H., and XU, H. ,2003 .Nature Mater. 2, 821

THOLE B. T., G. VAN DER LAAN, Phys. Rev. B, 1988, 38, 3158.

TJONG, S. C. AND CHEN, H. 2004. Nanocrystalline materials and coatings. MaterialsScience and Engineering R, Vol. 45, p. 1.88.

UEDA K., TABATA H. and KAWAI T., 2001 Appl. Phys. Lett., , 79(7), 988 - 990

VENKATESAN M., C. B. FITZGERALD, J. G. LUNNEY, AND J. M. D. COEY, 2004. Phys. Rev. Lett. 93, 177206

WARREN B.E., 1990 “X-Ray Diffraction “,

WILLIAMS, A. R.; LANG, N. D. Phys. Rev. Lett. 1978, 40, 954-957

WINTERER M., SRDIC V. V., DJENADIC R., KOMPCH A. and WEIRICH T. E., 2007,Rev. Sci. Instr., 78 123093.

WINICK, H., 1980Properties of Synchrotron Radiation; Winick, H. and Doniach, S.,

WINTERER, M., 2002,Nanocrystalline Ceramics – Synthesis and Structure; Springer Verlag, Berlin,.

WINTERER, M. 1997J. Phys. IV, 7C2-243.

WINTERER, M. J. ,2000Appl. Phys., 88, 5635.

WOLTERSDORF, J.; NEPIJKO, 1981,A. S.; Pippel, E. Surf. Sci., 106, 64.

WU J., SAI-CHANG LIU AND MING-HSUN YAN, 2004 Appl. Phys. Lett., 85, 1027 Ed. Plenum Press: New York, , pp 11-26.

WYCKOFF, R. W. G., 1963 Crystal Structures; Vol. 1, John Wiley & Sons, New York, London,.X-Ray Data Booklet Section 2.2

YAN L., ONG C. K., and RAO X. S., J. 2004.Appl. Phys. 96, 508

YAN S-S., REN C., WANG X., XIN Y., ZHOU Z. X., MEI L. M., REN M. J., CHEN YIN Z., CHEN N., CHAI C., and YANG F., 2004. J. Appl. Phys. 96, 5093 YOON S. W., CHO S.-B., S. C. YOON WE, S., SUH B. J. SONG, H. K. and SHIN Y. 2003 J., J. Appl. Phys., Vol. 93,

ZABINSKY, S. I., REHR, J. J., ANKUDINOV, A., ALBERS, R. C. & ELLER, M. J. 1995. Phys. Rev. B, 52, 2995–3009.

ZABINSKY, S. I. REHR, J. J. ANKUDINOV, A.ALBERS, R. C. ELLER, M. J. 1995Phys. Rev. B, 52, 2995.

ZIESE M.and THORNTON M. F., EDS., 2001Spin Electronics (Springer, Berlin,).

ZHANG, W. 2003. Nanoscale iron particles for environmental remediation: an overview. Journal of Nanoparticle Research, Vol. 5, p. 323.332.

CURRICULUM VITAE

Güvenç AKGÜL was born in Ceyhan in 1976. He finished Ceyhan high school, and continued his studies in Physics in University of Cukurova obtaining a BSc in Physics in 2000 and MSc in Physics in 2004. He wrote a master thesis on the subject “A Study of 3d Transition metals by X-Ray Absorption Spectroscopy” under the supervision of Prof. Ufuktepe. He was research and teaching assistant at Physics department in University of Cukurova in 2005. He continued his Ph.D. research under the supervision of Prof. Ufuktepe. His research was performed at the Argonne National Lab. Chicago IL,USA, under the supervision of Dr. Klaus Attenkofer. His research was on characteristics of doping nanomaterials especially Transmission metals doped ZnO nanoparticles produced by chemical vapor synthesis (CVS).

APPENDIX

Lorentz Space-Time Transformations

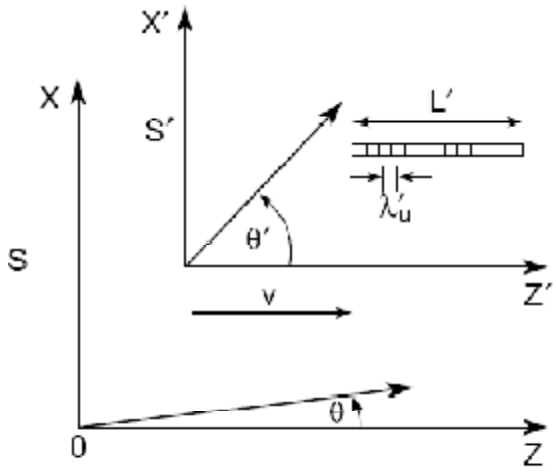

1- $z = \gamma(z' + \beta ct')$

2- $t = \gamma\left(t' + \frac{\beta z'}{c}\right)$

3- $y = y' \quad \text{and} \quad x = x'$

4- $z' = \gamma(z - \beta ct)$

5- $t' = \gamma\left(t - \frac{\beta z}{c}\right)$

6- $y' = y \quad \text{and} \quad x' = x$

7- $\beta \equiv \frac{v}{c}$

8- $\gamma \equiv \frac{1}{\sqrt{1-\beta^2}}$

9- $\omega = \omega'\gamma(1 + \beta\cos\theta')$

10- $\omega' = \omega\gamma(1 - \beta\cos\theta)$

11- $L' = L/\gamma$

12- $\Delta t' = \Delta t/\gamma$

13- $\cos\theta = \frac{\cos\theta' + \beta}{1 + \beta\cos\theta'}$

14- $\cos\theta' = \frac{\cos\theta - \beta}{1 - \beta\cos\theta}$

15- $\sin\theta = \frac{\sin\theta'}{\gamma(1 + \beta\cos\theta')}$

16- $$\sin\theta' = \frac{\sin\theta}{\gamma(1-\beta\cos\theta)}$$

17- $$\tan\theta = \frac{\sin\theta'}{\gamma(\cos\theta'+\beta)}$$

18- $$\tan\theta' = \frac{\sin\theta}{\gamma(\cos\theta-\beta)}$$

Vector Formulas

$$\mathbf{A}\cdot(\mathbf{B}\times\mathbf{C}) = (\mathbf{A}\times\mathbf{B})\cdot\mathbf{C} = \mathbf{C}\cdot(\mathbf{A}\times\mathbf{B}) = (\mathbf{C}\times\mathbf{A})\cdot\mathbf{B} = \mathbf{B}\cdot(\mathbf{C}\times\mathbf{A})$$
$$\mathbf{A}\times(\mathbf{B}\times\mathbf{C}) = \mathbf{B}(\mathbf{A}\cdot\mathbf{C}) - \mathbf{C}(\mathbf{A}\cdot\mathbf{B})$$
$$(\mathbf{A}\times\mathbf{B})\cdot(\mathbf{C}\times\mathbf{D}) = (\mathbf{A}\cdot\mathbf{C})(\mathbf{B}\cdot\mathbf{D}) - (\mathbf{A}\cdot\mathbf{D})(\mathbf{B}\cdot\mathbf{C})$$

Derivatives of Sums

$$\nabla(f-g) = \nabla f + \nabla g$$
$$\nabla\cdot(\mathbf{A}+\mathbf{B}) = \nabla\cdot\mathbf{A} + \nabla\cdot\mathbf{B}$$
$$\nabla\times(\mathbf{A}+\mathbf{B}) = \nabla\times\mathbf{A} + \nabla\times\mathbf{B}$$

Derivatives of Products

$$\nabla(fg) = f\nabla g + g\nabla f$$
$$\nabla(\mathbf{A}\cdot\mathbf{B}) = \mathbf{A}\times(\nabla\times\mathbf{B}) + \mathbf{B}\times(\nabla\times\mathbf{A}) + (\mathbf{A}\cdot\nabla)\mathbf{B} + (\mathbf{B}\cdot\nabla)\mathbf{A}$$
$$\nabla\cdot(f\mathbf{A}) = f(\nabla\cdot\mathbf{A}) + \mathbf{A}\cdot\nabla f$$
$$\nabla\cdot(\mathbf{A}\times\mathbf{B}) = \mathbf{B}\cdot(\nabla\times\mathbf{A}) - \mathbf{A}\cdot(\nabla\times\mathbf{B})$$
$$\nabla\times(f\mathbf{A}) = f(\nabla\times\mathbf{A}) - \mathbf{A}\times(\nabla f)$$
$$\nabla\times(\mathbf{A}\times\mathbf{B}) = \mathbf{A}(\nabla\cdot\mathbf{B}) - \mathbf{B}(\nabla\cdot\mathbf{A}) - (\mathbf{B}\cdot\nabla)\mathbf{A} - (\mathbf{A}\cdot\nabla)\mathbf{B}$$

Second Derivatives

$$\nabla\times(\nabla\times\mathbf{A}) = \nabla(\nabla\cdot\mathbf{A}) - \nabla^2\mathbf{A}$$
$$\nabla\cdot(\nabla\times\mathbf{A}) = 0$$
$$\nabla\times(\nabla f) = 0$$

Integral Theorems

$$\int_V (\nabla\cdot\mathbf{A})\,dV = \oint_S \mathbf{A}\cdot\hat{\mathbf{n}}\,dS \qquad \text{Gauss's (divergence) Theorem}$$

$$\int_S (\nabla\times\mathbf{A})\cdot\hat{\mathbf{n}}\,dS = \oint_C \mathbf{A}\cdot d\boldsymbol{\ell} \qquad \text{Stokes's (curl) Theorem}$$

$$\int_{\mathbf{a}}^{\mathbf{b}} (\nabla f)\cdot d\boldsymbol{\ell} = f(\mathbf{b}) - f(\mathbf{a})$$

$$\int_V (f\nabla^2 g - g\nabla^2 f)\,dV = \oint_S (f\nabla g - g\nabla f)\cdot\hat{\mathbf{n}}\,dS \qquad \text{Green's Theorem}$$